PRECISION MEASUREMENTS IN ATOMIC CESIUM-133

by

Jonah Quirk

A Dissertation

Submitted to the Faculty of Purdue University

In Partial Fulfillment of the Requirements for the degree of

Doctor of Philosophy

Department of Physics and Astronomy

West Lafayette, Indiana

May 2025

THE PURDUE UNIVERSITY GRADUATE SCHOOL
STATEMENT OF COMMITTEE APPROVAL

Dr. Daniel S. Elliott, Chair

Department of Physics and Astronomy

Dr. Christopher H. Greene

Department of Physics and Astronomy

Dr. Chen-Lung Hung

Department of Physics and Astronomy

Dr. Jonathan D. Hood

Department of Chemistry

Approved by:

Dr. Gabor A. Csathy

To my wife, Jamie.

ACKNOWLEDGMENTS

A PhD is never done alone and I have many people to thank for helping me along the way. First of all, I would like to thank Dr. Elliott for his endless patience and encouragement. His optimism often exceeded my own and played a significant role in the completion of this dissertation. I would also like to thank our collaborator Dr. Carol Tanner. She not only brings an immense experience in precision measurements, but also a unique perspective on our work that we often miss due to its proximity.

While at Purdue, I have had the pleasure of working with many talented individuals. George, May, and Cheng-an taught me much of what I know and cheerfully answered an endless number of questions and Amy and Diego worked and bounced ideas around with me. Also, we have been fortunate to host many talented undergraduate students and some of which contributed to this work. In particular, Aidan helped build the $\langle m \rangle$ switching apparatus and significantly contributed to the Stark shift measurement.

I would also like to thank the ECE staff members that help keep us running. Jill, Emily, Kyra, and Kendra for helping us place important orders, Bob for making sure we are able to get our packages, and Steve and Jordan for managing the building and upgrading our office! I would also like to thank the physics graduate coordinators Sandy and now Maria for their expertise in navigating the physics department and graduate school rules. Also in the physics department, I would like to thank Jim for his assistance in many machining projects. Though sporadic, machine shop visits are always critical in keeping projects moving forward.

Finally. I would like to thank family for their support and encouragement while continuing my education. Most of all, I would like to thank my wife, Jamie. She has been incredibly patient and understanding throughout this PhD and for this I am grateful.

TABLE OF CONTENTS

LIST OF TABLES

LIST OF FIGURES

ABBREVIATIONS

α	Stark scalar transition polarizability
$\tilde{\alpha}$	two-photon scalar transition polarizability
α_{ns}	static polarizability of an ns state
APV	Atomic parity violation
β	Stark vector transition polarizability
$\tilde{\beta}$	two-photon vector transition polarizability
E_1	Electric dipole
E_2	Electric quadrupole
ECDL	External cavity diode laser
FCL	Frequency comb laser
γ	Stark tensor transition polarizability
M_1	Magnetic dipole
MOPA	Master oscillator power amplifier
NSD	Nuclear spin-dependent
NSI	Nuclear spin-independent
PBC	Power build-up cavity
PNC	Parity non-conservation
PZT	Piezo electric transducer
SAS	Saturated absorption spectroscopy
YDFA	Ytterbium doped fiber amplifier

ABSTRACT

Atomic parity violation measurements facilitate tests of the standard model in a tabletop platform. This parity violating effect is caused by the weak force interaction that slightly mixes states of opposite parity and weakly allows electric dipole transitions. Precision determinations of the extremely weak parity violating transition amplitude rely on interference techniques to amplify this weak transition. The strength of this interfering transition is critical in evaluating the parity violating amplitude and is the primary focus of this work. Here we discuss several measurements in atomic cesium-133 that aid in our understanding of atomic parity violation. We have remeasured the relative strength of the scalar and vector transition polarizabilities on the $6s\ ^2S_{1/2} \rightarrow 7s\ ^2S_{1/2}$ transition to better that 0.1%. We have measured the static Stark polarizability on the $6s\ ^2S_{1/2} \rightarrow 7s\ ^2S_{1/2}$ transition to better than 0.04%. With this value we also reevaluate the reduced electric dipole matrix elements $\langle 7s||r||7p_J\rangle$. We use these new matrix elements to reevaluate the calculated scalar transition polarizability on the $6s\ ^2S_{1/2} \rightarrow 7s\ ^2S_{1/2}$ transition. Finally, we have also measured hyperfine intervals on the $12s\ ^2S_{1/2}$, $13s\ ^2S_{1/2}$, $11d\ ^2D_J$, and $6p\ ^2P_J$ levels.

1. INTRODUCTION

1.1 Motivation

Atomic parity violation (APV) experiments permit studies of the weak force interaction between nucleons and electrons at low momentum transfers. This enables searches for new physics or physics beyond the standard model in a tabletop platform as opposed to large accelerator-type facilities. Several measurements are required to facilitate such a test of the standard model and the following equation for the weak charge of cesium (Q_w) summarizes these contributions.

$$Q_w = k_{PV} \frac{\mathrm{Im}(E_{PNC})}{\beta} \frac{\beta}{\alpha} \alpha \tag{1.1}$$

Here k_{PV} is an atomic structure factor dependent on electronic wave functions near the nucleus. This factor is the calculated ratio between the weak charge (Q_w) and the parity non-conserving moment (E_{PNC}). The second and third terms are precision ratio measurements done in an experimental lab. The final term (α) is the Stark scalar polarizability. Due to the extraordinary difficulty of making an absolute measurement of $\mathrm{Im}(E_{PNC})$, this moment is evaluated using two ratio measurements and a calculated value for α (or M_1^{hf}).[1] This thesis includes measurements intended to aid our theory friends in calculation of k_{PV}, a new measurement of α/β, and a Stark shift measurement that updates our value for α. This only leaves the second term, a measurement of the parity non-conserving weak interaction. The primary goal of our group is towards a new higher precision measurement of $\mathrm{Im}(E_{PNC})/\beta$. Although this onerous task has not been completed in this thesis, we still report much progress in many aspects of that measurement. We now have phase coherence between three optical fields, atomic spin polarization near 99%, a system to measure atomic spin polarization to this precision, and a significantly improved technique for phase-modulating optical fields.

Even though our E_{PNC}/β measurement is steadily progressing, atomic parity violation measurements are never easy. The weak force interaction perturbs atomic systems and weakly mixes opposite parity states. This mixing weakly allows electric dipole transitions

[1]↑We will circle back to M_1^{hf} later, but right now it isn't critical.

between the same parity states where it would otherwise be forbidden. As a comparison, the parity non-conserving (PNC) weak transition amplitude is eleven orders of magnitude smaller than D1 or D2 electric dipole transition amplitudes in cesium. Direct observation of the transition is futile. APV experiments rely on quantum interference techniques to modulate the weak transition relative to a stronger known transition. This technique was used to great effect by Wood and Wieman to reach an impressive 0.35% uncertainty in the ratio of E_{PNC}/β [1]. Studies of weak transitions are typically limited by systematic effects. These effects arise from imperfect field reversals required for interference. Our group has demonstrated a two-pathway coherent control technique to reduce these systematic errors as a means for weak signal detection [2–5]. This technique reduces systematic uncertainties by varying the optical phase of the driving laser radiation to interfere the weak transitions as opposed to changing experimental parameters that are difficult to reset reliably, such as field orientation and state preparation.

1.2 History of parity violation

The possibility of parity violation in weak interactions was first proposed in the late 1950s by Yang and Lee [6]. Until then, parity was thought to have been a preserved quantity due to measurements studying the electromagnetic and strong interactions. Chien-Shiung Wu later showed experimentally that parity was not conserved in the beta decay of cobalt-60 [7]. This discovery led to Yang and Lee receiving the Nobel prize in 1957.

Table 1.1. The most precise measurements of PNC in various atomic species.

Atom	Year	Uncertainty	Technique	Ref.
Bi	1991	2%	Optical Rotation	[8]
Pb	1995	1.1%	Optical Rotation	[9]
Tl	1995	1.1%	Optical Rotation	[10]
Yb	2019	0.5%	Stark Interference	[11]
Cs	1997	0.35%	Stark Interference	[1]

PNC experiments quantify the strength of the weak interaction between electrons and nucleons in atoms. This interaction is mediated by the exchange of a Z boson. The range

of this interaction is minuscule and can be thought of as a contact interaction [12]. Originally the parity non-conserving transition amplitude was thought to have been negligible, but interest in atomic parity non-conservation measurements heightened once Bouchiat and Bouchiat realized that the atomic parity violating transition amplitudes scaled roughly as the atomic number cubed, Z^3 [13, 14]. Since then, several heavy elements have been studied, the best of which have been recorded in Table 1.1. There is an effort by Antypas to further improve the Yb PNC measurement precision [15]. There are also ongoing efforts to measure PNC in Francium [16]. Even with this cubic dependence, the PNC interaction is quite difficult to measure. These measurements rely on relative measurements to compare with stronger more precisely known transitions. The best measurements of PNC rely on either Stark interference or optical rotations with the best of which being the Stark interference measurements.

The strength of the PNC interaction is related to the weak charge through an atomic-structure factor k_{pv}, and this relation is;

$$Q_w = k_{pv} E_{PNC} \tag{1.2}$$

where E_{PNC} is the measured interaction strength and Q_w is the weak charge. Measurements of APV in cesium remain the most accurate to date of any atomic species. Although cesium is fairly simple with a single valence electron, theoretical calculations of k_{pv} have struggled to reach the 0.35% level uncertainty of the best PNC measurements due to many small corrections that must be included. There is presently disagreement over contributions to k_{pv} and new calculations are underway to help resolve discrepancies and push the uncertainty below that of experimental results [17]. New high-precision calculations of dipole matrix elements in cesium hint at the possibility that theoretical calculations are more precise than what they were believed to be [18, 19]. Improved theoretical calculations strengthen the need for an updated measurement of PNC in cesium. Along with atomic theory, PNC measurements explore standard model low-energy predictions, while operating in a tabletop format. This is compared to large accelerator-type facilities working at higher energies. PNC

measurements play a unique and important role in searches for new physics not included in the standard model.

1.3 1997 measurement of E_{PNC}

The most precise measurement of atomic parity violation was conducted by the Boulder group in 1997 [1]. Carl E. Wieman's group measured the ratio of $E_{pnc}/\beta = -1.5935(56)$ mV/cm, the electric field at which the Stark-induced and PNC interactions are equal in strength. This measurement utilized a spin-polarized atomic beam to prepare atoms and a high-finesse optical cavity to amplify the weak signal from the $6s\ ^2S_{1/2} \rightarrow 7s\ ^2S_{1/2}$ transition. Interference due to 32 unique field orientations and polarizations allow them to characterize the strength of the weak force interaction relative to the well-known Stark vector polarizability while also rooting out systematic errors.

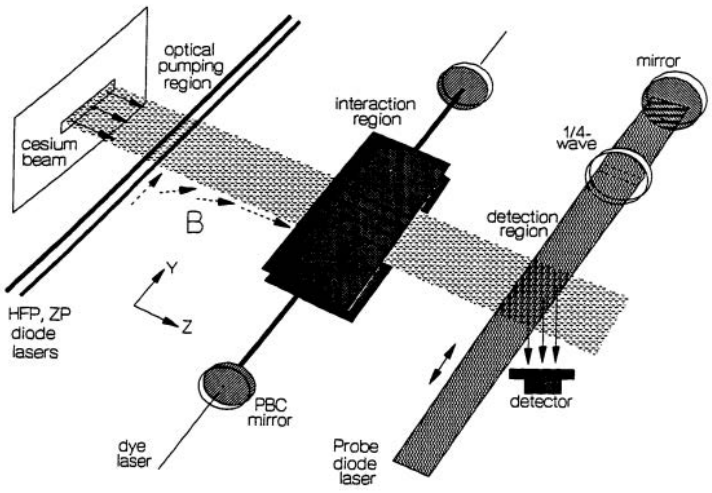

Figure 1.1. Experimental diagram of the 1997 PNC measurement from [1]

An experimental diagram of the Boulder measurement is illustrated in Fig. 1.1. In their experiment, they prepared the atoms in the atomic beam into a specific hyperfine (F) and Zeeman magnetic sublevel (m). The spin-polarized atoms then interact with an intense

standing wave laser beam resonant with the $6s\ ^2S_{1/2} \rightarrow 7s\ ^2S_{1/2}$ transition that is centered between two electric field plates. This intense laser beam greatly amplifies the observed interference signal. To detect the atoms that have undergone the transition, another laser is tuned to a cycling transition to detect atoms in the previously emptied state. Each atom scatters several photons which are detected by a large area photodiode. By modulating the fields or polarization of the standing wave, the interference between the Stark and PNC interaction reverses between constructive and destructive. This facilitates a precise relative measurement of the two interactions that is independent of poorly known experimental parameters, such as atomic beam density and interaction beam size. More information about this can be found in Wood's thesis [20].

1.4 Coherent control

We plan to repeat this exceptional measurement of E_{pnc}/β and further reduce the uncertainty using a coherent control technique that was pioneered in our lab [2–4]. This technique involves interfering weak transition amplitudes by varying the optical phase of the driving laser beams. This differs from Wieman's work in that they perform field reversals to interfere the weak transitions. By varying the optical phase, we are not reliant on the perfection of field reversals and we do not have to move or change the polarization of the laser beams. This technique was first demonstrated by our group and is depicted in Fig. 1.2. Here a strong two-photon interaction is beat against the much weaker Stark-induced interaction on the $6s\ S_{1/2} \rightarrow 8s\ S_{1/2}$ transition in cesium [2, 3]. An intense laser tuned to the two-photon frequency is used to generate a second harmonic beam in a nonlinear crystal. The two beams are coherent, a necessity for this type of experiment, and are split in a Mach-Zehnder interferometer. The relative phase of one of the beams is varied using a piezoelectric transducer (PZT) before the two beams are recombined and focused into a vapor cell containing electric field plates. Upon application of an electric field, the Stark-induced interaction becomes weakly allowed. The transition rate is proportional to the sum of the two transition pathways and is modulated by varying the optical phase. This modulation is studied to measure the relative strength of the two interactions.

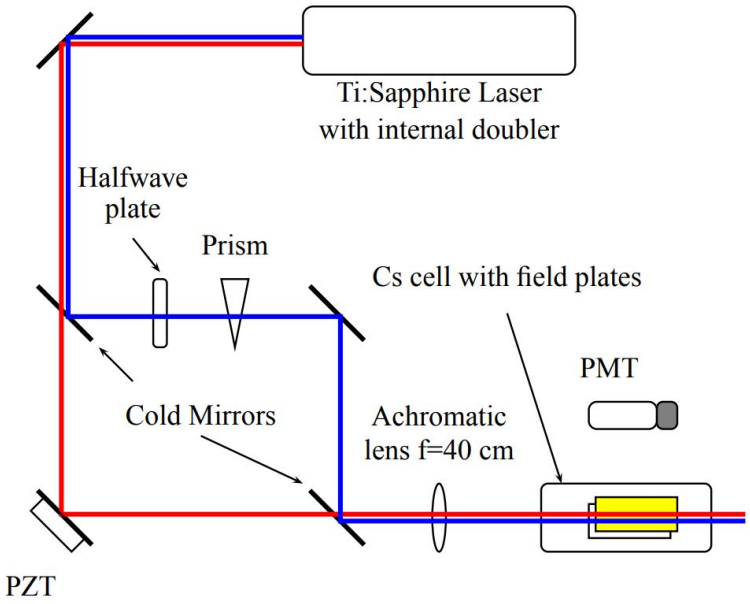

Figure 1.2. Experimental diagram of a weak signal measurement using coherent control from [3] PZT-Piezoelectric transducer, Cs-Cesium, PMT-Photomultiplier tube

This technique was then utilized by our group in a precision measurement of the ratio of the magnetic dipole moment to the vector Stark polarizability on the $6s\ ^2S_{1/2} \rightarrow 7s\ ^2S_{1/2}$ transition in cesium [4]. This was completed by interfering three different transitions, vector Stark, M_1, and a two-photon transition. When driving the interactions with phase-coherent laser fields, the transition rate goes as the square of the sum of each individual transition,

$$A^2 = |A_{2p} + A_{St} + A_{M_1}|^2 \approx A_{2p}^2 + 2A_{2p}(A_{St} + A_{M_1}) \tag{1.3}$$

where A_{2p}, A_{St}, and A_{M_1} are the transition amplitudes for the two-photon, Stark, and M_1 transitions respectively. The two-photon transition is much stronger than the other two transitions, so the individual transition rates and interference between only the weaker transitions are negligible and have been omitted. By varying the strength of the electric field driving the Stark transition, the interference term varied in amplitude and the relative strength of the M_1 and Stark transitions was measured. Currently, we use many of the

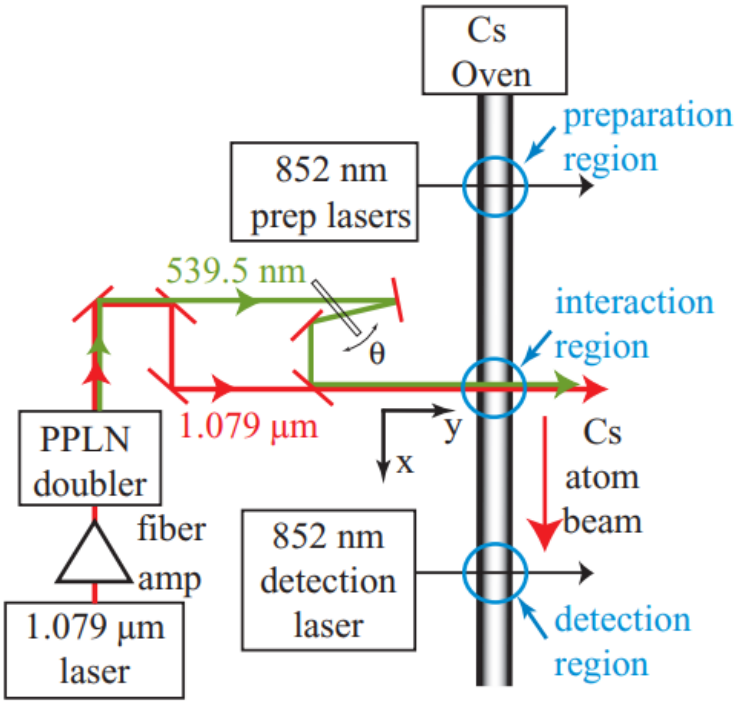

Figure 1.3. Experimental diagram of the M_1/β measurement using coherent control from [4]

techniques developed in these measurements in our lab. Dionysios Antypas constructed much of the vacuum system and multiple lasers we use for these coherent control experiments [21] and George Toh has spent a great deal of time searching for and reducing sources of noise in the lasers and electronics we currently use [22].

2. THEORY

This chapter details the theory that is necessary to understand the PNC experiment. Initially, properties of the $6s\ ^2S_{1/2} \rightarrow 7s\ ^2S_{1/2}$ transition and $7s\ ^2S_{1/2}$ state will be discussed. States will be abbreviated as ns and np_j for $ns\ ^2S_{1/2}$ and $np\ ^2P_j$ respectively. This will be followed with an overview of the weakly allowed $6s \rightarrow 7s$ single photon transitions and two-photon transition. Finally, the coherent control technique used to measure extremely weak transitions will be discussed.

2.1 Cesium

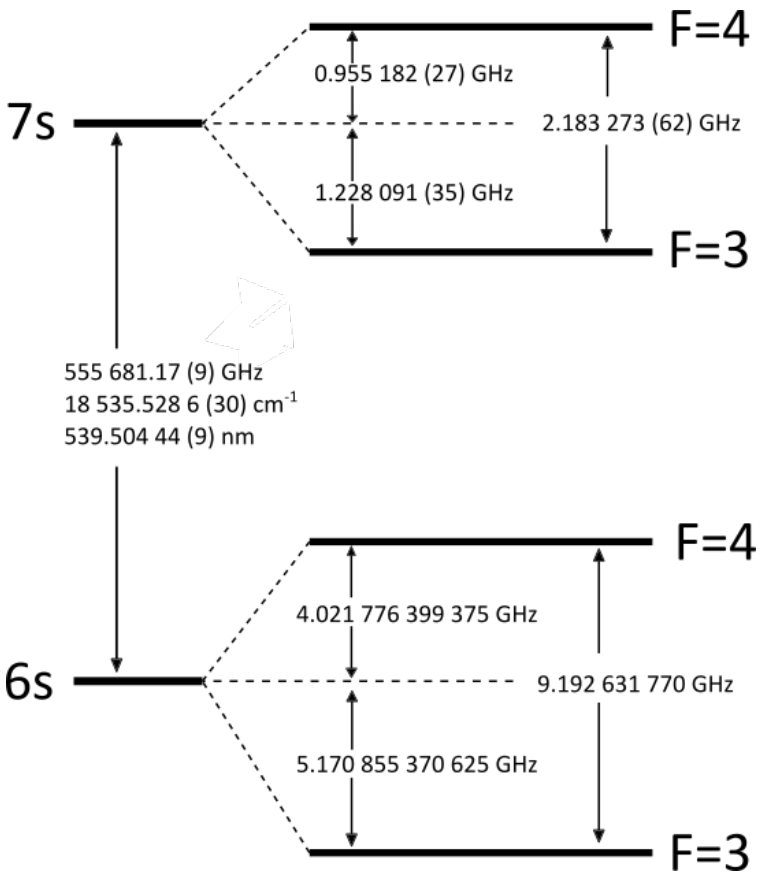

Figure 2.1. An energy level diagram of the $6s$ and $7s$ states. The hyperfine splitting of the $7s$ state is from [23] and the state energy is from [24].

Cesium-133 is an alkali metal with an atomic number of 55. Its ground state is the $6s\ ^2S_{1/2}$ state. To first order, an electric dipole transition coupling the $6s$ and $7s$ states is

forbidden due to their same parity. Cesium has a nuclear spin $I = 7/2$, so the $6s$ and $7s$ states are split into two hyperfine component, $F = 3$ and $F = 4$. F represents the total angular momentum ($F = I + J$). The ground state, $6s$, hyperfine interval is the basis of the second and is defined as 9 192 631 770 Hz. Under application of a magnetic field, the degeneracy of the $2F + 1$ magnetic Zeeman sublevels (m) is lifted. The energy shift of Zeeman sublevels is:

$$\Delta E = m g_F \mu_B B_z \tag{2.1}$$

where m is the magnetic Zeeman sublevel, g_F is the Lande g-factor, μ_B is the Bohr magneton, and B_Z is the applied magnetic field. For the $F = 3$ hyperfine level, the consecutive Zeeman sublevels are split by -0.35 MHz/G (0.35 MHz/G for F=4). This shift is illustrated in Fig. 2.2. Note that the state energies for different hyperfine levels, $F = 3$ and $F = 4$, move in opposite directions for the same magnetic Zeeman sublevel and that both the ground and excited $7s$ states are perturbed in this way. For example, under application of a magnetic field, the energy spacing between the $6s$ $F = 3, m = 3$ state and the $6s$ $F = 4, m = 3$ increases and oppositely signed magnetic sublevels would move closer.[1]

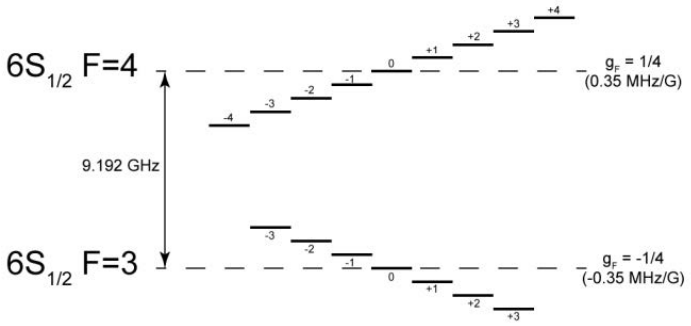

Figure 2.2. Illustration of the magnetic sublevel energy shift due to an applied magnetic field. Image from [22]

[1]↑This property will be used when determining ground state populations as discussed in Chapter 3.

Fig. 2.1 illustrates the energy levels of the $6s$ and $7s$ states along with their hyperfine structure. The $6s \rightarrow 7s$ transition can be driven weakly by a single photon at 539.5 nm (green) or two photons whose frequency add to that of the one photon frequency. The scaling of the hyperfine intervals has been greatly expanded for visibility.

2.2 Atomic parity violation

Atomic parity violation is caused by the weak force interaction through the exchange of a massive Z boson between nucleons and electrons. Due to the large mass of the Z boson ($m_z \approx 91\,\text{GeV}$), the interaction occurs over a short range and acts as a contact interaction[25]. This interaction is heavily dependent on the overlap of the electronic wave function and the nucleus. There are four main contributions to atomic parity violation, which are illustrated in figure 2.3. The first and by far the largest is a nuclear spin-independent (NSI) contribution from a Z-boson exchange between the axial-electron and nucleon-vector currents. The nuclear spin-dependent (NSD) contribution is comprised of three smaller contributions. The first is a Z-boson exchange between the nucleon-axial and electron-vector currents. The second and largest of the NSD terms is the electromagnetic exchange between and electron and a parity-violating toroidal current distribution within the nucleus know as the anapole moment. The last NSD interaction is a combined interaction between the NSI currents and the hyperfine interaction.

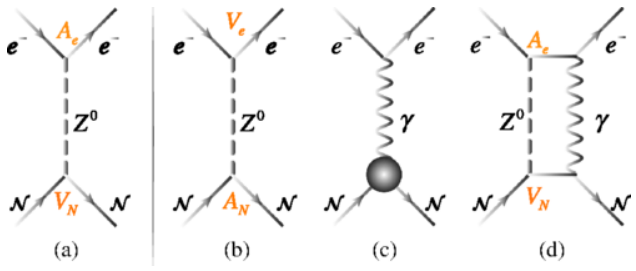

Figure 2.3. Diagram depicting the nuclear spin independent and nuclear spin dependent PNC interactions. Figure from [26].

The only observation of an anapole moment in any atomic species is the Boulder group's PNC measurement in cesium. Their determination consisted of measuring E_{PNC}/β on both

the $6sF = 3 \rightarrow 7sF = 4$ and $6sF = 4 \rightarrow 7sF = 3$ interactions. The average of these measurements is used to determine the nuclear spin-independent parity violating amplitude and the difference is used for the nuclear spin-dependent parity violating amplitude. Due to their high precision, they we able to measure the difference between these lines to be

$$\Delta \left[\frac{E_{PNC}}{\beta}\right]_{34-43} = -0.077 \pm 0.011 \; mv/cm. \tag{2.2}$$

A majority (84%) of this difference is caused by the anapole moment [27]. There is presently a deviation between the observed anapole moment and standard model predictions and a more precise measurement could possibly indicate new physics [28, 29]. We are currently working towards a new measurement of the NSD amplitude on the ground state of cesium.

2.3 $6s \rightarrow 7s$ transitions

In this section, the weakly allowed transitions coupling the $6s$ and $7s$ states will be discussed. Interference between these transitions is the basis for weak signal detection and is a key component in our coherent control technique. In Fig. 2.4, a simplified energy level diagram illustrates these weak interactions between the $6s$ and $7s$ states. In this figure, ω_1 represents the frequency of the one photon transitions. ω_2 and ω_3 represent the frequencies whose sum equals the one photon frequency.

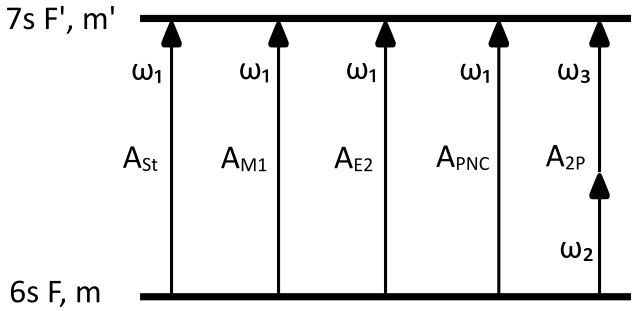

Figure 2.4. Simplified energy level diagram depicting the five allowed transitions that couple the $6s$ and $7s$ states.

2.3.1 Stark induced

When a DC electric field is applied to the atoms, opposite parity states mix via the Stark effect. This mixing weakly allows $\left|6S_{1/2}\ F, m\right\rangle$ to $\left|7S_{1/2}\ F', m'\right\rangle$ transitions. Mixing of the ns states is represented as $\left|\overline{6S_{1/2}Fm}\right\rangle$ where the bar denotes an s state with a slight amount of p states included. The transition amplitude between these two mixed states is;

$$\begin{aligned} A_{St}(F,m;F',m') &= \left\langle \overline{7S_{1/2}F'm'}|(-d\cdot\mathcal{E}^{\omega_1})|\overline{6S_{1/2}Fm}\right\rangle \\ &= \left[\alpha E\cdot\mathcal{E}^{\omega_1}\delta_{F,F'} + \mathrm{i}\beta\left(E\times\mathcal{E}^{\omega_1}\right)_z C_{F,m}^{F',m'}\right]\delta_{m,m'}\ \mathrm{e}^{\mathrm{i}\phi^{\omega_1}} \\ &+ \left[\pm\mathrm{i}\beta\left(E\times\mathcal{E}^{\omega_1}\right)_x - \beta\left(E\times\mathcal{E}^{\omega_1}\right)_y\right] C_{F,m}^{F',m'}\delta_{m,m'\pm1}\ \mathrm{e}^{\mathrm{i}\phi^{\omega_1}} \end{aligned} \tag{2.3}$$

where $\left|\overline{6S_{1/2}Fm}\right\rangle$ and $\left|\overline{7S_{1/2}Fm}\right\rangle$ represent the Stark mixed $6s$ and $7s$ states. α and β represent the scalar and vector transition polarizabilities, respectively. $C_{F,m}^{F',m'}$ are derived from the usual Clebsch-Gordon coefficients and are calculated using Ref. [30], $\mathbf{E}$ is the static applied electric field, and $\mathcal{E}^{\omega_1}$ and ϕ^{ω_1} are the electric field amplitude and phase of the driving laser field.

The coefficients α and β are calculated using a sum-over-states approach [31]. The equation to calculate the scalar coefficient is,

$$\begin{aligned} \alpha = \frac{1}{6}\sum_n \Bigg[&\left\langle 7S||r||nP_{1/2}\right\rangle\left\langle nP_{1/2}||r||6S\right\rangle\left(\frac{1}{E_{7S}-E_{nP_{1/2}}}+\frac{1}{E_{6S}-E_{nP_{1/2}}}\right) \\ &-\left\langle 7S||r||nP_{3/2}\right\rangle\left\langle nP_{3/2}||r||6S\right\rangle\left(\frac{1}{E_{7S}-E_{nP_{3/2}}}+\frac{1}{E_{6S}-E_{nP_{3/2}}}\right)\Bigg] \end{aligned} \tag{2.4}$$

and the vector term is

$$\begin{aligned} \beta = \frac{1}{6}\sum_n \Bigg[&\left\langle 7S||r||nP_{1/2}\right\rangle\left\langle nP_{1/2}||r||6S\right\rangle\left(\frac{1}{E_{7S}-E_{nP_{1/2}}}-\frac{1}{E_{6S}-E_{nP_{1/2}}}\right) \\ &+\frac{1}{2}\left\langle 7S||r||nP_{3/2}\right\rangle\left\langle nP_{3/2}||r||6S\right\rangle\left(\frac{1}{E_{7S}-E_{nP_{3/2}}}-\frac{1}{E_{6S}-E_{nP_{3/2}}}\right)\Bigg]. \end{aligned} \tag{2.5}$$

Here the denominators represent the difference in energy between the ground or excited state and the intermediate $nP_{1/2}$ or $nP_{3/2}$ level. The $\left\langle n'S||r||nP_{1/2}\right\rangle$ are reduced matrix elements connecting the ground or excited state (S) to an intermediate level (P). Clearly, the nearer P levels provide the strongest effect. Since there is large cancellation in the vector (β) term due to the minus sign, the β coefficient is smaller than α. The relative magnitude of α to β is $\left|\frac{\alpha}{\beta}\right| \approx 10$. Since α and β are calculated from the same reduced matrix elements and the uncertainty in the state energies is almost negligible, the relative uncertainty of α is around ten times smaller than for β. It is for this reason that a ratio measurement of $\frac{\alpha}{\beta}$ and a calculation of α is preferable to a direct calculation of β.[2]

It is important to note that there are several quantities that are commonly called polarizabilities. Even in this document alone there are three. They all quantify how an atom responds to an electric field. The polarizability is described/named by the type of electric field causing the effect and great care will be taken to distinguish the three polarizabilities as they come up. One interesting parallel between these polarizabilities is that they all can be calculated in a similar sum-over-states manner and the key difference is what is in the energy denominator. See Eqns. 2.4 or 2.5.

2.3.2 Magnetic dipole

The magnetic dipole transition is driven by the oscillating magnetic field of the excitation laser and its transition amplitude is as follows:

$$\begin{aligned} A_{M1}(F,m;F',m') = &\Bigg\{ \left(\hat{k}\times\mathcal{E}^{\omega_1}\right)_z \delta_{m,m'} \\ &+ \left[\pm\left(\hat{k}\times\mathcal{E}^{\omega_1}\right)_x + \mathrm{i}\left(\hat{k}\times\mathcal{E}^{\omega_1}\right)_y\right]\delta_{m,m'\pm1}\Bigg\} M_1 C_{F,m}^{F',m'} \mathrm{e}^{\mathrm{i}\phi^{\omega_1}} \end{aligned} \tag{2.6}$$

where $\hat{k}$ is the laser propagation direction and M_1 is the magnetic dipole matrix element. This moment is approximately 20 000 times larger than the PNC interaction. Careful field

[2]↑Both our group and Wieman's group have measured α/β to 0.1 %, so this is not too significant of a factor in the overall uncertainty in the calculation of Q_w.

alignment along with counter-propagating laser beams minimize systematic errors. This ratio M_1/β was measured by our group in 2013 using the two-pathway coherent control technique [4]. A modified version of this technique will be used for the PNC measurement proposed here.

Systematic errors due to the relative size of the PNC amplitude to the M_1 amplitude significantly complicate a precise measurement of the E_{PNC}/β. To circumvent this, Wieman's group utilized a high finesse cavity to ensure that the forward laser field exciting the $6s \rightarrow 7s$ transition was nearly equal to the backward laser field. These two beams produced oppositely signed M_1 amplitudes that tend to cancel very well and reduce systematics due to stray fields. Without this effect, stray magnetic fields would have to be reduced to the 20 000x1000 level, an intractable solution, for a 0.1% measurement of E_{PNC}/β. For our multi-wavelength approach, we require that all three laser fields be high finesse standing waves to produce the same effect. This requirement will be elaborated on in section 7.2.

The magnetic dipole contribution has a nuclear-spin-dependent contribution as well. Bouchiat and Piketty introduce a general phenomenological transition operator that is time-reversal invariant and parity conserving.[32] This operator is as follows,

$$\begin{aligned} T(n,n') = a_1 \boldsymbol{S}\cdot\boldsymbol{\mathcal{E}}\times k + \mathrm{i}a_2\left(\boldsymbol{S}\times\boldsymbol{I}\right)\cdot\left(\boldsymbol{\mathcal{E}}\times\boldsymbol{k}\right) \\ +\mathrm{i}a_3\left[\left(\boldsymbol{S}\cdot\boldsymbol{\mathcal{E}}\right)\left(\boldsymbol{I}\cdot\boldsymbol{k}\right)+\left(\boldsymbol{S}\cdot\boldsymbol{k}\right)\left(\boldsymbol{I}\cdot\boldsymbol{\mathcal{E}}\right)\right]. \end{aligned} \tag{2.7}$$

Bouchiat and Piketty substitute $a_1 \rightarrow -2M_1$, $a_2 \rightarrow -4M_1^{hf}/(2I+1)$, and $a_3 \rightarrow -E_2/2$. Here $\boldsymbol{S}$ and $\boldsymbol{I}$ represent the electronic and nuclear spin. When the nuclear spin of cesium is included, the transition operator simplifies to the following,

$$\begin{aligned} T(n,n') = -2M_1\boldsymbol{S}\cdot\left(\boldsymbol{\mathcal{E}}\times k\right) - \mathrm{i}(M_1^{hf}/2)\left(\boldsymbol{S}\times\boldsymbol{I}\right)\cdot\left(\boldsymbol{\mathcal{E}}\times\boldsymbol{k}\right) \\ -\mathrm{i}(E_2/2)\left[\left(\boldsymbol{S}\cdot\boldsymbol{\mathcal{E}}\right)\left(\boldsymbol{I}\cdot\boldsymbol{k}\right)+\left(\boldsymbol{S}\cdot\boldsymbol{k}\right)\left(\boldsymbol{I}\cdot\boldsymbol{\mathcal{E}}\right)\right]. \end{aligned} \tag{2.8}$$

This equation includes a hyperfine changing magnetic dipole contribution as well as an electric quadrupole moment. The relative strength of the M_1^{hf} to M_1 is $\left|\frac{M_1^{hf}}{M_1}\right| = 0.1906\ (5)$ [33]. A list of all the weak transitions and their relative strengths are recorded in table 2.1

2.3.3 Electric quadrupole

The $6s_{1/2} \rightarrow 7s_{1/2}$ line also has a small electric quadrupole (E_2) amplitude. This E_2 moment is weakly allowed due to hyperfine coupling between $S_{1/2}$ and $D_{3/2}$ states [32]. Bouchiat and Guena reanalyzed a series of inconsistent measurements on the $6s \rightarrow 7s$ transition and show better agreement among the measurements when the E_2 moment was included[34]. Later, Bennet combined their results in [35] with the results of Gilbert [36] and determine $E_2/M_1^{hf} = 53(3) \times 10^{-3}$. Derevianko *et al.* [37] write the transition amplitude for the quadrupole moment as;

$$\begin{aligned} A_{E_2}(F,m;F',m') &= \left\langle 7s\ F',m'\right| \left(-\mathrm{e}\vec{r}\cdot\mathcal{E}^{\omega_1}\right)\left(\hat{k}\cdot\vec{r}\right)\left|6s\ F,m\right\rangle \\ &= (-1)^{F'-m'}\begin{pmatrix} F' & 2 & F \\ -m' & q & m \end{pmatrix}(2F+1)^{1/2} \\ &\times (2F'+1)^{1/2}\begin{Bmatrix} J & F & I \\ F' & J' & 2 \end{Bmatrix} E_2\ \mathcal{E}^{\omega_1}, \end{aligned}$$

where E_2 is the electric-quadrupole moment, () and {} brackets denote the Wigner 3-j and 6-j symbols. This electric quadrupole moment is weakly allowed, but will drive only $\Delta m = \pm 2$ transitions in our field geometry. Since our interaction will be on a $\Delta m = \pm 1$ transition, the quadrupole moment will not interfere and won't affect the measurement.

2.3.4 PNC interaction

Opposite parity states mixed by the weak interaction permit electric dipole transitions between the $6s$ and $7s$ states. This parity non-conserving weak amplitude is:

Table 2.1. Strength of the weak transitions relative to the Stark vector polarizability, β. The ratios are given in terms of the static electric field required to make the β polarizability as strong as the transition moment of interest. Both the α and β transitions scale as the electric field and that ratio is unitless.

Transition	Ratio
α	-9.902(9) [5]
M_1	-29.48(7) V/cm [35]
M_1^{hf}	-5.6195(91) V/cm [35]
E_2	-0.298(17) V/cm [35]
$Im\{E_{PNC}\}$	-1.5935(56) mV/cm [1]

$$A_{PNC}(F,m;F',m') = \left[\mathcal{E}_z^{\omega_1}\delta_{m,m'} + \left(\pm\mathcal{E}_x^{\omega_1} + \mathrm{i}\mathcal{E}_y^{\omega_1}\right)\delta_{m,m'\pm1}\right]\mathrm{i}Im\left\{E_{PNC}\right\}C_{F,m}^{F',m'}\mathrm{e}^{\mathrm{i}\phi^{\omega_1}} \quad (2.9)$$

where E_{PNC} is the PNC matrix element produced by the electro-weak interaction between the electrons and nucleons in the cesium atom. The relative strength of the E_{PNC} to the vector Stark polarizability (E_{PNC}/β) has been previously measured and reported to 0.35 % uncertainty. Further measurement of this ratio along with theoretical calculations allow precise determinations of the weak charge of the nucleus and could elucidate new physics or physics not included in the standard model. We plan to measure E_{PNC}/β to greater precision than that of Wieman's group using our coherent control technique.

2.3.5 Two-photon interaction

The above transitions are extremely weak and measurements of their amplitudes benefit from interference techniques. This requires a stronger transition with which the weaker transition interferes. We choose to interfere these weak transitions with the two-photon transition coupling the $6s$ and $7s$ state. The two-photon transition amplitude is;

$$\begin{aligned} A_{2p}(F,m;F',m') = \Bigg\{&\left[\tilde{\alpha}\mathcal{E}^{\omega_2}\cdot\mathcal{E}^{\omega_3}\delta_{F,F'} + \mathrm{i}\tilde{\beta}\left(\mathcal{E}^{\omega_2}\times\mathcal{E}^{\omega_3}\right)_z C_{F,m}^{F',m'}\right]\delta_{m,m'} \\ &+\left[\pm\mathrm{i}\tilde{\beta}\left(\mathcal{E}^{\omega_2}\times\mathcal{E}^{\omega_3}\right)_x - \mathrm{i}\tilde{\beta}\left(\mathcal{E}^{\omega_2}\times\mathcal{E}^{\omega_3}\right)_y\right]C_{F,m}^{F',m'}\delta_{m,m'\pm1}\Bigg\}\mathrm{e}^{\mathrm{i}(\phi^{\omega_2}+\phi^{\omega_3})} \end{aligned} \quad (2.10)$$

where $\mathcal{E}^{\omega_2}$ and $\mathcal{E}^{\omega_3}$ are the laser electric field amplitudes for the two two-photon beams. The scalar coefficient $\tilde{\alpha}$ and vector coefficient $\tilde{\beta}$ characterize the strength of the two-photon transition when the two laser beam polarizations are parallel or perpendicular, respectively. The coefficients $\tilde{\alpha}$ and $\tilde{\beta}$ are calculated using a sum-over-states approach in a similar manner by which the Stark scalar and vector transition polarizabilities are calculated [31]. The equation to calculate the scalar coefficient is,

$$\tilde{\alpha} = \frac{1}{6\hbar}\sum_n \left[\left\langle 7S||r||nP_{1/2}\right\rangle \left\langle nP_{1/2}||r||6S\right\rangle \left(\frac{1}{\omega_3 - \omega_{nP_{1/2}}} + \frac{1}{\omega_2 - \omega_{nP_{1/2}}}\right) \right. \\ \left. - \left\langle 7S||r||nP_{3/2}\right\rangle \left\langle nP_{3/2}||r||6S\right\rangle \left(\frac{1}{\omega_3 - \omega_{nP_{3/2}}} + \frac{1}{\omega_2 - \omega_{nP_{3/2}}}\right) \right]. \tag{2.11}$$

To calculate the vector term, the following equation is used,

$$\tilde{\beta} = \frac{1}{6\hbar}\sum_n \left[\left\langle 7S||r||nP_{1/2}\right\rangle \left\langle nP_{1/2}||r||6S\right\rangle \left(\frac{1}{\omega_3 - \omega_{nP_{1/2}}} - \frac{1}{\omega_2 - \omega_{nP_{1/2}}}\right) \right. \\ \left. + \frac{1}{2}\left\langle 7S||r||nP_{3/2}\right\rangle \left\langle nP_{3/2}||r||6S\right\rangle \left(\frac{1}{\omega_3 - \omega_{nP_{3/2}}} - \frac{1}{\omega_2 - \omega_{nP_{3/2}}}\right) \right]. \tag{2.12}$$

Here the state energies have been rewritten in terms of optical frequencies and the ω_2 and ω_3 terms represent the two optical frequencies driving the two-photon transition. By inspection of equation 2.12, it is apparent that $\tilde{\beta}$ transitions are not possible with equal photons ($\omega_2 = \omega_3$). With only a single laser source, $\Delta F = \pm 1$ transitions are not possible. This would require us to measure E_{PNC}/α instead of E_{PNC}/β. A measurement of E_{PNC}/β is preferable since it allows a measurement of the NSD amplitude and would allow direct comparison with the measurement by Wood *et al.* [1]. Also, a measurement of E_{PNC}/β is more practical since β is ten times smaller than α. A relative measurement of E_{PNC}/β would then be ten times less susceptible to stray electric fields compared to a ratio measurement of E_{PNC}/α.

Since we want to interfere a E_{PNC} with β, we must drive this two-photon transition with two unequal photons. Equation 2.12 shows that we can enhance this transition strength by choosing a laser source (ω_2 or ω_3) such that it is near an intermediate resonance ($nP_{3/2}$ or $nP_{1/2}$). The caveat to this technique is that the laser frequency should not overlap with the intermediate resonance at all since that would ruin the coherence and effectively destroy the interference. It is also important to note that the smaller the detuning from resonance, the better the laser frequency must be stabilized since the transition amplitude may vary significantly if the detuning is small.

2.4 Coherent control

For the PNC measurement, we plan to interfere the two-photon and Stark transitions with the very weak PNC transition. In Fig. 2.5, we show the geometry of the static fields necessary to drive select transitions. In the figure, all lasers propagate in the $\hat{y}$ direction and the atomic beam propagates in the $\hat{x}$ direction. The symbol $\vec{\mathcal{E}}_{laser}$ represents the electric field of the driving excitation laser and $\vec{B}$ and $\vec{E}$ are the applied magnetic and electric fields, respectively. This configuration differs from the Boulder group in that the weak signal is amplified by the stronger two-photon transition instead of just the Stark induced transition. The scheme is also modified from what D. Antypas used in the measurement of M_1/β. Antypas drove the two-photon transition with equal 1079 nm photons where we will excite the transition with unequal photons. This will allow measurements of spin-dependent PNC effects. As an added bonus, the unequal photons will couple to the intermediate $6p_{3/2}$ state more strongly and will amplify the two-photon signal.

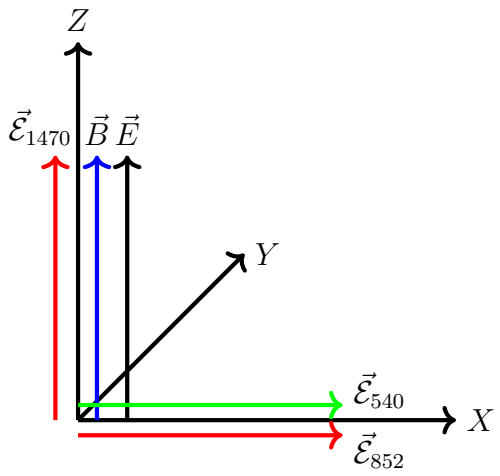

Figure 2.5. Field geometry for the PNC measurement

Using these fields in Fig. 2.5, most of the terms are zero in equations 2.3, 2.9, and 2.10. The sum of the remaining terms is below;

$$A = A_{2p} + A_{St} + A_{PNC} = \Big(- \mathrm{i}\tilde{\beta}\mathcal{E}^{\omega_2}\mathcal{E}^{\omega_3} C_{F,m}^{F',m'} \mathrm{e}^{\mathrm{i}(\phi^{\omega_2}+\phi^{\omega_3})} - \beta E \mathcal{E}^{\omega_1} C_{F,m}^{F',m'} \mathrm{e}^{\mathrm{i}\phi^{\omega_1}} \\ \pm \mathrm{i}\mathcal{E}^{\omega_1} Im\left\{E_{PNC}\right\} C_{F,m}^{F',m'} \mathrm{e}^{\mathrm{i}\phi^{\omega_1}} \Big) \delta_{m,m'\pm 1} \tag{2.13}$$

The phases of each of the optical fields are included here and are critical in the coherent control technique. If we ignore the extremely small interference between the PNC and Stark terms as well as the DC offset of the Stark and PNC terms, the observed transition will be;

$$\begin{aligned} A^2 \approx & \left(\tilde{\beta}\mathcal{E}^{\omega_2}\mathcal{E}^{\omega_3} C_{F,m}^{F',m'}\right)^2 \\ & - \mathrm{i}\tilde{\beta}\mathcal{E}^{\omega_2}\mathcal{E}^{\omega_3} C_{F,m}^{F',m'} \mathrm{e}^{\mathrm{i}(\phi^{\omega_2}+\phi^{\omega_3})} \left(-\beta E \mathcal{E}^{\omega_1} C_{F,m}^{F',m'} \mathrm{e}^{-\mathrm{i}\phi^{\omega_1}} \mp \mathrm{i}\mathcal{E}^{\omega_1} C_{F,m}^{F',m'} \mathrm{e}^{-\mathrm{i}\phi^{\omega_1}} Im\left\{E_{PNC}\right\}\right) \\ & + \mathrm{i}\tilde{\beta}\mathcal{E}^{\omega_2}\mathcal{E}^{\omega_3} C_{F,m}^{F',m'} \mathrm{e}^{-\mathrm{i}(\phi^{\omega_2}+\phi^{\omega_3})} \left(-\beta E \mathcal{E}^{\omega_1} C_{F,m}^{F',m'} \mathrm{e}^{\mathrm{i}\phi^{\omega_1}} \pm \mathrm{i}\mathcal{E}^{\omega_1} C_{F,m}^{F',m'} \mathrm{e}^{\mathrm{i}\phi^{\omega_1}} Im\left\{E_{PNC}\right\}\right) \end{aligned} \tag{2.14}$$

The first term here represents a DC offset of the observed signal due to the two photon absorption and the second two terms are dependent on the relative phase. The equation above can be simplified to;

$$\begin{aligned} A^2 \approx & \left(\tilde{\beta}\mathcal{E}^{\omega_2}\mathcal{E}^{\omega_3} C_{F,m}^{F',m'}\right)^2 \\ & + 2\tilde{\beta}\mathcal{E}^{\omega_1}\mathcal{E}^{\omega_2}\mathcal{E}^{\omega_3} \left(C_{F,m}^{F',m'}\right)^2 \sqrt{\beta^2 E^2 + (Im\left\{E_{PNC}\right\})^2} \sin(\phi^{\omega_2} + \phi^{\omega_3} - \phi^{\omega_1} + \Phi(E)) \end{aligned} \tag{2.15}$$

This observed signal has a large DC offset and a modulation term that is proportional to the product of the weak amplitudes and the much stronger two-photon amplitude. We vary the modulation by shifting the optical phase of the driving laser radiation. This was previously completed in our lab by passing one of the beams through a rotating window. As the window rotated, the apparent path length changed and allowed precise phase modulation. This phase modulation led to a sinusoidally varying interference that was later analyzed to

determine the amplitude and phase. The technique we intend to use is facilitated through our locking scheme and will be discussed later.

3. EXPERIMENTAL APPARATUS

This section will detail the experimental apparatus that has been in part used for weak signal detection [21] and will be configured to detect the parity nonconserving weak interaction. Fig. 3.1 gives an overview of the experimental configuration. This general overview illustrates the vacuum system and the three regions within. Atoms travel from the oven through the preparation region where they are spin polarized and then through the interaction region where they are driven through the $6s \rightarrow 7s$ transitions mentioned above. The final region is used to detect the atoms that interact by driving them through a cycling transition on a previously emptied hyperfine level and collecting the fluorescence. The following sections will discuss this process in detail as well as other techniques required for the PNC measurement.

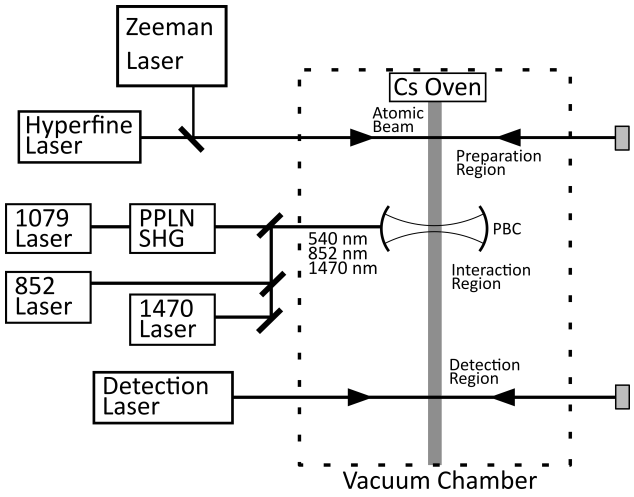

Figure 3.1. Drawing of experimental diagram. The abbreviated elements are; PPLN-periodically poled lithium noibate, PBC-power build-up cavity, SHG-second harmonic generation

3.1 Vacuum Chamber

The coherent control technique to study atomic parity violation utilizes an atomic beam generated in a vacuum chamber to carry out measurements. The vacuum chamber in which we generate a cesium beam is a large aluminum box measuring $50 \times 55 \times 40$ cm, see Fig. 3.2.

The chamber is large enough to contain all necessary magnetic field coils and electric field plates, photodetector, and a pair of cryogenically cooled copper baffles. It is notable that the chamber is aluminum as opposed to the more conventional options. This is necessary to reduce stray magnetic fields to a level as low as possible. The chamber is closed with a heavy aluminum lid that rests on an o-ring for a vacuum seal. The lid can easily be removed (with help) to allow access to the experimental components within the vacuum.

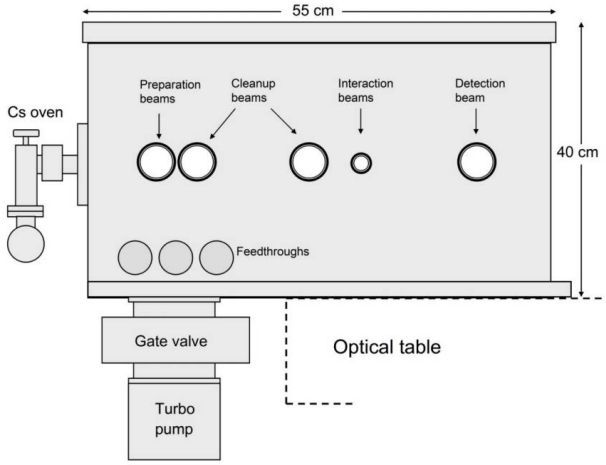

Figure 3.2. Illustration of the vacuum chamber from [21].

The chamber is evacuated by an Edwards STP-451 turbomolecular pump (480 L/sec) that is magnetically levitated to increase bearing life. This turbopump is backed by a mechanical roughing pump (Alcatel 2012) that is necessary to start a vacuum from atmospheric pressure. A pneumatic gate valve separates the turbopump from the main chamber. Along with a separate valve and roughing pump, the pneumatic valve allows us to open, close, and repump the chamber while the turbo pump rotates. This reduces the number of accelerations and increases the lifespan of the pump. The fast pumping speed of the turbopump and the lack of need for an ultrahigh vacuum allows us to pump back down to a base pressure in 12 to 24 hours as opposed to weeks or months for our ultra-high vacuum friends. The base pressure for this system is approximately 5×10^{-7} Torr. To reduce the clouding of the atomic cesium inside the chamber, a pair of liquid nitrogen cooled copper baffles act as a secondary pump that further reduces the pressure by as much as an order of magnitude. The copper baffles consist of a stainless steel tank with a large copper plate affixed to its surface. The pair of

baffles are on opposite sides of the chamber. The atomic beam passes through an aperture (10 mm wide, 3 mm tall) in the first copper baffle that defines the geometry of the atomic beam and the opposite baffle acts as an atomic beam dump to further reduce clouding of the chamber. The chamber contains four pairs of 50 mm (not 2 in.)[1] antireflection coated viewports for 852 nm light and a pair of 1 in. dual antireflection coated windows for 540 nm and 1079 nm. The chamber also contains eight other ports that allow us to connect a variety of other electronic feedthroughs for electric field biasing, magnetic field generation, and weak signal detection.

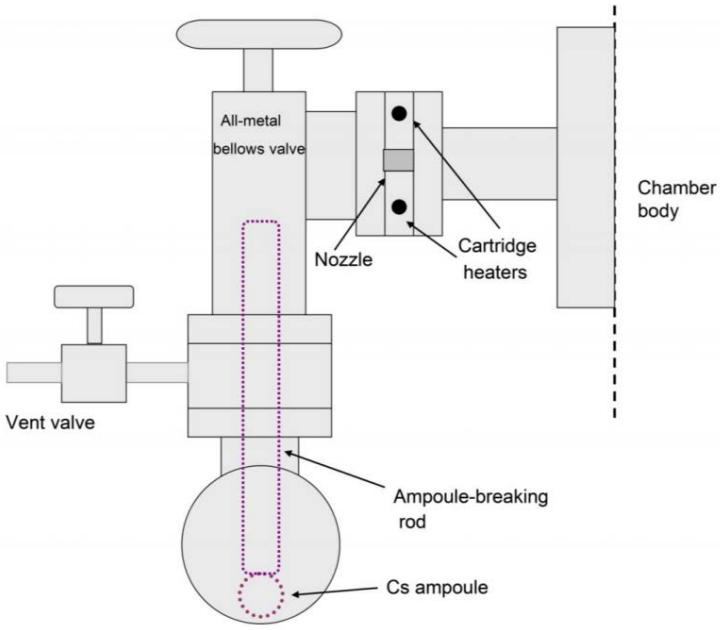

Figure 3.3. Illustration of the vacuum chamber oven/nozzle assembly. Image from [21]

The oven and nozzle assembly consists of a tee, bellows valve, rod, and nozzle (see Fig. 3.3). The tee is capped on two ends and contains the 5g cesium ampoule. We are able to load the cesium ampoule by removing one of these end caps and opening the bellows valve. Once the cesium ampoule is placed under the rod, the tee is recapped and the chamber is evacuated. By closing the bellows valve, we crush the ampoule to release the cesium safely. A pair of cartridge heaters are used to heat the nozzle to $\sim$170 $^{\circ}C$ and heating tape is used to control the temperature of the oven in the range of 130 to 160 $^{\circ}C$. The

[1] A 2 in window will just barely not fit in the opening.

nozzle temperature is kept well above the oven temperature to avoid clogging the nozzle and to minimize clouding in the chamber. We vary the atomic beam density by adjusting the temperature of the oven. The oven components are relatively heavy and are wrapped in multiple layers of aluminum foil to reduce cesium beam density drifts. The atomic beam is steady to <1% in an hour. Since relative measurements are completed in seconds, atomic beam drift is negligible. Occasionally it is necessary to open the chamber after having filled the oven with a fresh charge of cesium. In this instance, a vent valve is used to back fill the oven with dry argon or nitrogen gas to reduce cesium oxidation.

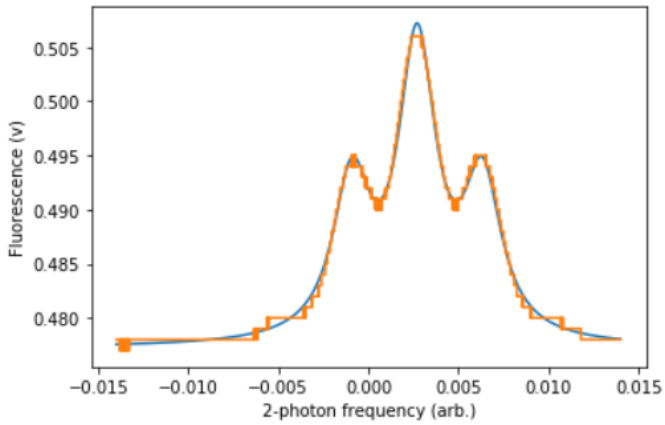

Figure 3.4. 2-photon spectrum illustrating the atomic beam divergence. Orange represents the cesium fluorescence as the atoms are driven through the $6s \rightarrow 7s$ transition. The Blue trace is the fit that includes the sidebands of the laser.

A collimated atomic beam is generated by effusing cesium through the heated nozzle constructed of many thin stainless steel capillaries (1 cm long, 0.8 mm I.D.). The geometry of the nozzle along with the temperature of the oven defines the collimation of the atomic beam. The beam divergence has been measured by Dionysios to be 38 mrad (14 MHz for our geometry) [21] and has since been remeasured. This was conducted by sweeping a laser at 1079 nm across the $6s \rightarrow 7s$ transition while modulating the laser at 20 MHz (higher than the linewidth of the transition). The fluorescence, see Fig. 3.4, is then fit to determine the sideband spacing (mod. frequency) and linewidth. Without knowing the scan depth, the relative spacing of the sidebands to the linewidth allows a decent determination

of the linewidth. Here we measure the linewidth to be 14 MHz in the atomic beam and 6.3 MHz[2] in a vapor cell. The broadening in the beam is primarily due to the atomic beam divergence. The natural linewidth along with transit time broadening dominates in the cell. Further improvement of atomic beam collimation has been achieved by using a down-stream collimator composed of microscope slides and cover slips. This reduces the beam density and is not typically used unless necessary. The well collimated atomic beam travels from left to right in Fig. 3.2 and is centered vertically on the optical viewports. Through these viewports, laser beams intersect the atomic beam at right angles to drive select transitions.

3.2 External cavity diode laser

To drive atomic transitions in cesium, we choose to use external cavity diode lasers (ECDL). ECDLs are much cheaper and easier to maintain than solid state lasers or dye lasers. This is at the expense of power and ease of tuning. ECDLs consist of a diode laser that has an external diffraction grating that provides feedback to stabilize and narrow the laser output frequency. This is commonly done in either a Littrow or a Littman-Metcalf configuration (see Fig. 3.5). In a typical Littrow configuration, light from a laser diode is collimated by an antireflection coated aspheric lens and then is incident on a diffraction grating. The first order diffracted light is directed back towards the laser diode to provide feedback. Since the diffraction angle is wavelength dependent, the tuning angle of the diffraction grating allows coarse adjustment with a tuning screw and relatively fine adjustment with a piezoelectric element. A piezo electric element (PZT) can be placed between the frame on an optical mount that the grating rests on and the adjustment screw (see Fig 3.6 for clarity). A voltage applied to this PZT changes its length and tunes the laser frequency. The bandwidth of this configuration is limited to below the resonant frequency of the piezo-mount system and is in the range of a few kilohertz. The Littman-Metcalf configuration is similar to the Littrow configuration except that the first order diffraction is directed onto a mirror and then the mirror is rotated to tune the wavelength. The cavity then consists of the diode, grating, and mirror as opposed to just the diode and grating. This configuration allows a wide tuning

[2]↑This linewidth is measured using two-photon absorption in a heated vapor cell using focused and retro-reflected beams at 1079 nm to reduce residual Doppler broadening.

range without changing the angle of the output beam, which reduces alignment errors when tuning.

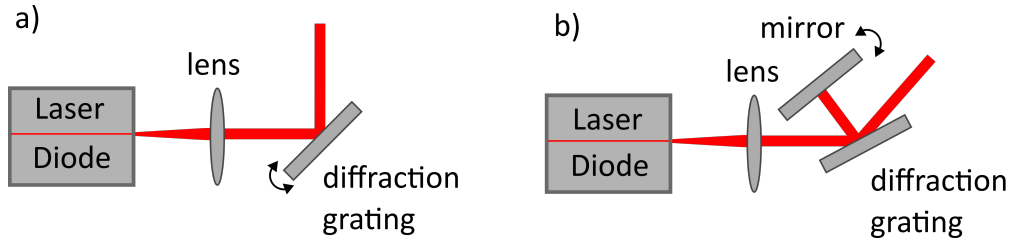

Figure 3.5. Illustration of a) a Littrow style ECDL and b) a Littman-Metcalf style ECDL Image from [21]

A more realistic example of a Littrow ECDL is depicted in Fig. 3.6. Here we see an external cavity formed by the laser diode and grating. Supporting these elements are the base plate and optic mount. Due to the coefficient of thermal expansion (CTE) of these elements as well as the diodes own temperature dependent gain curve, temperature control to the few mK level is critical. The diode gain curve can shift by 100 MHz/mK [38]. Without precise temperature control, atomic spectra can walk right off of the scan.[3]

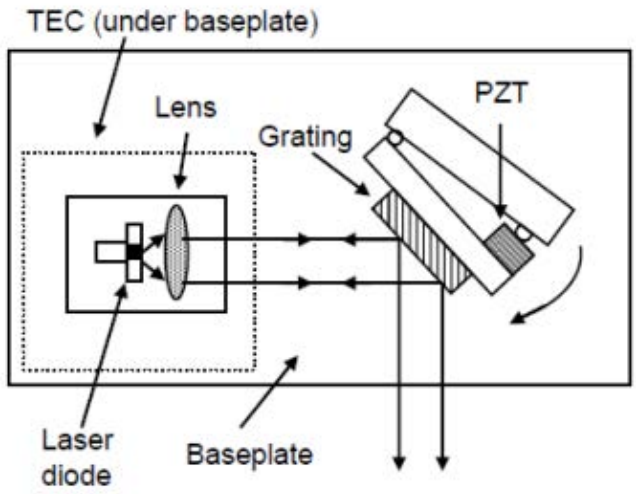

Figure 3.6. Illustration of and external cavity diode laser. Image from [21]

[3]↑There have been instances in our lab where cold air blowing directly down on the lasers and driving electronics have shifted spectra around. This was circumvented by plastic sheets that divert air across the room instead of downward.

Faster tuning of an ECDL is possible through the modulation of the driving laser diode current. The current through the diode laser affects the index of refraction inside the diode laser chip, which directly affects the output frequency of the laser. Along with that, higher currents affect the temperature of the diode chip which shifts the frequency as well. Since noise on the current will produce unwanted amplitude and frequency modulation, diode lasers require exceedingly quiet current supplies to reduce laser linewidth. Tuning sensitivity is typically around 3 GHz/mA [38]. Sub-MHz linewidths would require much less than 300 nA of RMS current noise. This does not include longer term effects such as acoustic vibrations and air pressure changes.[4] Modulation of the diode current is often necessary to cancel out these fluctuations and to apply sidebands to the laser output. The modulation rate of the diode laser depends on the technique in which the modulation is applied. Directly connecting the diode laser to a bias-tee allows fast AC modulation (a few GHz is possible). A safer way to modulate the diode laser current is typically built into the driving circuitry of the diode laser current driver. Commercial diode laser controllers typically have modulation bandwidths on the order of a few hundred kilohertz or even slower. This is insufficient if it is necessary to reduce the linewidth of a fairly noisy laser. Libbrecht and Hall [39] have published designs for low-noise fast laser diode current controllers that meet and exceed specifications for many commercial supplies.[5] We have utilized these designs as well as have made other suggested modifications to drive all of our homemade ECDLs [39–42].

3.3 Saturated absorption spectroscopy

Due to thermal motion of an atomic vapor in a vapor cell, simply passing a laser beam through the cell will result in a Doppler broadened spectrum. This is due to the apparent frequency of the laser radiation in the frame of the atom. In the atom's frame of reference, the laser frequency is shifted to;

$$\omega' = \omega - \vec{k} \cdot \vec{v} \tag{3.1}$$

[4]↑Laser manufacturers can be deceptive in their specifications of linewidth by quoting linewidths for extremely short time scales or by just quoting a linewidth without a time.
[5]↑Many commercial current controllers don't need or want this fast modulation since it increases noise and they have modulation ports built directly into the laser head.

where $\vec{k}$ is the laser wave vector and $\vec{v}$ is the atom's velocity. This broadening leads to a Doppler width;

$$\omega_D = \omega_0 \sqrt{\frac{8k_B T ln2}{mc^2}} \tag{3.2}$$

where ω_0 is the rest frequency of the transition and k_B is Boltzman's constant [43]. For the cesium D2 line, this width is ∼400 MHz at room temperature. Doppler broadening completely hides the hyperfine structure that we wish to stabilize our lasers to. To narrow this observed linewidth, atoms need to be probed with counter propagating beams. One technique that accomplishes this is saturated absorption spectroscopy (SAS), illustrated in Fig. 3.7. Here, a pump beam depletes atoms from the ground state of a particular velocity subgroup while on resonance. When the weaker probe beam interacts with the same velocity group of atoms, fewer atoms are available to absorb the light and the probe beam has larger transmission. Off resonance, the pump beam is not saturating the same velocity group that the probe beam is interrogating and probe beam absorption increases which decreases transmission. Typically, a second probe beam is used to subtract off the Doppler broadened dip. The result is a relatively flat spectrum with peaks at each transition.

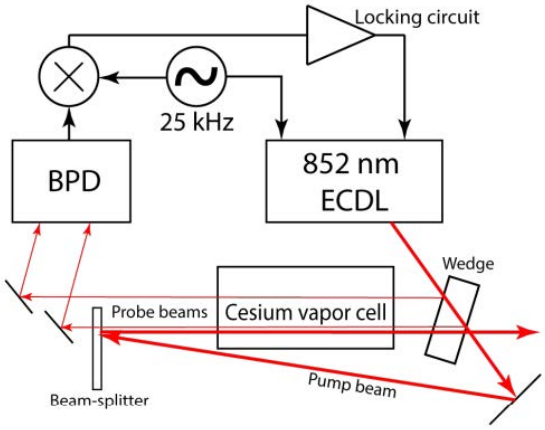

Figure 3.7. Diagram of a saturated absorption setup. BPD-balanced photodetector. Image from [22].

An example spectrum of saturated absorption spectroscopy for the $6s\ F = 4 \rightarrow 6p_{3/2}\ F = 3, 4, 5$ transitions in cesium is shown in Fig. 3.8. Here the upper trace includes the three hyperfine transitions as well as their cross over resonances, which occur exactly half way between each peak. Below the spectrum is the error signal (i.e. the derivative spectrum) that we stabilize the lasers to.

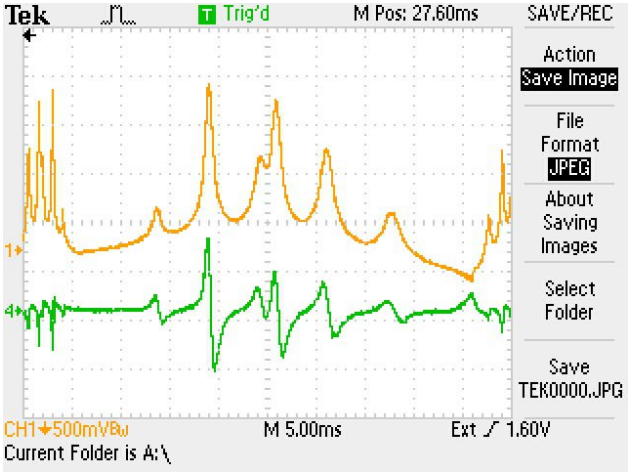

Figure 3.8. Saturated absorption spectroscopy signal

An example peak is illustrated in Fig. 3.9 (left) as well as its derivative (right). When stabilizing a laser, a servo needs a region where the error signal is monotonic. This allows the servo to know which way to correct frequency changes. We can electronically derive the dispersion shape in Fig. 3.9 (right) by dithering the laser frequency near 25 kHz and then multiplying the spectrum by the dither via a mixer. The output of the mixer is lowpass filtered and used to stabilize the laser. In this configuration, the three ECDLs stabilized via SAS stay locked for at least several hours, if not all day.

3.4 Pound-Drever-Hall

Direct current modulation and grating position can be used to stabilize and narrow the frequency of an ECDL. The extent to which the frequency is stabilized and the linewidth is narrowed depends on the speed of the feedback, the sharpness of the error signal, and the stability of the reference used to derive the error signal. Previously, we have discussed

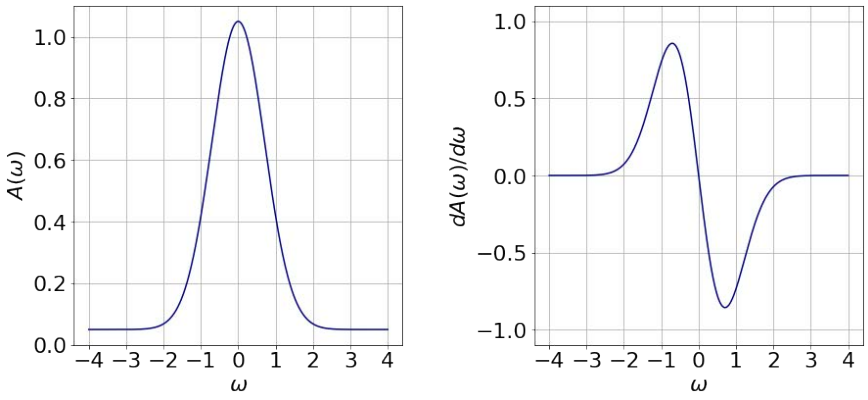

Figure 3.9. Plot illustrating top-of-fringe locking.

using atomic resonances as a means to stabilize the frequency, but they are limited due to the linewidth of the transition. To further narrow the linewidth of a laser, the laser can be stabilized to a narrow Fabry-Perot interferometer using Pound-Drever-Hall (PDH) locking. The PDH technique is commonly used to stabilize a laser to a Fabry-Perot cavity due to the high bandwidth and intensity independence compared to side-of-fringe locking or low-bandwidth top-of-fringe locking.

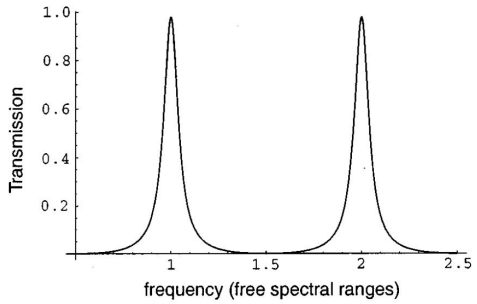

Figure 3.10. Transmission through a Fabry-Perot cavity with a finesse of about 12 as a function of laser frequency. Image from [44]

The frequency discriminator in PDH locking is the Fabry-Perot optical cavity. When light is incident on one of the mirrors of an optical cavity, most of the light is reflected unless its frequency is nearly equal to an integer multiple of the cavity's free spectral range, $FSR = c/2nL$ where n is the index of refraction of the material and L is the distance

between the mirrors. Fig. 3.10 shows the transmission of light through an optical cavity with a finesse of about 12 as the laser frequency is swept.[6] Prior to PDH, it was common to stabilize the frequency of a laser by using the side of one of these fringes as a locking point. By measuring the transmitted light at one of these points, a small frequency change will lead to a proportional change in transmitted light. This change can be measured and an appropriate servo response can correct the frequency error. Unfortunately, this technique cannot distinguish between intensity and frequency fluctuations of the laser. PDH uses the optical cavity as a frequency discriminator when on resonance and is much less susceptible to intensity fluctuations.

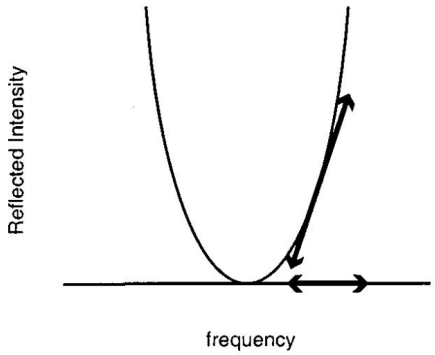

Figure 3.11. Reflected light intensity as a laser frequency is swept across an optical cavity resonance. Image from [44]

To stabilize the laser on resonance with an optical cavity, a problem is quickly apparent for the servo. When on resonance, each direction the servo can push the laser reduces cavity transmission (and increases the reflection). This concept is illustrated in Fig. 3.11. To produce a signal that a servo can understand, the laser frequency needs to be modulated. This modulated light is reflected off of an optical cavity and is detected with a fast photodiode. This signal is then mixed with the same modulation source to produce a dc response that is proportional to the slope of the reflection curve with a zero crossing at maximal transmission. When modulating at a low frequency compared to the bandwidth of the cavity, the dispersion shape looks similar to Fig. 3.12. This error signal can be used to stabilize the

[6]↑The cavity length can also be swept using a mirror mounted on a piezoelectric transducer. A finesse of 12 is small for typical applications and would correspond to a two mirror cavity with a mirror reflectivity of around 77%.

laser frequency in a bandwidth less than the modulation frequency. This technique can be improved to increase the locking bandwidth and increase the slope of the error signal near resonance by modulating the phase faster than the bandwidth of the cavity.

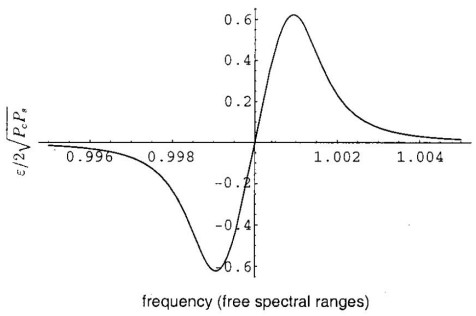

Figure 3.12. Error signal for top-of-fringe locking with a low modulation frequency. Image from [44]

To modulate a laser fast enough for PDH stabilization, an EOM is typically used to modulate the phase. It is possible to modulate the frequency of the laser by modulating the current, but this also imparts intensity fluctuations as well. With a high frequency modulation signal passing to an EOM, the electric field of the laser beam becomes

$$E = E_0 \mathrm{e}^{\mathrm{i}(wt + \eta sin\ \Omega t)}$$

where η is the modulation depth and Ω is the modulation frequency. This exponential can be expanded with Bessel functions to

$$E \approx E_0[J_0(\eta)\mathrm{e}^{\mathrm{i}wt} + J_1(\eta)\mathrm{e}^{\mathrm{i}(w+\Omega)t} - J_1(\eta)\mathrm{e}^{\mathrm{i}(w-\Omega)t}]$$

where the modulation index is small so that most of the power is in the carrier, $\mathrm{e}^{\mathrm{i}wt}$, and the first order sidebands, $\mathrm{e}^{\mathrm{i}(w\pm\Omega)t}$. When this fast modulated (much faster than the bandwidth of the cavity) light is incident on an optical cavity, the cavity does not have a chance to respond quickly enough. Instead of modulating the intensity of light in the cavity, the cavity acts as a reservoir frequency discriminator to average out the incoming signal. As the laser frequency is swept across the cavity resonance, the laser sidebands beat against the averaged

signal in the cavity at the modulation frequency, Ω. This averaged cavity signal allows a servo to correct for frequency fluctuations of the laser that are faster that the cavity can respond. When the reflected signal is then mixed with the modulation frequency, the phase of the beat signal between the sidebands and the light in the cavity acts as an error signal with a very large slope near resonance. This error signal is illustrated in Fig. 3.13. Here the slope is much higher than that of the slow frequency modulation and the capture range is also extended. This allows extremely tight and stable locks to cavity resonances that also narrow the linewidth of the laser.

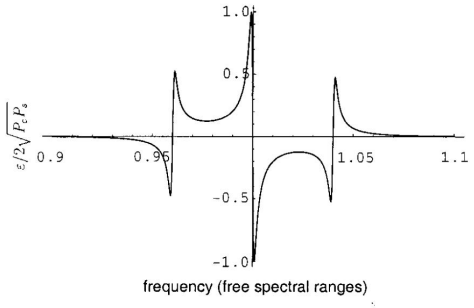

Figure 3.13. Error signal for Pound-Drever-Hall locking with a high modulation frequency. Image from [44]

The experimental setup to perform PDH frequency stabilization is illustrated in Fig. 3.14. Here the rf source provides the modulation signal to the electro-optic phase modulator (EOM) and to a phase shifter (ϕ) and mixer. The laser beam passes through the EOM, a polarizing beam splitter (PBS), and quarter-wave plate (QWP). This beam is coupled into the cavity and the reflected beam travels back through the QWP and is then deflected by the PBS onto a photodiode (PD). The photodiode signal is amplified and mixed down with the phase shifted modulation signal. The phase shifter is necessary to align the phase of the beat signal with the EOM modulation to maximize the error signal.[7] This mixed down signal is then low-pass filtered (LPF) and then sent to a servo to control the laser frequency. For our configuration, we are servoing the laser current to eliminate fast frequency fluctuations and the piezo to account for slow drifts.

[7]↑A length of cable is also a phase shifter.

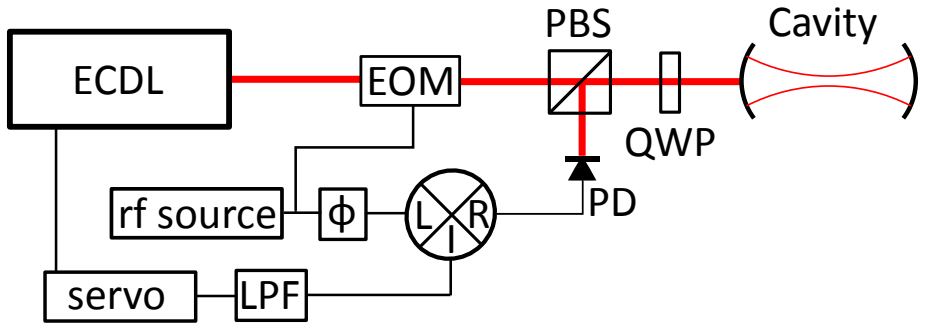

Figure 3.14. Pound-Drever-Hall experimental configuration. The laser beam is phase modulated in an EOM and reflected off on a F-P cavity. The reflected light is collected by a fast photodiode and mixed with the modulation frequency to produce an error signal.

To drive the single photon $6s \rightarrow 7s$ transition, we have purchased a commercial laser at 1079 nm and servo and have integrated them into our experiment. To determine the quality of the laser lock to the cavity, we observe the laser noise spectrum centered at the EOM frequency. This signal is observed by placing a 20 dB (1%) coupler after the photodiode and sending this signal to a spectrum analyzer. The noise could be observed at DC, but $1/f$ noise would be significant and the noise floor would be high. The laser noise spectrum is illustrated in Fig. 3.15. The spectrum is centered around 20 MHz, the span of the spectrum analyzer is set to 10 MHz, and the resolution bandwidth is 1 kHz. The noise is greatly suppressed from the carrier out to a few MHz. When the frequency fluctuations are faster than the time it takes for the error signal to reach the servo and for the servo to respond, the servo starts to add noise. This characteristic frequency is the servo bandwidth. To avoid the system from oscillating, the gain on the servo needs to fall below 0 dB before the servo bandwidth.

3.5 Optical pumping and detection

Interference of the two-photon transition with one of the weak amplitude transitions (β-Stark, M_1, and E_{PNC}) is dependent on the particular Zeeman sublevel the atoms are in.

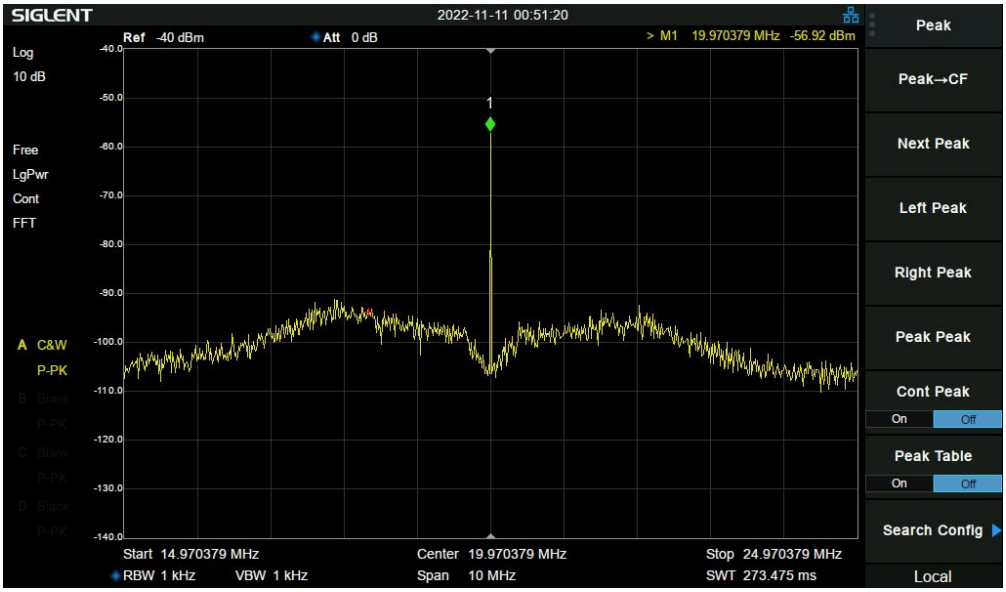

Figure 3.15. Laser noise spectrum centered at the EOM modulation frequency. The peak in the center is the residual amplitude modulation (RAM) in the laser. This is caused by a slight misalignment of the laser polarization into the EOM. This causes the electro-optic phase modulator to act a bit like an electro-optic amplitude modulator. This RAM could also be caused by etalon effects in the EOM crystal. Either way, this peak is bad, but the PNC measurement is not sensitive to this effect.

To detect atoms that have undergone these weak interactions, we empty out a particular hyperfine level, drive the atoms with the weak interaction, and then probe the previously empty level for new population. Thus it is necessary to drive as much of the ground state population to either of the extreme hyperfine and Zeeman sublevels in a process described as optical pumping.

Optical pumping and detection is driven by way of three home built ECDLs tuned to the $6s \rightarrow 6p_{3/2}$ transition. These lasers are the hyperfine, Zeeman, and detection lasers. The three lasers are in Littrow configuration and produce 15 to 20 mW of power. We drive these lasers with homemade current controllers and temperature stabilize them with commercial (Thorlabs Model TED 8020) temperature controllers. The lasers are all frequency stabilized using saturated absorption spectroscopy. Previous heterodyne measurements between our homemade ECDLs by George Toh [22] give $\sim$1 MHz linewidth on a long time scale. This

linewidth is not considered narrow, but it is narrower than the optical transition and is more than sufficient.

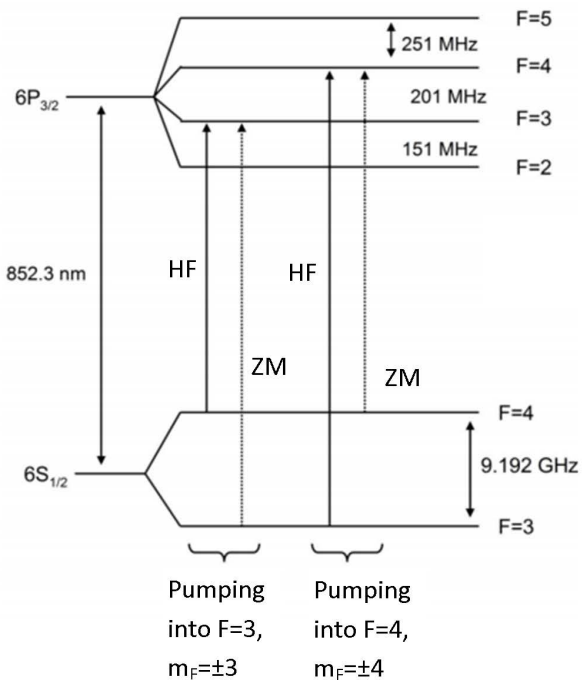

Figure 3.16. Energy level diagram of the ground state and $6p_{3/2}$ excited state in cesium. Optical pump transitions are indicated with arrows. Image from [21]

3.5.1 Hyperfine

The hyperfine laser is used to empty the ground state population out of a particular hyperfine level. Beam geometry, polarization and excited state branching ratios all affect the quality of pumping. We use linear polarization and saturate the transition with a one cm diameter beam that intersects the atomic beam at a right angle. To pump to the $6s$ $F = 3$

hyperfine state, we drive the $6s\ F = 4 \rightarrow 6p_{3/2}\ F = 3$ transition, where the atoms are likely to decay back to the $F = 3$ state (75 %). Few scattered photons are needed on average to populate the $F = 3$ state. To populate the $F = 4$ state, the $6s\ F = 3 \rightarrow 6p_{3/2}\ F = 4$ transition is used. Here the branching ratio is less favorable (58 %), but still depletes the level after a few scattering cycles [20]. To ensure that we drive atoms out of all of the magnetic Zeeman sublevels, we use linearly polarized light that is polarized perpendicular to the applied magnetic field. This linear polarization can be thought of as equal parts right and left circularly polarized light which drive $\Delta m = \pm 1$ transitions. Care is taken to keep the applied magnetic field low such that the edge magnetic Zeeman shifted levels are not pushed out of resonance with the excitation laser.

3.5.2 Zeeman

Along with hyperfine pumping, preparation of magnetic Zeeman sublevels is also necessary. A weak magnetic field is applied to lift the degeneracy of the magnetic sublevels. This shift is small compared to the laser linewidth and broadening due to laser intensity. We drive atoms into extreme magnetic sublevels by driving $\Delta m = +1$ or -1 transitions with left or right circularly polarized light tuned to the $6s\ F = 4 \rightarrow 6p_{3/2}\ F = 4$ ($F = 4$ hyperfine pumping) or $6s\ F = 3 \rightarrow 6p_{3/2}\ F = 3$ ($F = 3$ hyperfine pumping). Circular polarization reversal switches which extreme magnetic sublevel is reached. It is necessary to drive as much of the ground state population to either of the extreme Zeeman sublevels as possible because the weak transition we interfere varies with m and opposite m states have opposite transition amplitudes and would tend to average. This makes relative measurements of weak interactions where only one is dependent on m exceedingly difficult. These measurements require extremely precise determinations of the distribution of atoms in the magnetic sublevels. For instance, the primary source of uncertainty in the two most precise measurements of the ratio of scalar to vector polarizability on the $6s \rightarrow 7s$ transition was the determination in the magnetic sublevel distribution [5, 45].

3.5.3 Detection

Detection of atoms in the previously emptied hyperfine state occurs by way of a detection laser tuned to a cycling transition. This laser is expanded horizontally to 3 cm wide and is directed through the chamber. Below where the atomic beam and detection laser intersect, a large area photodiode collects the scattered light. A curved gold mirror is aligned above this point to direct upward scattered photons downward into the diode. To reduce the background, a 40 nm bandpass filter centered at 852 nm sits atop the photodiode. The output of this photodiode is sent into a transimpedence amplifier with 20 MΩ of transimpedence gain.

To detect atoms in the $6s\ F = 3$ state, we drive a $6s\ F = 3 \rightarrow 6p_{3/2}\ F = 2$ transition and hopefully scatter several photons in a cycling transition. This transition is not a true cycling transition since atoms can evolve into a dark state. To reduce this effect, the detection laser intersects the atom beam with linear polarization, travels through a $\lambda/4$ wave plate, and then is retroreflected. This configuration produces crossed polarization for the returning beam and reduces the likelihood that atoms will evolve into a dark state. This is due to the rapidly varying polarization the atoms see across the atom beam. Along with the varying polarization, a magnetic field gradient helps. Even with these steps to reduce dark states, detection of the $6s\ F = 3$ state is less efficient than detection on the $6s\ F = 4$ state, driven by a $6s\ F = 4 \rightarrow 6p_{3/2}\ F = 5$ cycling transition.

3.6 Raman Lasers

The quality of optical pumping is important in optimizing the interference signal since weak amplitudes often depend on m and oppositely signed m states tend to cancel. Interference measurements comparing weak transitions that do not depend on Zeeman sublevel (α-Stark) to ones that do depend on Zeeman sublevel (β-Stark) require precise determination of average m states. These two constraints require a means of accurately transferring population from individual magnetic Zeeman sublevels on one hyperfine line to the other hyperfine level, where we detect population, without an intermediate step that would introduce population error.

There are multiple techniques with which this transition could be driven, but some have significant downsides which will be mentioned first. The transition could be driven directly with a microwave cavity resonant at the ground state splitting (9192.631 770 MHz). Microwave cavities are bulky, have a finite linewidth, and are difficult to operate in the same location as the optical interaction we wish to study. Since we wish to measure the pumping efficiency at precisely the same location and with the same magnetic field as the interaction we are trying to study, a different technique is required. Another (better) option is to drive this transition optically through a Raman process enhanced by the $6p_{3/2}$ state, detuned from resonance by 1 GHz or less. This can be done by placing sidebands on a laser with an electro-optic phase modulator at half the ground state splitting so that the sidebands are spaced by the ground state splitting. We refrained from this technique since fast fiber-based EOMs are expensive and often have low input powers due to photorefractive effects. Also, it would be difficult to stabilize or even measure the sideband amplitude to the 0.1% level using this technique. A simple and relatively cheap option was to place sidebands directly on a single diode laser through direct current modulation. Initially, this was the technique that our group (and the Boulder group) used [20, 21]. Dionysios Antypas constructed this single Raman laser and drove Raman transitions by frequency modulating the laser diode at half of the ground state splitting to produce upper and lower side bands that are ∼9.2 GHz apart. Then the upper sideband was stabilized ∼160 MHz below the $6s \rightarrow 6p_{3/2}$ transition via an acousto-optic modulator. By tuning the modulation frequency (4.6 GHz), the individual Zeeman split sublevels are driven to the opposite hyperfine level to determine relative populations. This technique was cumbersome and unstable since diode lasers do not like being modulated at such high frequencies. Along with being difficult to stabilize, the sideband amplitude varied by as much as 10 % as a function of modulation frequency [20]. This necessitates a significant correction when determining pumping efficiency. This instability and amplitude variance pushed us towards another option.

A fair amount of time was spent, by Joseph (Jungu) Choi, to recreate this system with three laser sources where two of the sources would be injection locked to ∼4.6 GHz sidebands on a third laser source. By varying the modulation frequency, the sideband would pull the other two bare diode lasers along for frequency offset. This system did not have a large

sideband variance over modulation frequency since the "sidebands" were derived from two laser diodes, but it was quite difficult to use and was unstable.

Due to the complexity and instability of previous systems, I undertook the task of upgrading the Raman lasers to what we use today. With greatly appreciated advice from Cheng-an Chen, I constructed an optical-phase-lock loop utilizing a fast Schottky photodiode (Newfocus 1434)[8], several RF amplifiers and a ADF4007 evaluation board. I constructed a new ECDL and high speed servo[9]. Using this system, I was able to optical-phase-lock two ECDLs that remain stable and modulate the offset frequency between the lasers. Although quiet and phase locked, the degree to which the two ECDLs were phase locked left much to be desired due to a lack of gain. Conveniently, John Hood graciously offered to loan one of his Vescent D2-135 optical-phase-locking servos. Although the homemade servo was likely not too far away from acceptable in terms of performance, the D2-135 was far too nice. It allowed fast modulation, low phase noise, and almost never came unlocked. After having a taste of the finer things, we had to purchase one ourselves. This system was used as is for a while, but we yearned for even lower phase noise. Since one laser is optical-phase-locked to the other, the noise of one laser is written onto the other. With this concept in mind, we purchased a commercial 852 nm ECDL from Moglabs and phase locked the better behaved of the two homemade ECDLs to it. By phase locking the homemade ECDL to the Moglabs ECDL, we narrow the relatively noisy homemade laser down to the linewidth of the Moglabs (60 kHz). The following section will discuss optical-phase-lock loops in more detail.

3.6.1 Optical-phase-locked loops

Optical-phase-locked loops (OPLL) are slightly more complicated phase-locked loops (PLL). Phase-locked loop are common in lock-in amplifiers, radio-frequency synthesizers, spectrum analysers, and other RF electronics[10] that require a high frequency source to be stabilized to a stable, low phase noise oscillator. Using techinques from PLLs, the offset phase of two independent lasers can be stabilized. This is a critical step in driving coherent

[8]↑loaned to us by Carol Tanner
[9]↑design from Cheng-an Chen
[10]↑PLLs are pretty much in everything in a lab

Raman transitions. The offset beat frequency of two lasers is observed on a fast photodiode. The relative phase of this beat signal is compared to a reference and is then stabilized. OPLLs rely on phase detectors to differentiate which source is advanced in phase relative to the other. This knowledge allows a control signal to vary the phase of one of the laser sources to stabilize the phase difference. Phase detection can either be analog (mixer) or digital. A diagram depicting each is included in Fig. 3.17.

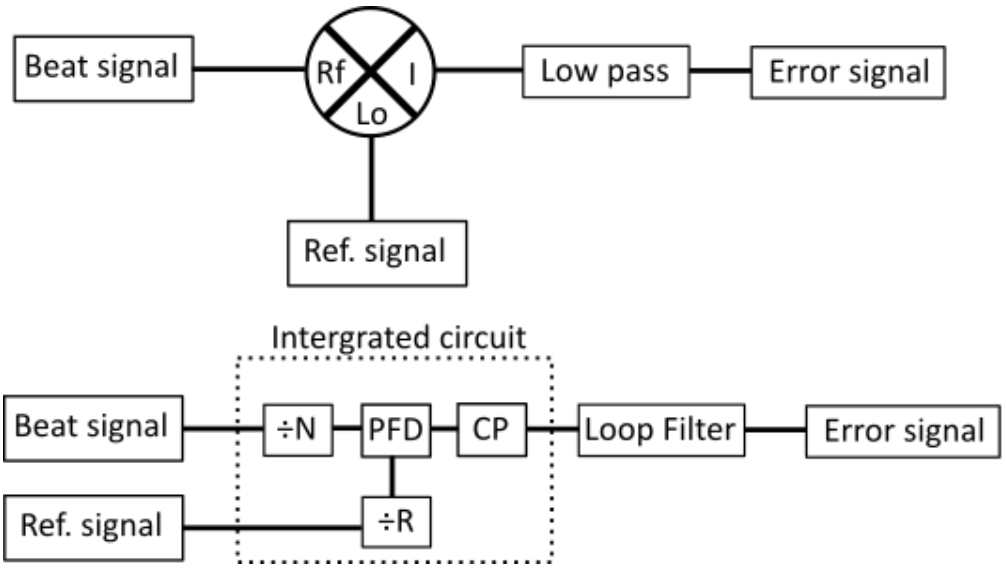

Figure 3.17. Diagram depicting an analog optical-phase-lock loop (top) and a digital phase lock loop (bottom)

Mixers are simple and thus are easy to integrate into a system. They mix (read multiply) the signal down to DC and the DC level indicates the phase. A low pass filter is used to eliminate the local oscillator harmonics and the filter output can be directly fed into a servo. Digital phase locked loops typically utilize frequency dividers, digital phase detectors, and charge pumps. These components are integrated together as a single chip and provide a flexible phase detection system. The D2-135 and the ADF4007 both utilize digital phase detectors. On the PLL integrated circuit, the reference (R) and signal (N) dividers are used to divide the frequency for the phase frequency detector (PFD) to detect the phase. The charge pump (CP) sends out short current pulses whose polarity indicates which phase is ahead (reference or signal). This current pulse is integrated with a loop filter and the output of this loop filter is used as an error signal for phase stabilization. Digital phase detectors

work well with moderate to high signal-to-noise ratios and are monotonic everywhere. This is a convenient feature since large frequency excursions (other than mode hops) are quickly corrected for. On the other hand, the error signal for an analog OPLL is the same when it is locked and when it is not.

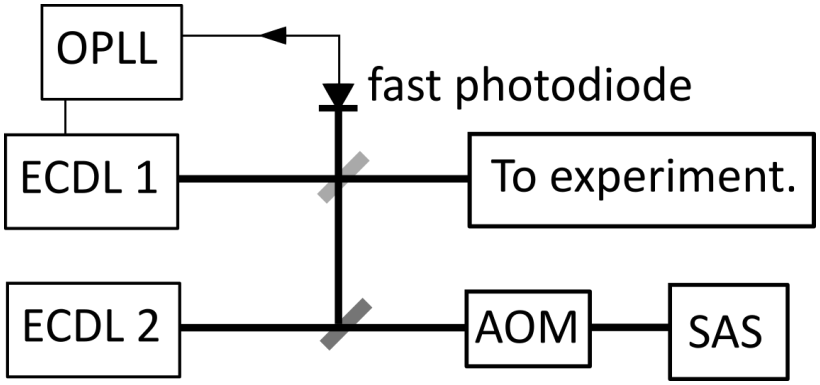

Figure 3.18. Diagram of the Raman laser system

To stabilize the difference between two ECDLs at 852 nm, we beat them on a 26 GHz Schottky photodetector and amplify this beat signal for phase detection. There are commercially available digital phase-lock-loop detectors and servo units to simplify integration. We ultimately chose to purchase a servo from Vescent photonics that includes a digital phase detector. This servo is fast and allows us to phase lock two independent ECDLs 0.25 to 10 GHz apart with a phase error of less that 90 mrad at 9.2 GHz in a 1 MHz bandwidth. An example beat note spectrum is included in Fig. 3.20. Here the servo bumps indicate the loop bandwith is about 1 MHz. It is at this point that the phase of the feedback is 180 degrees out of phase with the error signal and the servo adds to the noise in the system. The servo will begin to oscillate more as the gain increased. With this system we are able to modulate the input reference frequency into the OPLL to vary the offset between the laser and drive the coherent Raman interaction.

So, why do we care about coherence between the two Raman lasers for population detection? We actually don't. It is not necessary for the Raman laser offset frequency to be phase coherent with anything. We only need the lasers to be frequency offset locked. It is, however, critical for the Raman lasers to be phase coherent with the RF cavity in the ground

state experiment. In this experiment, the Raman lasers interact with the cesium atoms and generate a 50:50 mixture of atoms in the ground and excited state. The experimental configuration is illustrated in Fig. 3.19. Then the atoms will be excited with an electric dipole transition facilitated by the weak force interaction within an RF cavity. When the phase of the RF cavity is varied relative to the Raman offset phase, the 50:50 mixture of atoms will oscillate between the ground and excited state. This oscillation will be measured and used to determine the strength of the weak force interaction on this transition. My contribution to the ground state project is the phase coherent Raman field and the technique for modulating the Raman lasers relative to the RF cavity excitation. The technique that we use here, and will use in the PNC measurement, is that we will drive the RF cavity and the Raman lasers at slightly different frequencies. Before, we were using a rotating window to vary the optical path length of a laser to modulate the phase. This technique suffers in the linearity of the scan, the difficulty in setting the scan rate, and the finite length of the scan. By driving the Raman and RF cavity with slightly different frequencies, the phase automatically and infinitely scans at the frequency difference. If we connect all of the 10 MHz clocks, the lock-in-amplifier and the RF generators all agree in frequency. This allows the RF generators to be offset a small amount (≈ 150 Hz and the lock-in amplifier can demodulate at that 150 Hz and output an amplitude that is proportional to the interference. Prior to this technique, we had to scan and dither the phase. This produced a sinusoidal interference signal that then had to be fitted to determine its amplitude. It is much more preferable to not have to fit sinusoids.

3.6.2 Raman spectra

To determine the magnetic sublevel distribution, the two phase-locked lasers are spatially overlapped using an optical fiber and are directed unfocused into the atomic beam. The polarization of these Raman lasers dictate the allowed Δm transition. When we optically pump the atoms into the $6s, F = 3$ $m = \pm 3$ states, we can drive $\Delta m = 0$ transitions since the corresponding m state exists in the $F = 4$ ground state for detection. This is not true for all Zeeman sublevels in the $F = 4$ ground state and a $\Delta m = \pm 2$ transition is necessary.

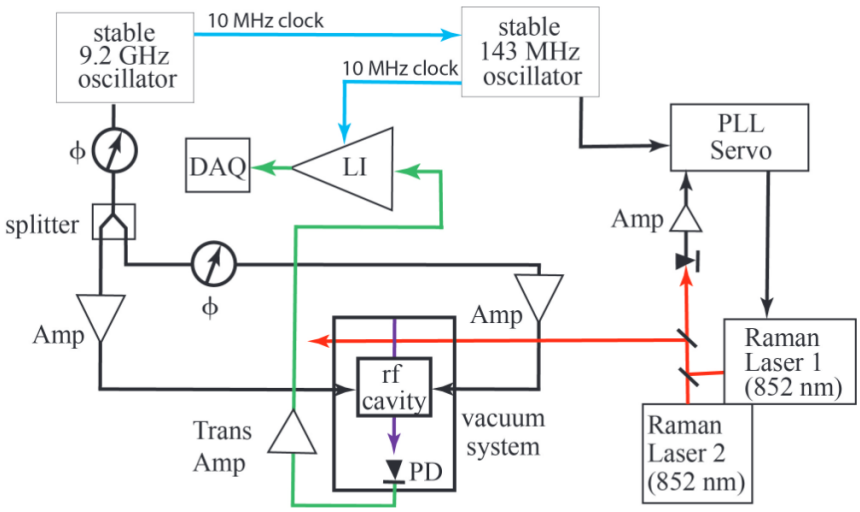

Figure 3.19. Experimental diagram of the ground state experiment. The abbreviations are as follows: DAQ - Data acquisition system, PLL - phase-locked-loop, ϕ - phase shifter, Trans. AMP - transimpedance amplifier, LI - lock-in amplifier, RF - radio frequency.

The $\Delta m = \pm 2$ transitions are more complicated to analyze since the $\Delta m = 0$ are much stronger and tend to still be prominent when trying to only drive $\Delta m = \pm 2$ transitions. For this reason, we have less confidence in the determination of the pumping efficiency when pumping to the $6s, F = 4$ $m = \pm 4$ states.

To drive a $\Delta m = 0$ transition we circularly polarize the Raman lasers with the same handedness while applying a magnetic field in the direction of laser propagation. To collect Raman spectra, we tune the hyperfine laser to empty out a particular hyperfine state and tune the detection laser to the cycling transition exciting that emptied state. By scanning the frequency difference between the Raman lasers, the individual Zeeman shifted magnetic sublevels can be selectively driven in a weak magnetic field. This drives population into the previously emptied hyperfine level where many photons are scattered per atom due to the detection laser. These photons generate a photocurrent that is converted to a voltage signal that is measured by our analog-to-digital converter. An example spectrum without Zeeman pumping is included in Fig. 3.21. In this spectrum, the frequency difference between the Raman lasers is scanned with the offset frequency increasing from left to right. While tuning,

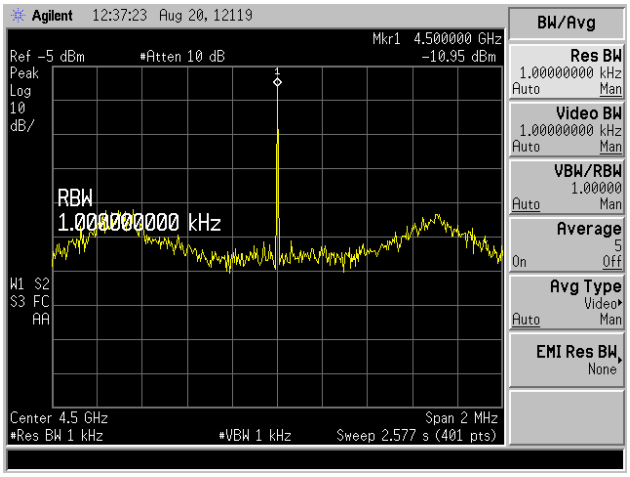

Figure 3.20. Beat note spectrum between the two lasers driving the Raman transitions. The peak in the center here is the beating between the two Raman lasers (divided by two). Here the peak height to noise floor shows a large signal to noise ratio that is indicative of highly coherent laser fields.

the Raman lasers drive $\Delta m = 0$ transitions starting with $6s, F = 3\ m = -3 \rightarrow 6s, F = 4\ m = -3$ (left) and ending with $6s, F = 3\ m = 3 \rightarrow 6s, F = 4\ m = 3$ (right). The spectra are collected by sweeping the frequency difference between the Raman lasers by 64 MHz peak-to-peak around the 9.192 ground state splitting at a rate of 0.5 Hz. Fifteen scans are collected and averaged to reduce noise. Transit time broadening in the Raman beam is the primary broadening mechanism. We operate well below saturation and pressure broadening effects are negligible.

3.6.3 Initial population determination

We use the Raman lasers to probe the individual Zeeman sublevels and look at the relative amplitudes of each transition. To determine the populations, we need to know how strong each transition is. To do this we collect Raman spectra without Zeeman pumping so that one hyperfine level is empty and the opposite hyperfine level is hopefully uniformly populated. Also, we have calculated the line strength of each $\Delta m = 0$ transition and have compared them with the observed value in Fig. 3.21. Each peak is labeled with the percent difference between the observed line strength and the calculated line strength. This comparison relies

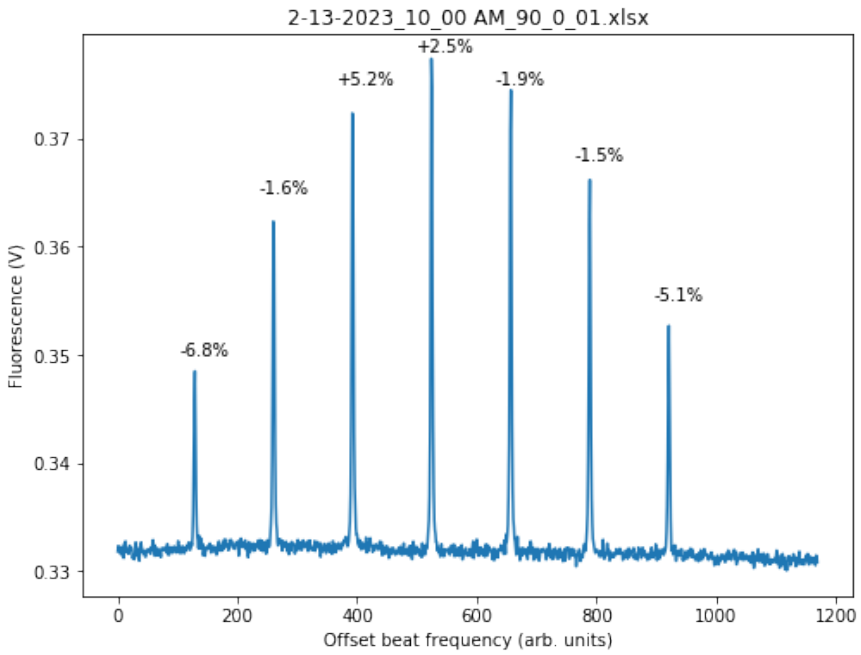

Figure 3.21. Raman spectrum without Zeeman optical pumping.

on the Zeeman levels being evenly populated, but simply having the hyperfine laser emptying one of the hyperfine states affects this initial state population. So, we don't know whether the calculation is right and the hyperfine laser is redistributing the Zeeman sublevels or that the calculation is off and the levels are evenly distributed. To aid in this confusion, we did observe that if the hypefine laser was sent through a good polarizer right before the chamber the calculated line strengths matched better (<7%) than without the polarizer. This is attributed to non-pure polarization of the hyperfine beam causing a weak Zeeman pumping and this indicates that the hyperfine laser does Zeeman pump to a lesser degree. Fortunately, we are not as concerned with the exact populations of each state as we are with the average m value. We can determine the average m value to 0.1 % with a poor knowledge of the line strengths (<7%) if the pumping efficiency is high enough. This decreases the correction for atoms that are not in the correct Zeeman state. To then determine the population, we divide the measured transition amplitudes by their respective calculated line strength.

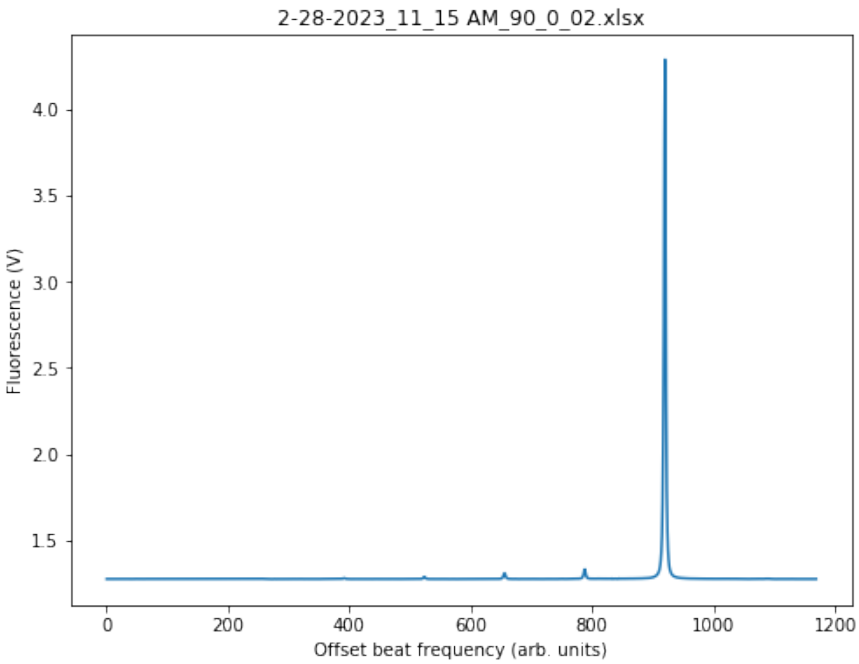

Figure 3.22. Raman spectrum with Zeeman optical pumping into $m = +3$.

3.6.4 Average m

We now know the line strengths for each transition well enough for a 0.1 % measurement of m. If we now allow the Zeeman laser to pump into an extreme Zeeman sublevel, Fig 3.21 turns into Fig. 3.22 when pumping to the $m = +3$ state or into Fig. 3.23 when pumping to the $m = -3$. These spectra are analyzed to determine the peak area for each hyperfine transition. This is done by performing an initial fit to the spectra with a Lorentzian profile, a DC offset and a sloping background. The spacing between each peak and the width of each peak are all forced to be the same. We don't rely on the fit for anything other than determining the peak centers. With the peak centers, we splice individual peaks out of the spectrum and use the edge values to determine the background. Once the background is subtracted, we integrate the peak area to determine the transition amplitude. We divide these amplitudes by their respective transition strengths to determine the relative populations. Then the average value of m can be calculated as;

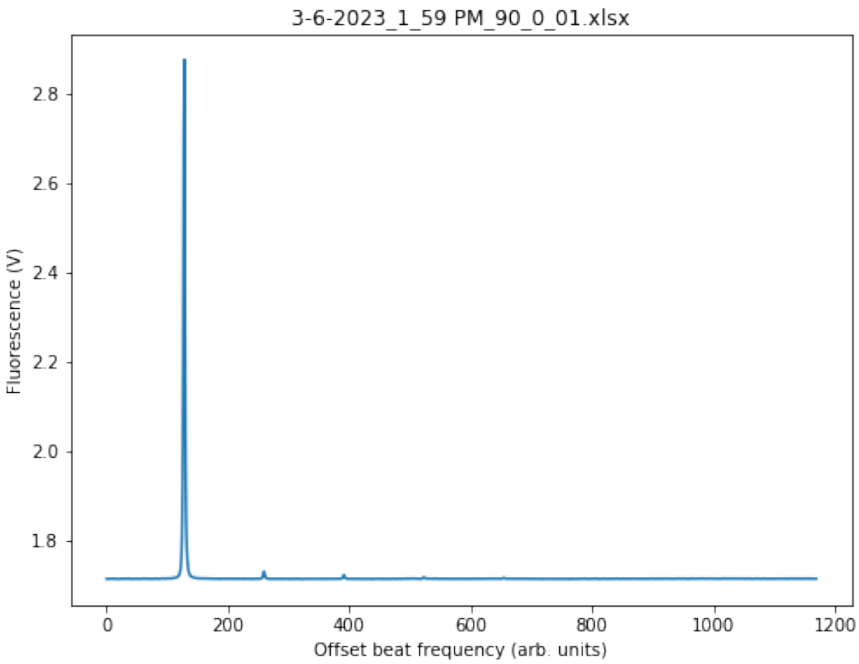

Figure 3.23. Raman spectrum with Zeeman optical pumping into $m = -3$.

$$\langle m \rangle = \sum P_m m \tag{3.3}$$

where P_m is the relative population of that magnetic sublevel and m is the value of that Zeeman sublevel. The value of $\langle m \rangle$ ranges from $-F$ to F for a particular hyperfine level and a larger magnitude of $\langle m \rangle$ indicated more efficient pumping.

3.7 Generation of high power 540 nm light via SHG

To generate narrow band high power at 540 nm, it is easier to start at half the frequency with a low-power quiet seed laser since 540 nm amplifiers aren't available. In general, high power sources are not quiet and quiet sources are not high power. This is typically circumvented by using a master oscillator power amplifier system (MOPA). This technique uses low power quiet lasers to seed high power amplifiers. A MOPA system maintains most of the characteristics of the seed while amplifying up to high powers. We use a 50 mW seed

laser at 1079 nm and amplify up to 10 W in an Azurlight systems fiber amplifier.[11] This amplifier has two gain stages and is described as low phase noise[12]. This high power light is then frequency doubled in a magnesium doped periodically poled lithium niobate crystal (MgO:PPLN or PPLN), see Fig. 3.24.

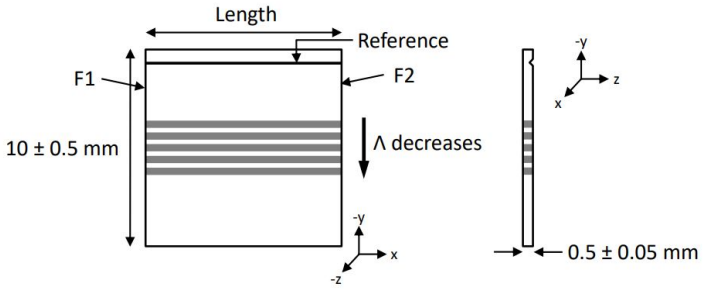

Figure 3.24. Drawing of PPLN crystal. Each channel contains periodic poling. The poling spacing varies to operate across a wider wavelength range. Image from MSHG1064-1.0-20 datasheet.

The periodic poling of the crystal substrate is generated by applying a large alternating electric field to the crystal as it is grown. This periodic structure is necessary for a non-linear process known as quasiphase matching. With an appropriately chosen poling period, extremely high conversion efficiencies can be reached. Bulk PPLN crystals typically come with several poling periods for coarse tuning to the desired wavelength and are typically heated for fine tuning. A tuning chart of the PPLN crystal we use is included in Fig. 3.25 to illustrate this tuning. With 10 W of 1079 nm light focused with a 12.5 cm lens[13], 1150 mW of light at 540 nm is produced.

The 1079 nm laser is amplified and focused tightly into the PPLN crystal. This very intense beam causes local heating in the crystal and may crack it if the crystal is moved quickly or significantly. Alignment into the PPLN crystal should be done at low power and very carefully. Any tweaking at high power should be minuscule if done at all. We have an old damaged PPLN crystal with the smaller 0.5 mm channel width that was cracked while

[11]↑We actually purchased this fiber amplifier shortly after Toptica purchased Azurlight systems (I got quotes from Azurlight and bought from Toptica). So, technically it is a Toptica amplifier.
[12]↑The manufacturer has tested that a 1 kHz seed is not broadened after amplification.
[13]↑Antypas noted in [21] that a tighter focus produces more second harmonic light, but leads to instabilities on the output power likely due to the Green-Induced IR absorption effect (GRIIRA).

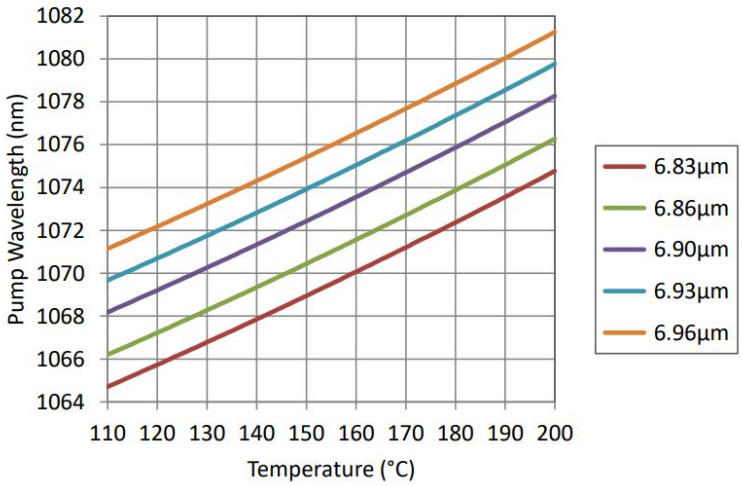

Figure 3.25. Optimal wavelength for second harmonic conversion as a function of temperature for the five PPLN channels. Image from MSHG1064-1.0-20 datasheet.

being used in this manner. We have since switched to the 1 mm channel width, but care must still be taken. To do the alignment, work at low intensities and roughly align the tip-tilt/xyz positioner so that the majority of the 1079 nm beam transmits through the crystal with minimal beam distortion. A small amount of green light should be seen if the crystal has been heated to an appropriate temperature. The chart in Fig. 3.25 is a good place to start when looking for a temperature. The optimal temperature is quite dependent on wavelength, so if you switch from one hyperfine transition to the next, the crystal temperature would need to be tuned for optimal conversion efficiency. Once the beam is aligned and the temperature is set, the power of the laser can be increased and the beam profile should be viewed by picking off a small portion. Here the 1079 nm and 540 nm beam shapes should be checked. The 1079 nm beams comes out of a fiber, so it should have a great beam shape. Since the laser can cause local heating, a small temperature tune down may be necessary at high powers.

3.8 Conclusion

This chapter described the atomic beam apparatus and accompanying lasers that we use to prepare the cesium atoms, excite the transitions of interest, and then detect excited atoms. Then we discussed techniques used to build and stabilize diode lasers to atomic transitions or Fabry-Perot cavities. Finally, the technique for quantifying the atomic spin polarization ($\langle m \rangle$) and the technique for frequency doubling the 1079 nm laser is discussed. We have used these techniques for several measurements which will be discussed through the rest of this dissertation.

4. MEASUREMENTS OF HYPERFINE COUPLING CONSTANTS IN CESIUM

4.1 Introduction

One of the goals of our group is to perform precision measurements to help advance understanding of the weak force interaction. Both the weak Hamiltonian and the hyperfine interaction are sensitive to the electronic wave-function near the nucleus. Ginges and Volotka [46] have proposed a method to calculate lower ns state hyperfine splittings using high precision measurements of higher $ns_{1/2}$ and $np_{1/2}$ states. High precision measurements of these high $ns_{1/2}$ and $np_{1/2}$ levels aid in the understanding of the electronic wave-function near the nucleus and ultimately the relationship between E_{pnc} and the weak charge of the nucleus, Q_w.

This motivation, along with availability of laser sources, led to multiple measurements of hyperfine coupling constants. These hyperfine coupling constant measurements were preformed on the $8p_{1/2}$ and $8p_{3/2}$ states (discussed first) as well as on the $12s$, $13s$, $11d_{3/2}$, and $11d_{5/2}$ states (discussed second). The $J = 1/2$ states are pertinent to the calculations on electronic wave-function near the nucleus and the $J \neq 1/2$ are measured due to their close wavelength to $J = 1/2$ states.

4.2 Theory

The experiment to measure the $8p_{1/2}$ and $8p_{3/2}$ hyperfine coupling constants consists of atomic beam spectroscopy with detection of cascaded fluorescence. The $6s \rightarrow 8p_{1/2}$ transition is illustrated in Fig. 4.1. In Fig. 4.1, the hyperfine structure is depicted for both the excited $8p_{1/2}$ state and for the ground state, $6s$. For the electron angular momentum of $J = 1/2$, two hyperfine states exist with total, nuclear and electron, angular momentum $F = 3$ or 4. The splitting between these F=3 and F=4 states depends on the strength of the magnetic dipole moment of the ^{133}Cs nucleus. For $J = 3/2$, higher order effects such as the electric quadrupole moment of the nucleus also affects the hyperfine spacings. The Hamiltonian that describes these interactions is, [47, 48]

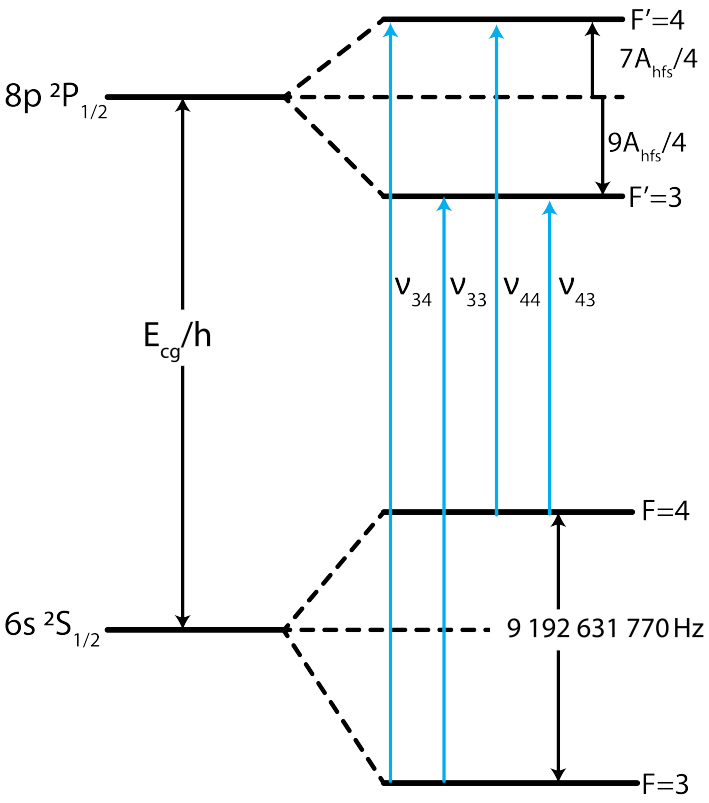

Figure 4.1. Energy level diagram depicting the $6s, F = 3, 4 \rightarrow 8p_{1/2}, F' = 3, 4$ transition.

$$H_{dipole} = AI \cdot J, \quad H_{quadrupole} = B\frac{3(I \cdot J)^2 + \frac{3}{2}I \cdot J - I(I+1)J(J+1)}{2I(2I-1)J(2J-1)} \tag{4.1}$$

where J is the electron's total angular momentum and I is the nucleus' angular momentum. A and B are the magnetic dipole and electric quadruple constants.

The energy shift due to the hyperfine interaction is,

$$\Delta E_{hfs} = \frac{1}{2}AK + B\frac{\frac{3}{2}K(K+1) - 2I(I+1)J(J+1)}{2I(2I-1)J(2J-1)} \tag{4.2}$$

where,

$$K = F(F+1) - I(I+1) - J(J+1) \tag{4.3}$$

.

For the $8p_{1/2}$ state, the energy splitting between $8p_{1/2},\ F' = 3$ and $8p_{1/2},\ F' = 4$ is $\Delta E_{hfs} = 4A$ The $8p_{3/2}$ state contains four lines due to the four possible values for the total angular momenta, F'. The $8p_{3/2}$ state is illustrated in Fig. 4.2. The individual energy spacings for the $8p_{3/2},\ F' = 2, 3, 4, 5$ states are more complicated than that of the $8p_{1/2}$ due to the inclusion of the electric quadrupole effect and are calculated using equation 4.2.

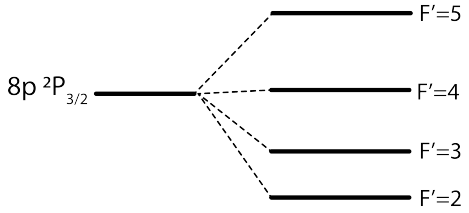

Figure 4.2. Energy level diagram depicting the $8p_{3/2}, F' = 2, 3, 4, 5$ states.

The limiting factor in the uncertainty of these measurements was the linewidth of the individual transitions. Broader lines are more difficult to determine the center of and lines can be less resolvable if they are close enough together. For the $8p_{1/2}$ and $8p_{3/2}$ experiments, the transition linewidth was most affected by the divergence of the atomic beam. The atomic beam is generated in a vacuum chamber and the driving laser beam intersects the atomic beam at a right angle to reduce the Doppler broadening. The atoms are housed in a heated oven and are effused through narrow capillaries. After the capillaries, the atomic beam is further collimated by parallel glass microscope coverslips that are spaced by glass microscope slides. The geometry of the nozzle assembly and the cover slip collimator define the divergence of the atomic beam and directly impact the observed linewidth. Residual Doppler broadening due to the unwanted divergence of the atomic beam is approximately [43],

$$\Delta\omega = \mathbf{k} \cdot \mathbf{v}. \tag{4.4}$$

Here $\mathbf{k}$ is the wave vector of the laser beam and $\mathbf{v}$ is the velocity of the atomic beam. With a 40 mrad divergence estimated from the geometry of the collimator, the observed linewidth

of 26 to 27 MHz is in excellent agreement with the estimate of broadening due to the nozzle geometry, 27.7 MHz width for $\langle v \rangle$ =270 m/s Cs beam where $\langle v \rangle$ is the average atomic velocity. Other smaller broadening mechanisms include the laser linewidth, transit-time broadening, collisional broadening, Zeeman broadening, and Stark broadening. Transit time broadening occurs due to the finite time of the interaction between the fast atomic beam through the narrow laser beam. In this experimental geometry, the transit-time broadening is estimated to be less than 20 kHz. Collisional broadening occurs when atoms collide with one another. We operate in a vacuum of 5×10^{-6} Torr and with a fairly well collimated atomic beam. Collisions are quite infrequent and do not significantly contribute to the linewidth of the transition. We mitigate the broadening and line shifts due to the Stark effect by operating much lower than the saturating power of the transition and by varying the laser power to extrapolate back to zero power. Finally, the Zeeman shifts and broadening are studied and determined to be negligible when biasing magnetic fields are used to cancel out external fields.

A critical component for these hyperfine coupling constant measurements is the frequency comb laser source we share with Prof. Wiener's group, see Fig. 4.3. This laser source is a mode locked erbium doped femtosecond fiber laser. Many coherent modes of light are oscillating inside of the laser resonator. This produces an ultrashort pulse of light that is emitted with a repetition rate of approximately 250 MHz. In the frequency domain, this pulse train represents many different optical frequencies that are spaced by the repetition rate. This signal looks much like an upturned comb hence the name, frequency comb laser. When the repetition rate and offset frequency of the mode locked laser are stabilized, the comb of light that it produces becomes a valuable tool for spectroscopy, optical clocks, and many other areas of study.

Along with fluorescence, we measure the absolute frequency of the driving laser to resolve the line center of each transition. We measure this frequency by beating our laser against the previously discussed frequency comb laser source. The frequency comb's center wavelength is 1560 nm. This output is frequency doubled to 780 nm and then spectrally broadened through four-wave mixing in a highly nonlinear photonic crystal fiber. Prior to spectral broadening, the comb width is a few tens of nanometers. After broadening, the comb spans

over an octave, 500 to 1050 nm. The comb is self-referenced and is stabilized to a low phase noise GPS conditioned reference. The repetition rate is $\nu_{rep} = 250$ MHz and the offset is $\nu_{offset} = 40$ MHz. The absolute frequency of an individual comb line is,

$$\nu = N\nu_{rep} + \nu_{offset} \tag{4.5}$$

and the absolute frequency of a laser beat against the comb is,

$$\nu_{laser} = N\nu_{rep} + \nu_{offset} \pm \nu_{beat}. \tag{4.6}$$

The $\pm\nu_{beat}$ accounts for beating from above or below the nearest comb tooth. By measuring the frequency of our laser to better than half the repetition rate with a wavemeter, we determine the comb tooth number, N. The sign of the beat frequency can be determined by viewing the beat note as the laser frequency is tuned higher or lower on a spectrum analyzer. For instance if the laser frequency and beat note are both increasing, then the laser is above and moving away from the nearest tooth. The comb tooth number (N) can also be determined by varying the repetition rate of the comb and observing how much the beat note changes. This technique was not preferable since it requires someone to run back and forth between labs several times. With the comb tooth number, repetition rate, offset frequency, and beat frequency, the absolute frequency of the beating laser can be determined.

The experiments to measure the hyperfine coupling constants of the 8p, 12s, 13s, and 11d states comprised of measuring the absolute frequency of the driving laser while detecting fluorescence from the excited atoms in either a vapor cell or in an atomic beam. Fluorescence versus frequency spectra are recorded and fit with appropriate lineshapes to determine the center frequency of each line.

4.3 8p hyperfine measurements

The hyperfine coupling constant measurements were completed and reported separately. The $12s_{1/2}$, $13s_{1/2}$, and $11d_{3/2,5/2}$ measurements were completed first in a vapor cell and

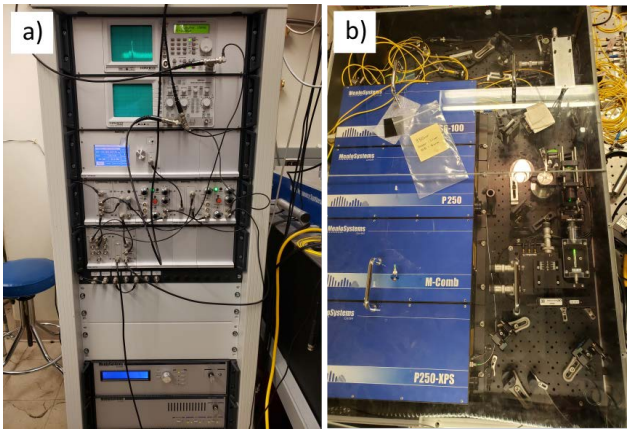

Figure 4.3. a) Frquency comb laser source control electronics b) Frequency comb laser source

then the $8p_{1/2}$ and $8p_{3/2}$ were completed later in an atomic beam. The $12s_{1/2}$, $13s_{1/2}$, and $11d_{3/2,5/4}$ measurements were completed in a vapor cell since the two-photon transition is much weaker and the signal was Doppler-free using retro reflected beams. The $8p_{1/2}$ and $8p_{3/2}$ measurements were driven with a single photon and in this case an atomic beam is preferable since an atomic beam produces less broadening.

The experimental configuration for the $8p_{1/2}$ and $8p_{3/2}$ hyperfine coupling constant measurements are as follows, see Fig 4.4. 3.5 W of 778 nm light is generated in a commercial ECDL and tapered amplifer unit and is focused into a lithium tri-borate crystal (LBO) in a single pass configuration to generate second harmonic light at 388 to 389 nm (170 μW) to excite the electric dipole transition. This doubled light is chopped and directed into a vacuum chamber, through an atomic beam and is retro-reflected to reduce Doppler shifts. The cascaded fluorescence is detected from primarily the $6p_{1/2}$ and $6p_{3/2}$ excited states using a silicon photo detector filtered with a 700 nm long pass filter to reduce scattered light. The fluorescence is amplified in a homemade transimpedence amplifier with 50 MOhm of transimpedence gain. This amplified signal is then demodulated in a lock-in amplifier at the chopped frequency. The output of the lock-in amplifer is digitized in an analog to digital converter. Concurrently, a portion of the 778 nm light is beat against the frequency

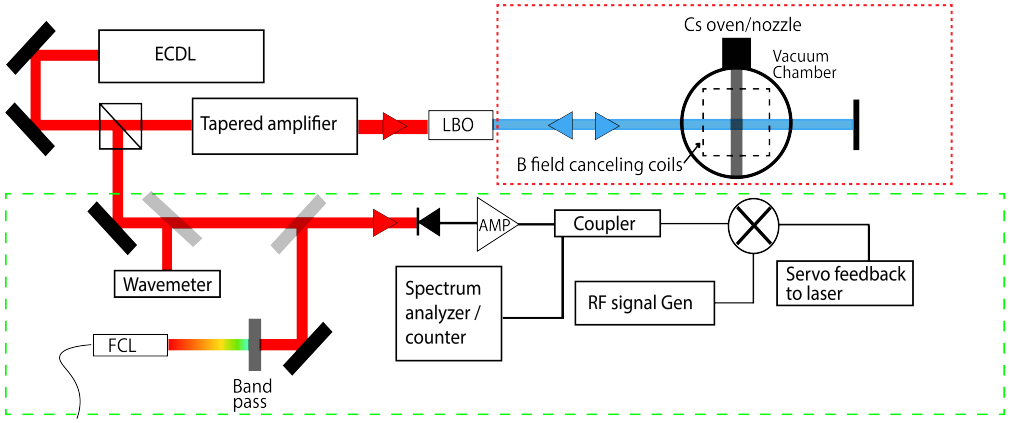

Figure 4.4. Experimental configuration for the $8p_{1/2}$ and $8p_{3/2}$ hyperfine spectroscopy. The lithium tri-borate crystal used for frequency doubling is labeled LBO. The fine red dotted section includes the fluorescence detection and magnetic field canceling coils. The coarse green dotted section illustrates the frequency measurement and stabilization.

comb laser (FCL) and another portion is measured with a wavemeter. The combination of these measurements yields precise absolute frequency measurements limited by the observed linewidth of the transition. The center frequency of the atomic resonance is fit and has an uncertainty in range of 12-28 kHz. We sweep the laser by utilizing an analog optical phase lock loop to stabilize the fundamental laser offset from the nearest comb tooth. The offset frequency driving the OPLL is varied to sweep the laser across the desired transition. Offset phase locking the ECDL to the frequency comb imposes the inherent stability of the comb onto the laser and can significantly reduce the linewidth of the ECDL[1]. In this configuration, the laser linewidth does not significantly increase the linewidth of the transition.

We collect data in the following manner. After the temperature of the oven and nozzle have adequately stabilized to produce a consistent atomic beam density, the signal generator frequency is set to control the offset beatnote. The system pauses for a time 2τ, where $\tau = 100$ ms is the time constant of the lock-in amplifier. One hundred voltage samples are then collected using a 16-bit analog-to-digital converter (ADC) at a rate of one kHz, and

[1]↑The shared comb has approximately 65 kHz of linewidth near the fundamental comb frequency. This linewidth can be viewed on the CEO beat monitor.

are averaged and recorded. Ten sets of 100 voltage samples are collected. This protocol reduces correlation among the ten different data sets. The average and standard error of the ten voltage sets are then computed and recorded. The frequency of the signal generator is measured with a frequency counter and the beat signal itself is measured with a spectrum anaylzer. Both of these frequencies are recorded. Then the signal generator is advanced to the next frequency. We collect a spectrum by stepping up and then back down through the optical transition and carefully search for drifts in the atomic beam density. A scan across the spectrum in both directions takes between four and six minutes, depending on the frequency width of the scan. We collect 15 to 20 spectra for each transition and fit the entire scan (both up and down-scans together). With these 15 to 20 individual fits, we determine the mean center frequency for each transition.

We separately measure and record the absorption spectrum of each of the hyperfine components $6s, F \rightarrow 8p_{1/2}, F'$, where $F = 3, 4$ ($F' = 3, 4$) is the total angular momentum of the ground $6s$ (excited $8p_{1/2}$) state. We show a single spectrum of the $6s, F = 3 \rightarrow 8p_{1/2}, F' = 3$ line, as a representative sample, in Fig. 4.5a. The hyperfine lines for the $6s, F = 3(4) \rightarrow 8p_{3/2},\ F' = 2, 3, 4(3, 4, 5)$ transitions are plotted in Fig. 4.5b(4.5c).

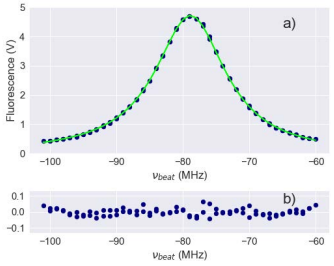

(a) Hyperfine spectrum for the $6s,\ F = 3 \rightarrow 8p_{1/2},\ F' = 3$ transition.

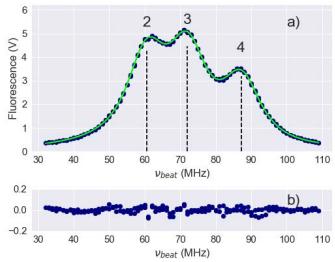

(b) Hyperfine spectrum excited from the $6s,\ F = 3$ ground state $\rightarrow 8p_{3/2},\ F' = 2, 3, 4$.

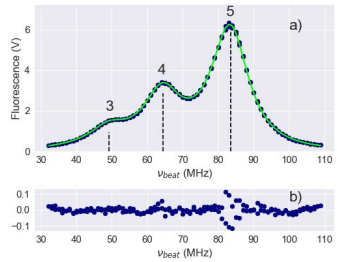

(c) Hyperfine spectrum excited from the $6s,\ F = 4$ ground state $\rightarrow 8p_{3/2},\ F' = 3, 4, 5$.

Figure 4.5. Three representative hyperfine spectra for the $8p_{1/2}$ and $8p_{3/2}$ states. Each figure contains the measured fluorescence spectra and fit (above) and the associated residuals (below).

The spectrum shows the fluorescence signal (lock-in amplifier output) versus the measured beat frequency between the fundamental (778 nm) laser and the nearest comb tooth of

the frequency comb laser. The spectra are fit to a Voigt profile using a least-squares fitting algorithm. The fitting parameters include the amplitude, Gaussian and Lorentzian width, and center frequency of the peak, and a sloping baseline. The gently ($< 1\%$ change) sloping baseline is produced by scattered light, and is present even in the absence of the atomic beam.

The spectra here illustrates the fluorescence detected from the electric dipole transition excited by the second harmonic generated light versus the beat frequency between the comb and the fundamental laser frequency. Since we drive the transition with the second harmonic light and measure the laser frequency with the fundamental light, a frequency change in the fundamental light results in twice the change in the second harmonic. Due to this, the atomic linewidth is twice the plotted linewidth in Fig. 4.5. As stated above, the linewidth is in excellent agreement with estimated atomic beam divergence. Other broadening mechanisms are negligible and the natural linewidth is much narrower than the observed transition, 0.42 MHz for $8p_{1/2}$ and 0.5 MHz for $8p_{3/2}$. These linewidths are calculated from [49]. The residuals are shown in the lower plots of Fig. 4.5. This rms value of the residual is $\sim$0.5% of the peak signal level, and is primarily due to thermal noise in the feedback resistor of the transimpedence amplifier. This Johnson$-$Nyquist noise scales as the square root of the resistance. Reducing the transimpedance amplifier resistance would reduce the noise, but also decrease the signal-to-noise ratio. The only modification to approach the shot noise limit would be to increase the fluorescence signal itself.

To account for ac Stark shifts in our measurement, we measure each transition at multiple different laser intensities. With these measurements, we extrapolate the center frequency back to zero laser power for each line. We measure the hyperfine splitting of the $8p_{1/2}$ state while driving transitions from either the $6s$ $F = 4$ or $6s$ $F = 3$ hyperfine ground states. The two values are 42.936(9) MHz and 42.926(15) MHz, respectively. A weighted average of these two is computed and reported in Table 4.1. The uncertainty in this measurement is largely dominated by the line center fitting due to the width of the transition, 12 to 28 kHz. We also include the error due to the frequency comb uncertainty (<0.5 kHz), and the Zeeman effect (<0.2 kHz). These errors are added in quadrature and are reported as the total uncertainty in the determination of the line center frequencies in Table 4.2. We also

report previous measurements and theoretical calculations of A. Our value agrees well with previous measurements, but with significantly reduced uncertainty, and with calculations by [50] in Table 4.1. Other theoretical calculations appear to differ, but do not report an error.

Table 4.1. Summary of results for the hyperfine coupling constant A, in MHz, of the $8p_{1/2}$ level. The numbers in parentheses following each value are the 1σ standard error of the mean in the least significant digits.

A MHz	Source
Experiment	
42.97 (10)	Tai *et al.*, 1973 [51]
42.92 (25)	Cataliotti *et al.*, 1996 [52]
42.95 (25)	Liu & Baird, 2000 [53]
42.933 (8)	This work
Theory	
42.43	Safronova *et al.*, 1999 [54]
42.32	Tang *et al.*, 2019 [55]
42 (1)	Sahoo *et al.*, 2021 [56]
42.95 (9)	fit method, Grunefeld *et al.*, 2019 [50]
42.93 (7)	ratio method, Grunefeld *et al.*, 2019 [50]

Table 4.2. Sources of error and the uncertainty resulting from each, for the determinations of line centers for each of the spectra. We add the errors in quadrature to obtain the total uncertainty. *Beam misalignment affects only the absolute frequency determinations.

Source	σ_{int}(kHz)
Fit, σ_ν	12-28
FCL frequency, ν_{FLC}	< 0.5
Zeeman	< 0.2
Beam misalignment*	150
Total Uncertainty, $\sigma_{\text{int}}^{\text{total}}$	12-28

The hyperfine splittings of the $8p_{3/2}$ state are also measured. This measurement is quite similar to the $8p_{1/2}$ state, but differ in a few notable ways. The first of which is that three individual lines are driven from each ground state since we drive $\Delta F = 0$ or ± 1 transitions.

This allows us to fit multiple peaks in a single scan. Another difference is that the lines are close to one another and are not completely resolved. This increases the uncertainty in the fitted center frequency compared to the $8p_{1/2}$ spectra. The last important difference is that the transition amplitude is larger by a factor of 5 to 10. This allows us to have better signal-to-noise ratios for the low laser power spectra. Other than these differences, the data collection and analysis is the same as the $8p_{1/2}$.

We observed no change to the hyperfine spacings of the $8p_{3/2}$ state when applying a one Gauss magnetic field and power dependence spectra show a slight laser power dependence (200 to 450 Hz/μW). With these hyperfine spacings, we calculate the hyperfine coupling constants and report them in Table 4.3.

In this work, we report a new, high precision measurement of the hyperfine coupling constant A =42.933(8) MHz for the $8p_{1/2}$ state in atomic cesium-133. This determination is supplemental to theoretical efforts toward high precision calculations of electronic wave functions. These wave functions are critical in determining the dependence of E_{PNC} on the weak charge, Q_w. We were generously loaned the atomic beam apparatus and critical equipment by one of our collaborators, Dr. Carol Tanner, that is similar to the beam apparatus used in her group's high precision studies of hyperfine coupling constants [47, 57, 58]. With this vacuum chamber, we were able to quickly generate an atomic beam necessary for this experiment. The measurement of the hyperfine coupling constants for the $8p_{1/2}$ and $8p_{3/2}$ levels has been published in Physical Review A [59].

Table 4.3. Summary of results for the hyperfine coupling constants A, B, and C, in MHz, of the $8p_{3/2}$ level. The numbers in parentheses following each value are the 1σ standard error of the mean in the least significant digits.

A MHz	B MHz	C MHz	Source
Experiment			
7.626 (5)	-0.049 (42)	-	Bucka *et al.*, 1962 [60]
7.58 (1)	-0.14 (5)	-	Faist *et al.*, 1964 [61]
7.626 (5)	-0.090 (24)	-	Rydberg *et al.*, 1972 [62]
7.644 (25)	-	-	Abele *et al.*, 1975 [63]
7.42 (6)	0.14 (29)	-	Bayram *et al.*, 2014 [64]
7.609 (8)	-0.005 (40)	0.016(4)	This work, 2022
Theory			
7.58 (5)	-0.046 (35)	-	Barbey *et al.*, 1962 [65]
7.27	-	-	Safronova *et al.*, 1999 [54]
7.44	-	-	Tang *et al.*, 2019 [55]

4.4 12s, 13s, and 11d hyperfine measurements

To aid in electronic structure calculations, we also measured the hyperfine splittings of two higher $ns_{1/2}$ states, $n = 12$ and 13. The two-photon transition relies on coupling between opposite parity states to facilitate the transition and is much weaker than the electric dipole transition driving the $6s \rightarrow 8p$ transitions. Due to this much weaker signal, we excite the transition in a heated vapor cell and collect fluorescence with a photomultiplier tube (PMT, type R928). The PMT has a much higher sensitivity (3.5×10^4 A/W) than the photodetector described above and the heated vapor cell produces a much denser cesium cloud than an atomic beam. These two methods for increasing the signal are not without consequence. The collisional broadening in the vapor cell, which is negligible in a atomic beam, becomes significant and must be accounted for. We reduce systematic effects of collisional broadening by measuring the center frequencies as a function of collision rate, controlled by vapor cell temperature, and extrapolate back to zero collision rate. In this measurement, we drive a two-photon transition with an amplified ECDL in a MOPA configuration. Since the two

photons were of equal frequency (from the same laser source), we excite only $\Delta F = 0$ transitions. Laser frequency determination is identical to the $8p$ measurements, but the frequency stabilization technique differs. This is due to the decreased optical power at the two-photon wavelength in the frequency comb output. The photonic crystal fiber responsible for the spectral broadening via four-wave mixing is optimized for green light and not red (670 nm). The amount of frequency comb power at 670 nm is about 30 dB lower than the power near the center frequency (where the ECDL was phase locked for the $8p$ measurements).

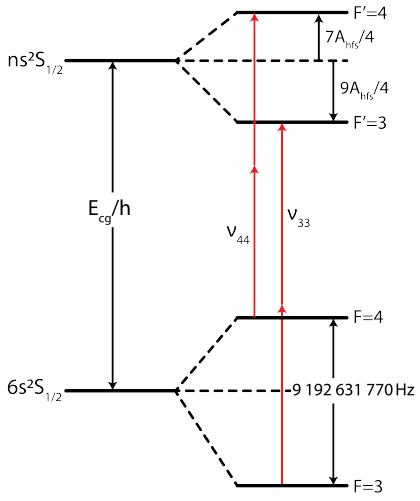

Figure 4.6. Energy level diagram showing the hyperfine components (not to scale) of the $6s$ and ns states of cesium, where $n = 12$ or 13. ν_{33} (ν_{44}) indicates the frequency of the laser when resonant with the $F = 3 \rightarrow F' = 3$ ($F = 4 \rightarrow F' = 4$) two-photon transition. $E_{\rm cg}$ is the energy of the $12s$ or $13s$ state in the absence of the hyperfine interaction (that is, the center-of-gravity of the state).

The experimental setup is as follows and is illustrated in Fig. 4.8. The commercial diode laser (ECDL) and tapered amplifier generate 180-300 mW of narrow-band cw light, which is focused into a heated cesium vapor cell. After passing through the cell, the laser light is reflected back on itself for Doppler-free two photon excitation. We collect the fluorescence light (green box) emitted from the final $6p_{3/2} \rightarrow 6s$ step of the decay, which we measure with a photomultiplier tube (PMT). We use a Faraday isolator to separate the retro-reflected beam from the input beam, while maintaining the linear polarization of the excitation beam in the vapor cell. We stabilize the laser frequency (blue box), offset with a broadband electro-

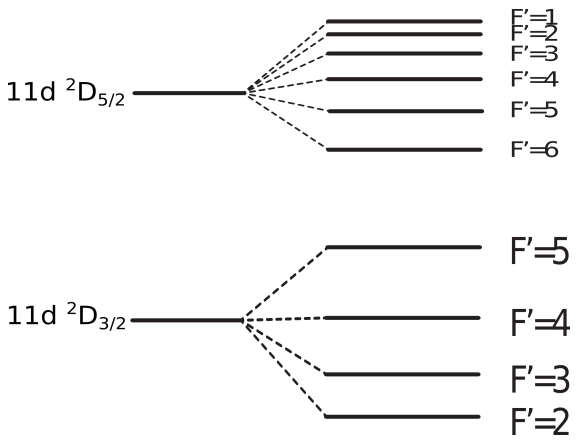

Figure 4.7. Energy level diagram showing the hyperfine components of the $11d_{3/2}$ and $11d_{5/2}$ states in cesium. Not shown here is the ground state from which we excite the cesium atoms. Note that the $11d_{5/2}$ state is inverted, with the level energy decreasing with increasing F'. The energy spacings of the $11d_{3/2}$ state are not drawn to scale with the energy spacings of the $11d_{5/2}$ state, nor is the fine structure interval between the $11d_{3/2}$ and $11d_{5/2}$ states to scale.

optic modulator (EOM), to the transmission peak of a temperature-stabilized etalon. We measure the frequency (red box) of the beat note between the laser light and a single tooth of a frequency-comb laser (FCL) for absolute calibration of the laser frequency.

To measure the transition amplitude as a function of laser frequency, we very slowly ramp the laser frequency by tuning the EOM driving frequency. The frequency is swept back and forth several times to eliminate shifts in the center frequency. Since the sideband of the laser is stabilized to the etalon, the carrier signal sweeps with the driving frequency. We do not rely on the etalon for frequency measurement (only for short term frequency stability), slight shifts in the etalon frequency over the course of a scan do not affect the fitted center frequency. Unmodulated laser light is beat against the nearest tooth of the frequency comb source. This beat frequency is recorded continuously during the scan. The fluorescence from the $6p_{3/2} \rightarrow 6s$ decay is imaged by a lens onto the photomultiplier tube photocathode. This signal is amplified in the PMT and then digitized using a 16-bit analog-to-digital converter. We collect 6 to 9 spectra similar to the one shown in Fig. 4.9 for each hyperfine line and fit

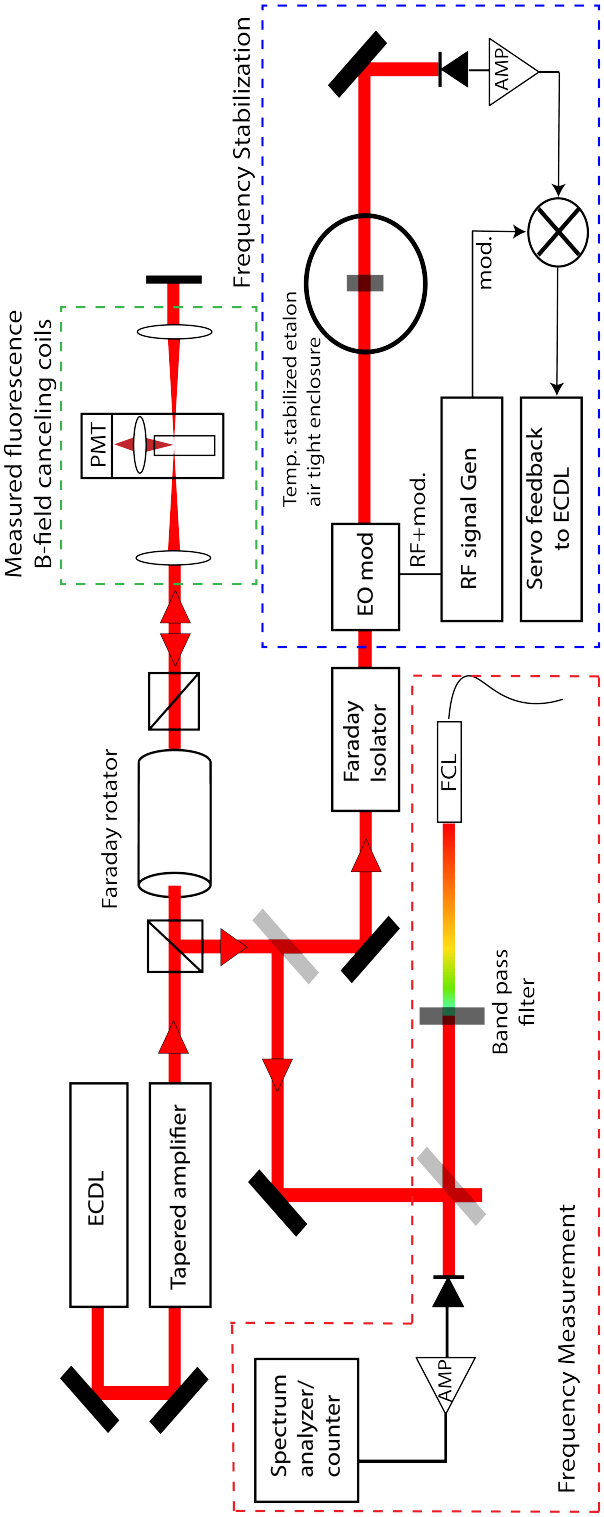

Figure 4.8. Experimental setup for the measurement of the two-photon absorption spectra.

the center frequencies using a Lorentzian function. From these fitted center frequencies, we calculate the mean and standard error.

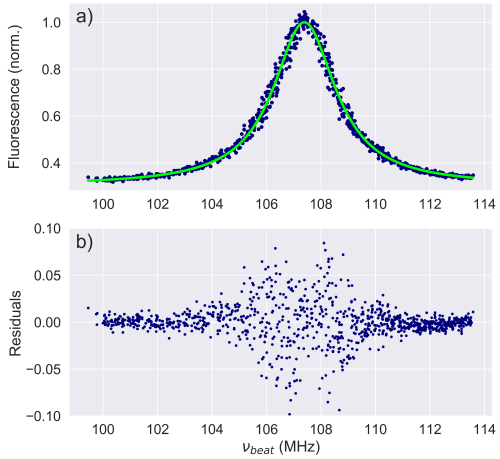

Figure 4.9. (a) An example of a two-photon spectrum of a single hyperfine line, consisting of the normalized fluorescence signal versus the beat frequency ν_{beat}. These data represent the $6s, F = 4 \rightarrow 13s, F' = 4$ line. Each data point is the signal collected in a 100 ms window as the laser frequency is scanned continuously over the 14 MHz span. The solid green line is the result of a least-squares fit of a Lorentzian function to the data. (b) The residuals of the fitted function.

To test for effects of collisional broadening, ac Stark shift, and possible Zeeman shifts, we measure the linecenter frequencies at various vapor cell temperatures, laser powers, and applied magnetic fields. Under a one Gauss applied field, there are no observable Zeeman shifts within the resolution of our measurement. We reduce the magnetic field around the vapor cell to a level below 10 mGauss by applying a weak magnetic field using three pairs of magnetic field coils. This helps reduce the effect of Earth's magnetic field and stray fields originating from the optical table. Collisional broadening and ac Stark shifts both affect the linewidth of the transition as well as linecenter frequency. We record linecenter frequencies in a grid of various vapor pressures and laser powers. We then fit this surface with a plane and use the zero laser power and vapor pressure intercept to determine the linecenter frequencies. This process was repeated on the opposite hyperfine level of the ground state to excite the opposite ns hyperfine state (Note only $\Delta F = 0$ transitions are allowed). From these frequencies and the defined ground state splitting, the hyperfine spacing

for the $12s$ and $13s$ states are calculated. The resultant hyperfine coupling constants, A, are reported in Table ??. These values are in excellent agreement with theoretical calculations [50, 55] and previous experimental results [66, 67]. Using the fitted center frequencies and the comb tooth number, the absolute frequency is calculated and reported in Table ??. These linecenter frequencies agree with and are more precise that previous measurements [24].

Table 4.4. Summary of results for the hyperfine coupling constants $A_{\rm hfs}$ of the $12s$, $13s$, $11d_{3/2}$ and $11d_{5/2}$ states of ^{133}Cs. The numbers in parentheses following each value are the 1σ standard error of the mean in the least significant digits. The techniques employed in Refs. [68] and [69] yielded the magnitude of $A_{\rm hfs}$, but not its sign. Therefore, we have listed these results preceded by the '$\pm$' sign.

State	$A_{\rm hfs}$ (MHz)			
	Experiment		Theory	
	This work	Prior exp.	Ref. [55]	Ref. [50]
$12s$	26.318 (15)	26.31 (10) [66]	26.28	26.30 (2)
$13s$	18.431 (10)	18.40 (11) [67]	–	18.42 (1)
$11d_{3/2}$	+1.0530 (69)	$\pm$1.055 (15) [68] $\pm$1.05 (4) [69]	1.06	–
$11d_{5/2}$	−0.21 (6)	$\pm$0.24 (6) [68]	−0.142	–

Due to the proximity of the $11d_{3/2}$ and $11d_{5/2}$ lines to the $12s$ and $13s$ lines, we decided to measure the hyperfine coupling constants as well as the absolute frequency of these lines. These lines differ in that we can scan across most of the hyperfine lines in a single scan. These lines are difficult to resolve in our experimental configuration and the accuracy of the hyperfine coupling constant determination is reduced. Nevertheless, we measured the hyperfine coupling constants in a similar manner as the $12s$ and $13s$ states except that we fit multiple peaks in a single scan. We correct for power and collisional broadening as before and report coupling constants in Table ?? and absolute frequencies in Table ??.

This work, published in PRA [70], reports new high precision values for the hyperfine coupling constants for the $12s$ and $13s$ states in atomic cesium. This work is in support of theoretical calculations of the electronic wave function that has implications on the relationship between the parity nonconserving moment and the weak charge of the nucleus. This

Table 4.5. Summary of results for the state energies $E_{\rm cg}/h$ of the $12s$, $13s$, $11d_{3/2}$, and $11d_{5/2}$ states of ^{133}Cs. The numbers in parentheses following each value are the 1σ standard error of the mean in the least significant digits.

Line	E_{cg}/h (MHz)	
	this work	Prior exp. [24]
$6s \rightarrow 12s$	889 448 351.098 (29)	889 448 348.5 (60)
$6s \rightarrow 13s$	900 450 284.724 (20)	900 450 282.0 (60)
$6s \rightarrow 11d_{3/2}$	896 269 630.698 (65)	896 269 624.7 (60)
$6s \rightarrow 11d_{5/2}$	896 365 856.56 (24)	896 365 852.6 (60)

work also includes high precision determinations of the linecenter frequencies of the $12s$, $13s$, $11d_{3/2}$, and $11d_{5/2}$ states.

5. STATIC STARK SHIFT OF THE $7s\,^2S_{1/2}$ LEVEL IN ATOMIC CESIUM

5.1 Motivation

In this chapter, we will discuss the measurement of the static Stark shift of the $7s\,^2S_{1/2}$ level. The 2019 letter by Toh *et al.* [71] pointed out a discrepancy, 2.8 σ, between values of the Stark vector polarizability when using a sum-over-states approach to determine α combined with the measured α/β ratio and a calculated value of M_1^{hf} combined with a measured value of M_1^{hf}/β. Contention between the two techniques used to evaluate the Stark vector polarizability casts doubt on each technique's precision. An accurate value for the Stark vector polarizability is critical in determining the value for Q_w. Any of these four quantities (α, α/β, M_1^{hf}, and M_1^{hf}/β) could be errant. Since atomic theorists are pretty confident in the calculated value of M_1^{hf} to the 0.1% level [72], we turned our attention towards a ratio measurement of α/β and the static Stark shift measurement. We are also interested in measuring the M_1^{hf}/β ratio, but that is another thesis.

Recent high precision theoretical calculations of reduced electric dipole matrix elements pointed towards a discrepancy between the calculated and the measured value for the $\langle 7s||r||7p_{1/2}\rangle$ and $\langle 7s||r||7p_{3/2}\rangle$ matrix elements [73–75]. The determination of these reduced E1 matrix elements was derived from a measurement of the static Stark polarizability of the $7s$ state by Bennett [76]. Here we report a new high precision measurement that differs from that of Bennett and somewhat reduces the discrepancy between the two techniques used for determining β.

5.2 Measurement of the static polarizability of the $7s$ state in cesium

The application of an external electric field shifts the energy of a state according to,

$$\Delta U = -\frac{1}{2}\alpha E^2, \tag{5.1}$$

where α is the static polarizability of the state. To help distinguish this polarizability from the other two mentioned previously, we will add a subscript $7s$. We determine α_{7s} of the

$7s$ state of atomic cesium by measuring the relative frequency shift of the $6s\,^2S_{1/2}$ and the $7s\,^2S_{1/2}$ states,

$$\Delta\nu = \frac{\alpha_{6_S} - \alpha_{7_S}}{4\pi} E^2. \tag{5.2}$$

This equation shows a frequency shift of the $6s \rightarrow 7s$ transition that varies quadratically with the applied electric field due to the difference in polarizabilities of the excited and ground state, $\alpha_{6s} - \alpha_{7s}$. When combined with precise measurements of the static polarizability of the ground state α_{6s} [77, 78], $\Delta\nu$ can be evaluated to determine α_{7_S}. This frequency shift varies linearly with the applied electric field squared and can be reported as a slope,

$$k = \frac{\Delta\nu}{E^2} = \frac{\alpha_{6_S} - \alpha_{7_S}}{4\pi}. \tag{5.3}$$

This static polarizability can be calculated through a sum-over-states method [79],

$$\alpha_{7s} = \frac{1}{3}\sum_n \left[\frac{|\langle 7s||r||np_{1/2}\rangle|^2}{E_{np_{1/2}} - E_{7s}} + \frac{|\langle 7s||r||np_{3/2}\rangle|^2}{E_{np_{3/2}} - E_{7s}} \right]. \tag{5.4}$$

Using this equation, we can see that a large contribution to α_{7s} will come from the $7p$ levels since they are much closer in frequency than other p levels. When we combine a high precision measurement of α_{7s} with $\langle 7s||r||n'p_{1/2}\rangle$ and $\langle 7s||r||n'p_{3/2}\rangle$ matrix elements where $n' \neq 7$, we are then able to calculate our $\langle 7s||r||7p_{1/2}\rangle$ and $\langle 7s||r||7p_{3/2}\rangle$ matrix elements. Since the largest contribution to α_{7s} comes from these $\langle 7s||r||7p_J\rangle$ matrix elements, this result is a precise technique for evaluating $\langle 7s||r||7p_J\rangle$. This technique also requires a calculation of the ratio of the $\langle 7s||r||7p_J\rangle$ matrix elements. Our theory friends are very good at calculating this ratio to the 0.014% level [73–75, 80].

5.3 Experimental configuration

This experiment was conducted with an atomic beam of cesium that was generated in an effusive oven. The atomic beam is further collimated using a 1 mm aperture 30 cm after the oven nozzle. The atomic beam travels along the vacuum chamber where the atoms are prepared into a single hyperfine state, excited with a 2-photon transition, and then detected on the previously emptied hyperfine state via a cycling transition.

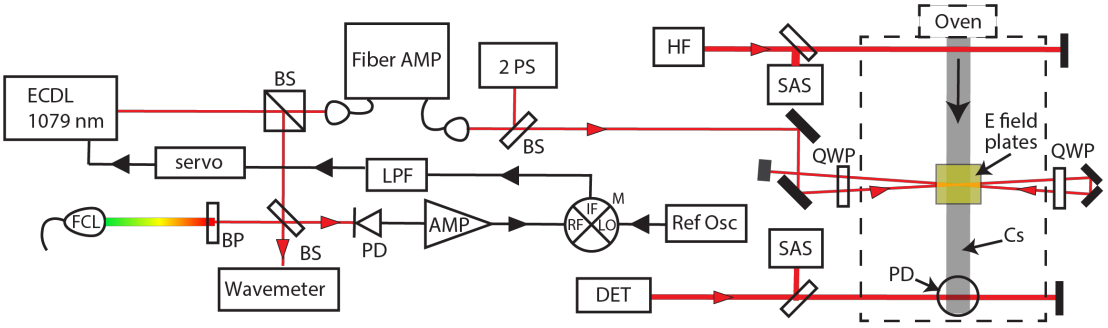

Figure 5.1. Experimental configuration for the $7s$ Stark shift measurement. We stabilize the frequency of the 1079 nm laser (ECDL) light to the frequency comb laser (FCL) using an optical phase-lock loop and sweep the offset by varying the reference oscillator driving the local oscillator (LO) port of the mixer (M). The following elements are labeled as; BP - band pass filter, PD - photodetector, BS - beam splitter, LPF - low pass filter, SAS - saturated absorption spectroscopy cell, 2PS - two photon spectroscopy in a vapor cell, QWP - quarter wave plate, DET - detection laser, HF - hyperfine laser. The dashed section illustrates the vacuum chamber, which contains the field plates and detection system.

The experimental configuration of this measurement is illustrated in Fig. 5.1. Here a 1079 nm ECDL with 50 mW of power is split for frequency stabilization and for amplification in a ytterbium doped fiber amplifier (YDFA). The amplified light (10 W) is directed into the vacuum chamber where it intersects an atomic beam of cesium. This amplified light is nearly perpendicular to the atomic beam and is retro-reflected so that both the forward and return beams overlap at the atomic beam. The reflected beam is then safely dumped. The crossing angle between the two unfocused beams is ≈10 mrad. A quarter waveplate before the vacuum chamber generates circular polarization and the second quarter waveplate changes the handedness of the polarization for the return beam. This forces the cesium atoms to only absorb a single photon from each direction and not two photons from a single direction [43]. This further reduces the Doppler width of the transition. The observed transition is primarily broadened due to the transition lifetime (3.3 MHz) and residual Doppler broadening from the crossing angle, resulting in an observed linewidth of ≈ 3.8 MHz. Transit time broadening is estimated to be 250 kHz and collisional effects are expected to be negligible due to the high vacuum, 5×10^{-7} Torr.

To DC Stark shift the $7s$ state, we apply a large electric field around the interaction region (where the atomic and laser beams intersect). To generate this precise and large electric field, we constructed a parallel plate structure using two unprotected gold-coated 2" square mirrors. The mirrors are spaced by three precision ceramic spacers and these three spacers give a field plate spacing of 8.169 (1) mm. We apply up to 5 kV to the plates and measure this voltage with a precision voltage divider. This divided voltage is continuously monitored during the experiment using a freshly calibrated 7.5 digit digital multimeter. The contributions to the electric field uncertainty are listed in Table 5.1

Table 5.1. Contribution to the uncertainty in the applied electric field. This uncertainty (times two) constitutes the systematic error of the differential polarizability. *We apply up to 5 kV.

Source of error	relative size (ppm)
Spacer length	122
Divider ratio	50
Divider nonlinearity	5/kV*
Voltage measurement	22
Divider temperature	10
Plate flatness	10
Total	137

The picked-off portion of the 1079 nm beam is combined and beat with a commercial frequency comb laser source. The frequency of the 1079 nm laser is stabilized in an optical-phase-lock loop to a tooth of the frequency comb laser source. The carrier-envelope offset frequency and repetition rate of the frequency comb are locked to a GPS conditioned reference (Endrun Meridian II). The OPLL is completed by mixing down the beat note and low pass filtering to generate an error signal to control the laser current. Although the comb teeth have an extremely narrow linewidth relative to one another, the absolute linewidth of the comb teeth is around 65 kHz.[1]

In this measurement, we minimize the stray magnetic fields in the interaction region by observing the Raman spectra while only hyperfine pumping. Under no magnetic field, there

[1]↑The comb teeth beating together generate a beatnote that is so narrow that we don't have the proper equipment to measure it, a phase noise analyzer. The overall linewidth of the comb can be measured by itself! The output of the f-2f interferometer shows the CEO and the phase noise of the comb.

are no Zeeman shifts and the individual magnetic Zeeman sublevels should be degenerate. The sublevels are often not quite degenerate and show up as broadening or even individual peaks. This Raman spectra and three orthogonal magnetic field coils are used to reduce the stray magnetic field to below 3 mG. The lower limit on stray field reduction is due to transit time broadening in the Raman transition. The resolution for the magnetic field control is finer than the small differences we see in the Raman spectra. For the ground state and PNC experiments, we use a larger beam size to further reduce stray fields below this 3 mG value.

Atoms are excited in the large electric field and the change in population is recorded as fluorescence from the cycling transition in the detection region. Spectra are collected by stepping the reference oscillator that is used to down mix the beat signal. After each frequency step, we wait 50 ms for the signal to stabilize and collect 240 voltage measurements at a rate of 480 Hz. The bandwidth of the detection signal is around 550 Hz. The individual voltage measurements are mostly, but not completely uncorrelated. Since we wait around 25 time constants, we ensure that the detection signal has stabilized after a frequency step. This eliminates apparent frequency shifts due to scanning speed. During each step, the power of the fiber amplifier is recorded as well as the beat frequency between the laser and the frequency comb. The reference oscillator is stepped up and down 15 MHz in 250 kHz steps for slightly over one minute. We then change the applied DC electric field and repeat the measurement. Sample scans are shown in Fig. 5.2. Here we show the fluorescence signal as the laser offset frequency is stepped relative to the frequency comb. The offset from the comb is labeled ν_{beat}. Since this is a two photon transition, the shift in center frequency of the $6s \rightarrow 7s$ transition is twice of the shift measured in the 1079 nm laser frequency.

We collect ten scans at each electric field. The primary source of noise is the Johnson-Nyquist noise in the large transimpedance gain (20 MΩ) of the photodiode amplifier. Each scan is fit to a Voigt profile with the following fitting parameters: offset, amplitude, center frequency, Gaussian width, and Lorentzian width. The line centers for the six electric fields are then fit against the electric field squared to determine the slope (polarizability) for this transition. This procedure is repeated ten times for the $F = 3$ transition. The fit for the $6s, F = 3 \rightarrow 7s, F = 3$ spectra is shown is Fig. 5.3. These measurements are repeated fifteen times for the $6s, F = 4 \rightarrow 7s, F = 4$ transition. The fluorescence peaks for the $F = 4$

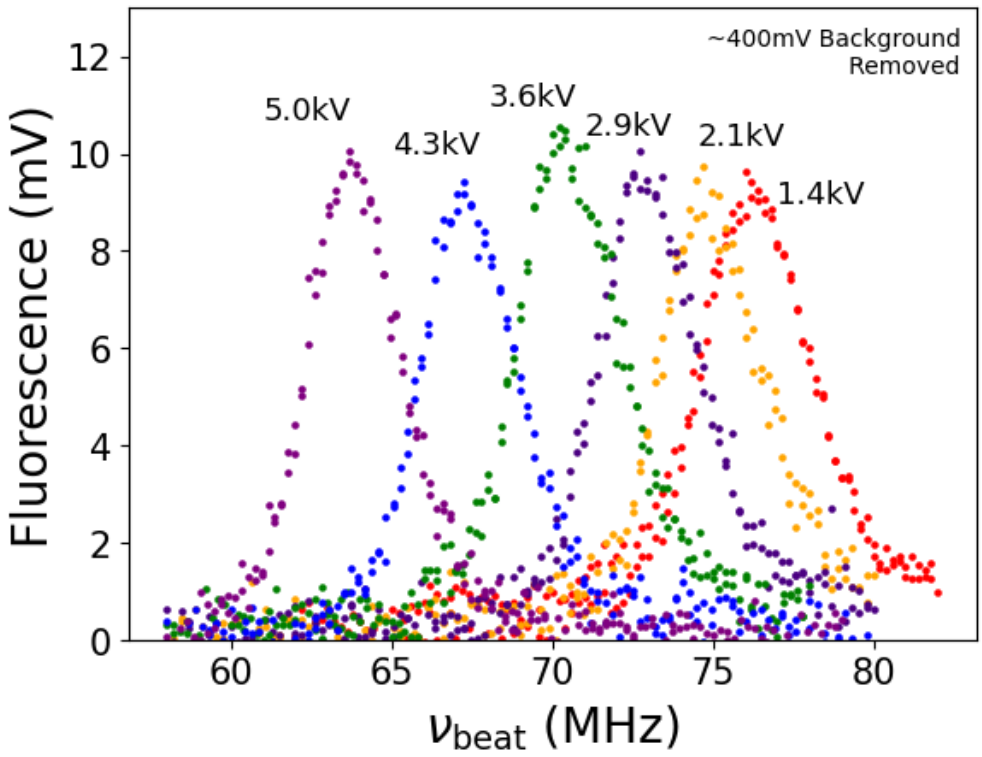

Figure 5.2. Single spectral scans of the $6s\ F = 3 \rightarrow 7s\ F = 3$ transition for each electric field value applied. The frequency ν_{beat} is the frequency difference between the ECDL and the frequency comb tooth.

transition are smaller by a factor of 3-4. The average uncertainty for an individual peak center fit for the $F = 3$ transition is 10 kHz and for the $F = 4$ transition is 15 kHz. The linewidth and amplitudes do not change as the applied electric field is varied. There is no difference in the fitted slope when the direction of the applied electric field is reversed.

The weighted average of the fitted slopes for the $6s, F = 3 \rightarrow 7s, F = 3$ transition is $k_{F=3} = 0.72267(23)^{stat}(20)^{sys}\text{Hz(V/cm)}^{-2}$ where the stat and the sys indicate the statistical and the systematic uncertainty. The weighted average for the $6s, F = 4 \rightarrow 7s, F = 4$ was $k_{F=4} = 0.72229(32)^{stat}(20)^{sys}\text{Hz(V/cm)}^{-2}$. The average Stark shift slope is $k = (7k_{F=3} + 9k_{F=4})/16$, where 7 and 9 are the degeneracies of the $F = 3$ and $F = 4$ states. We combine the systematic uncertainties in quadrature and have a final value for $k = 0.72246(29)\text{Hz(V/cm)}^{-2}$ with a relative uncertainty of 0.04%.

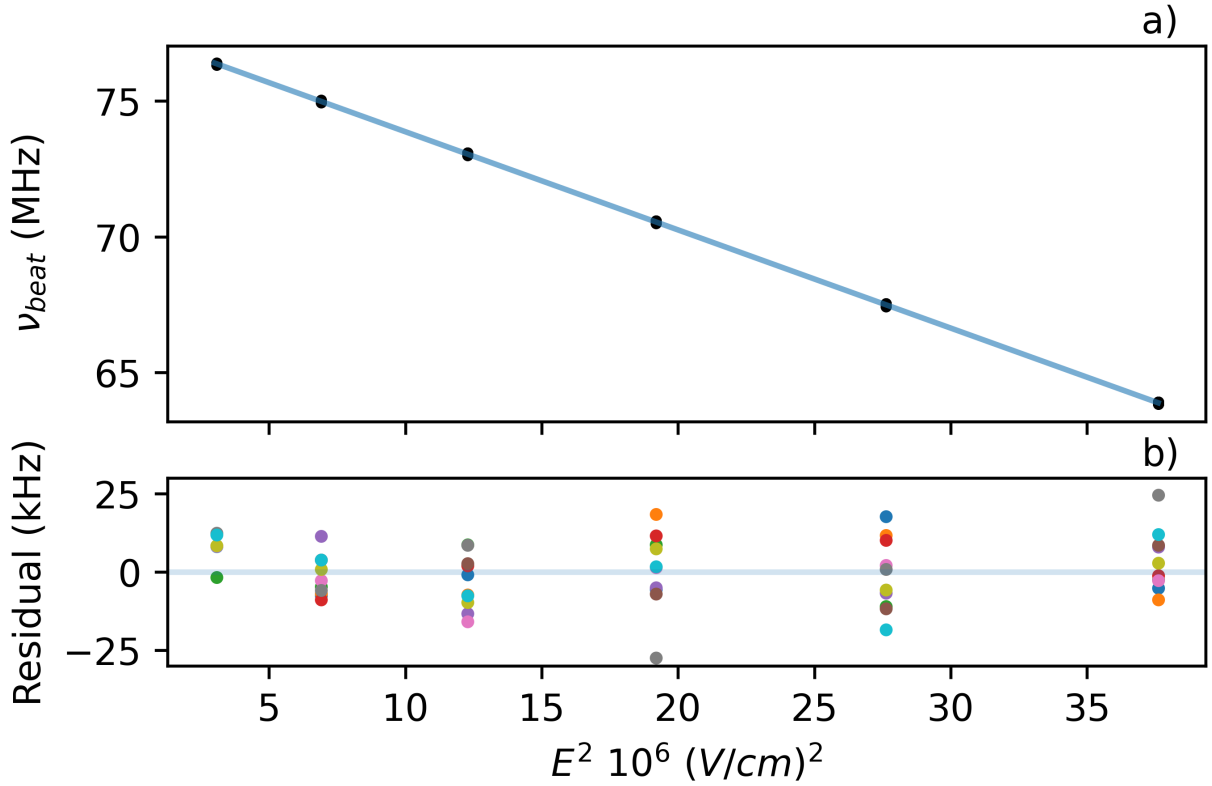

Figure 5.3. Fitted peak frequency relative to nearest comb tooth vs. applied electric field squared. Plot a) shows each of the 10 fitted centers averaged for each electric field for all of the runs on the $6s\ F = 3 \rightarrow 7s\ F = 3$ transition. Plot b) shows the residuals of those linear fits.

Our result and previous determinations of k and the polarizability α_{7s} are listed in Table 5.2. These bold entries are calculated using a weighted average of the two most precise values for the ground state polarizability [77, 78]. Values above the double line are experimental determinations and the values below the double line are theoretical. This result is ≈0.5% smaller that that of [76], a 4.7σ deviation.

Even though our value significantly deviates from that of Bennett, we have confidence in our measurement for several good reasons. We have the benefit of working with symmetric, near lifetime limited lineshapes whose amplitude does not change with DC electric field. The work of Bennett [76] utilized the Stark transition and a power-build-up cavity to excite this transition at 539.5 nm. Their lineshapes varied significantly as a function of the DC electric field and were not symmetric. It is difficult to find the line center of asymmetric lineshapes.

Also, we have the luxury of a frequency comb laser source to which we could stabilize our laser. Bennett did not. At the time of their measurement in 1999, Ted Hänsch and Jan Hall hadn't invented the frequency comb yet. Bennett had to stabilize their laser to a Fabry-Perot cavity and take back-and-forth measurements to subtract the sizable cavity drift.

Table 5.2. Determinations of the static polarizability of the $7s$ state. Calculated values are bold. Experimental determinations are above the double line and theoretical are below. See [81] on converting units of polarizabilities.

	k (Hz(V/cm)$^{-2}$)	α_{7s} (a_0^3)
This work	0.72246(29)	**6207.9(2.4)**
Bennett *et al.* [76]	0.7262(8)	**6238(6)**
Watts *et al.* [82]	0.7103(24)	6111(21)
Hoffnagle *et al.* [83]	**0.7803(480)**	6673 (386)
Van Wijngaarden *et al.* [84]	**0.7140**	6140
Zhou *et al.* [85]	**0.7042**	6061
Blundell *et al.* [31]	**0.72572**	6234.1
Bouchiat *et al.* [86]	0.7225	**6208**

5.4 α_{7s} results

We use Eqn. 5.4 to calculate the contributions of each reduced E1 matrix element to the DC Stark polarizability of the $7s$ state, α_{7s}. We use the experimental matrix elements $\langle 7s||r||6p_J\rangle$ [87, 88] and the theoretical matrix elements from [18] for the higher np_j states, $8 \leq n \leq 12$. All of these contributions are added up and subtracted from the measured value and the remaining portion is due solely to the $\langle 7s||r||7p_J\rangle$ matrix elements. The relative amplitude of the $\langle 7s||r||7p_{3/2}\rangle$ and $\langle 7s||r||7p_{1/2}\rangle$ elements are then used to calculate these elements. A summary of this calculation is shown in Table 5.3. The contributions to α_{7s} are in the 5th column (headed α_{7s} (a_0^3)) and its uncertainty in the 6th column (headed $\delta\alpha_{7s}$ (a_0^3)). Here we see the contributions to α_{7s} from all of the np_J where $J \neq 7$. This contribution make up less than 10% of the total α_{7s} polarizability. This small contribution allows a

precision determination of the $\langle 7s||r||7p_J\rangle$ elements from a precision determination of α_{7s}. The results are $\langle 7s||r||7p_{1/2}\rangle = 10.303(3)\ a_0$, where a_0 is the Bohr radius, and $\langle 7s||r||7p_{3/2}\rangle = 14.311\ (3)\ a_0$. Our results for these matrix elements and previous determinations are listed in Table 5.4. The matrix elements from this work agree well with theoretical determinations and disagree with the experimental result of Bennett [76] and Watts [82].

Table 5.3. E1 matrix elements, eigenstate energies, and contributions to the Stark polarizability α_{7s}. This table shows our sum-over-states calculation of the Stark polarizability α_{7s}. E1 elements for $n = 6$ and 7 are experimental values, as discussed in the text. [a]Refs. [87, 88], [b]Refs. [77, 78, 89–97], [c]Ref. [76] and this work, [d]Ref. [98]. Theory values of E1 elements $8 \le n \le 12$ are from Ref. [75], while those for $n = 13$ and 14 are from Ref. [49]. State energies (rounded here to two decimal places after the point) are found in NIST tables [99].

n	$d\ (a_0)$	$\delta d(\%)$	$E_{np_j}\ (\mathrm{cm}^{-1})$	$\alpha_{7s}\ (a_0^3)$	$\delta\alpha_{7s}\ (a_0^3)$
	$\langle 7s\|\|r\|\|np_{1/2}\rangle$				
6	-4.249^a	0.094	11178.27	−179.52	0.34
7	-	-	21765.35	-	-
8	0.9263	0.30	25708.84	8.75	0.05
9	0.3414	0.41	27637.00	0.94	0.01
10	0.1848	0.48	28726.81	0.25	0.002
11	0.1200	0.62	29403.42	0.10	0.001
12	0.0858	0.61	29852.68	0.05	0.001
13	0.069	1.05	30165.67	0.03	0.001
14	0.056	1.04	30392.87	0.02	0.0004
	$\langle 7s\|\|r\|\|np_{3/2}\rangle$				
6	-6.489^a	0.077	11732.31	−452.80	0.70
7	-	-	21946.39	-	-
8	1.6355	0.15	25791.51	26.97	0.08
9	0.6703	0.21	27681.68	3.60	0.02
10	0.3876	0.19	28753.68	1.08	0.004
11	0.2635	0.31	29420.82	0.47	0.003
12	0.1952	0.32	29864.54	0.25	0.002
13	0.158	3.7	30174.18	0.16	0.012
14	0.129	3.9	30399.16	0.10	0.008
			$\alpha_{n>14,j=1/2} =$	0.02	0.02
			$\alpha_{n>14,j=3/2} =$	0.10	0.10
			$\alpha_{n\neq 7} =$	−589.34	0.79

Table 5.4. Comparison of matrix elements $\langle 7s||r||7p_{1/2}\rangle$ and $\langle 7s||r||7p_{3/2}\rangle$. Experimental determinations are above the double line and theoretical are below. *These matrix elements were derived from the measurements of Bennett *et* al. [76] and reported in Ref. [100].

	$\langle 7s\|\|r\|\|7p_{1/2}\rangle$ (a_0^3)	$\langle 7s\|\|r\|\|7p_{3/2}\rangle$ (a_0^3)
This work	10.303 (3)	14.311 (3)
*Bennett *et al.* [76]	10.325 (5)	14.344 (7)
Tran Tan *et al.* [75]	10.292 (6)	14.297 (10)
Roberts *et al.* [73, 74]	10.297 (23)	14.303 (33)
Safronova *et al.* [80]	10.310 (40)	14.323 (61)
Dzuba *et al.* [101]	10.285 (31)	14.286 (43)

5.5 α and β results

Since the 2019 letter by Toh, we have gained new higher precision reduced E1 matrix elements for $8 \leq n \leq 12$ and better values for the tail and valence core contributions to α [18, 19]. We use these values and the result of this work to update the sum-over-states calculation of the Stark scalar polarizability α in [71]. This sum-over-states calculation is tabulated in Table 5.5.

The motivation for this Stark shift measurement was to help solve the discrepancy between the two techniques for evaluating β. See Figure 5.4 for a quick summary of these determinations. The first method uses a theoretical value for the hyperfine changing component of the magnetic dipole interaction, M_1^{hf} [72] and a measurement of M_1^{hf}/β [35] to find $\beta_{M1} = 26.957\ (51)\ a_0^3$, the subscript on β indicates the technique with which it is evaluated. β_{M1} showed significant disagreement with the second method for evaluating β. This technique was used in [71] to find $\beta_\alpha = 27.139\ (42)\ a_0^3$. With our updated matrix elements from [18, 19] and this work, we calculate $\beta_\alpha = 27.043\ (36)\ a_0^3$. The reduction in β_α comes from (1) the new Stark shift measurement ($\Delta\beta = -0.031\, a_0^3$), (2) the improved theoretical values for E1 matrix elements for $8 \leq n \leq 12$ [18] ($\Delta\beta = -0.048\, a_0^3$), and the improved value of the

valence-core and tail ($n > 12$) contributions to the polarizability [19] ($\Delta\beta = -0.018\, a_0^3$). A weighted average of this result, β_α, with β_{M1} yields $\beta = 27.014\ (30)\ a_0^3$

Since these two determinations originate from entirely unique sets of measurements and theoretical determinations, correlation among these two values is minimal and the uncertainty is the quadrature sum of the individual uncertainties. This assumption also relies on the fact that β is independent of hyperfine levels. This is valid at the current measurement precision [102].

Tran Tan and Derevianko also calculate α exclusively with their theoretical reduced E1 matrix element and combine this result with [45] to get $\beta = 26.887\ (38)\ a_0^3$. Although determinations of β are more consistent, further investigations are necessary to resolve the remaining discrepancy. We propose new measurements of M_1^{hf}/β and measurement of reduced E1 matrix elements $\langle 6s||r||7p_J\rangle$. The motivation for the former is that it has only been measured to a high precision once [35]. For the latter, the $\langle 6s||r||7p_J\rangle$ matrix elements vary significantly from the calculated values of [18]. See Figure 5.5. For all but the $\langle 6s||r||7p_J\rangle$ moments, their calculations agree nicely with experiment. A new measurement here could resolve this discrepancy.

In this Stark shift measurement, we apply a large dc electric field to the atoms, and drive a Doppler-free two-photon $6s\ ^2S_{1/2} \rightarrow 7s\ ^2S_{1/2}$ transition using the output of a 1079 nm external cavity diode laser (ECDL). This transition has a symmetric, near-lifetime-limited lineshape that does not vary with the applied dc electric field. This results in a simple accurate line center determination that is critical to measuring high precision Stark polarizabilities. We measure the shift in the transition frequency as a function of the applied electric field and determine the static polarizability. We use this static polarizability to reevaluate the reduced E1 matrix elements $\langle 7s||r||7p_J\rangle$. From these elements we recalculate α and ultimately β.

This measurement was completed in the Fall of 2024. For this measurement, Aidan Jacobsen aided in the construction of the electric field plates as well as with writing the Labview program for data collection. Aidan also helped with constructing and evaluating the high precision voltage divider that we used. This work has been published in Physical Review Letters [106].

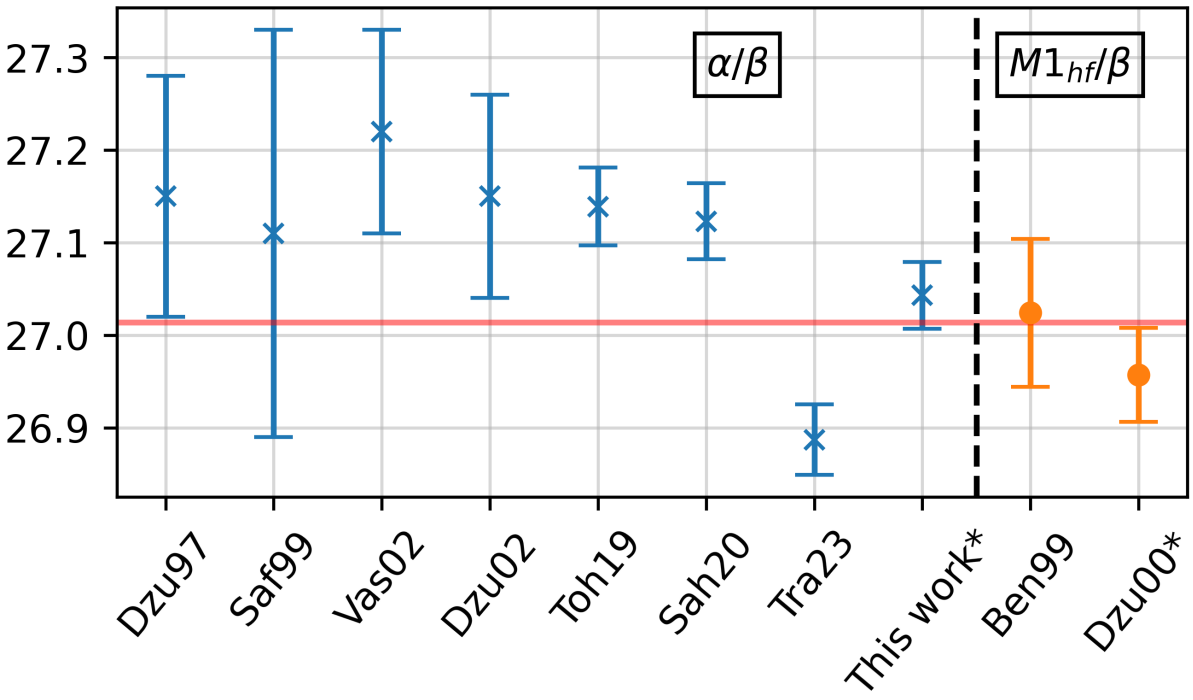

Figure 5.4. Comparison of previous determinations of β [19, 54, 72, 76, 100, 101, 103–105] with the result of this work. These determinations are identified by the first three letters of the first author's name and the abbreviated publication year. The blue values to the left of the dotted line are determined using the sum-over-states technique. The orange values to the right of the dotted line are determined by the $M1_{hf}$ technique. The pink horizontal line indicates our recommended value, a weighted average of the two most precise determinations from each technique. The two values are highlighted with an asterisk.

Table 5.5. E1 matrix elements, eigenstate energies, and contributions to the scalar polarizability α. This table shows our sum-over-states calculation, as given in Eqn. 2.4, of the scalar polarizability α. E1 elements for $n = 6$ and 7 are experimental values, as discussed in the text. [a]Refs. [87, 88], [b]Refs. [77, 78, 89–97], [c]Ref. [76] and this work, [d]Ref. [98]. Theory values of E1 elements ($8 \leq n \leq 12$) are from Ref. [75]. State energies (rounded here to two decimal places after the point) are found in NIST tables [99].

n	d (a_0)	δd(%)	$\delta\alpha$ (a_0^3)	d (a_0)	δd(%)	$\delta\alpha$ (a_0^3)	$E_{np_{1/2}}$ (cm^{-1})	α (a_0^3)	$\delta\alpha$ (a_0^3)
	$\langle 7s\|\|r\|\|np_{1/2}\rangle$			$\langle np_{1/2}\|\|r\|\|6s\rangle$					
6	-4.249^a	0.094	0.031	4.5057^b	0.035	0.011	11178.27	−32.54	0.03
7	10.303^c	0.03	0.011	0.2781^d	0.16	0.060	21765.35	−37.27	0.06
8	0.9263	0.30	0.0014	0.0753	1.3	0.0060	25708.84	−0.455	0.006
9	0.3414	0.41	0.00023	0.0308	2.0	0.0011	27637.00	−0.056	0.001
10	0.1848	0.48	0.00007	0.0153	2.7	0.0004	28726.81	−0.0137	0.0004
11	0.1200	0.62	0.00003	0.0088	4.3	0.0002	29403.42	−0.0048	0.0002
12	0.0858	0.61	0.00001	0.0052	5.2	0.0001	29852.68	−0.0020	0.0001
	$\langle 7s\|\|r\|\|np_{3/2}\rangle$			$\langle np_{3/2}\|\|r\|\|6s\rangle$					
6	-6.489^a	0.077	0.072	-6.3398^b	0.035	0.033	11732.31	−92.93	0.08
7	14.311^c	0.02	0.020	-0.5742^d	0.10	0.102	21946.39	−101.82	0.10
8	1.6355	0.15	0.003	−0.2097	0.48	0.011	25791.51	−2.215	0.01
9	0.6703	0.21	0.001	−0.1133	0.64	0.003	27681.68	−0.404	0.003
10	0.3876	0.19	0.0003	−0.0730	0.56	0.001	28753.68	−0.137	0.001
11	0.2635	0.31	0.0002	−0.0526	0.89	0.001	29420.82	−0.064	0.001
12	0.1952	0.32	0.0001	−0.0401	0.95	0.0003	29864.54	−0.035	0.003
							$\alpha_{n>12} =$	−0.32	0.09
							$\alpha_{vc} =$	+0.40	0.10
							$\alpha =$	−267.86	0.20

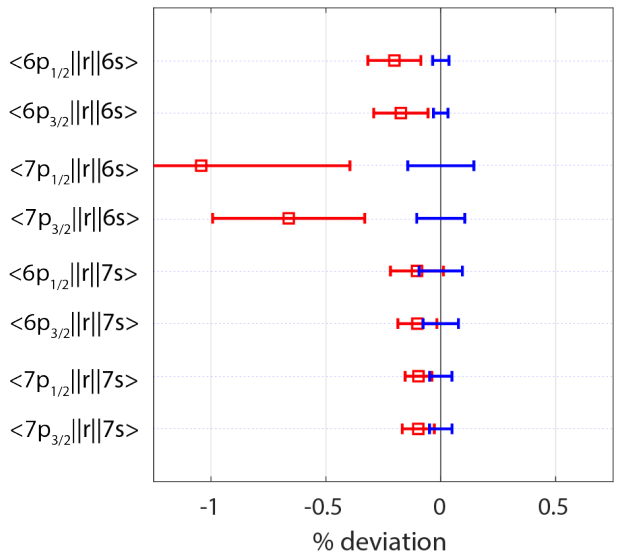

Figure 5.5. Comparison of theoretical and experimental E1 moments $\langle np_j||r||ms\rangle$ for $m, n = 6$ and 7 and j = 1/2 and 3/2. The experimental values are shown at zero deviation, with the blue error bars showing their relative uncertainty (ranging from 0.1% - 0.2%). The calculated results are those of Tran Tan and Derevianko [75] (red, □).

6. A NEW MEASUREMENT OF THE RATIO α/β

The motivation for a new α/β measurement is similar to that of the measurement of the dc Stark shift of the $7s$ state. After completion of the Stark shift measurement, the difference between the two determinations yielding the vector Stark transition polarizability, β, was reduced. This difference is $\beta_\alpha - \beta_{M1} = \Delta\beta = 0.086(62)$, where the number in parenthesis is the quadrature sum of the two individual uncertainties. Although reduced, this deviation is still too large for comfort due to its importance in calculating Q_w. Looking to rectify this discrepancy, we chose to measure the ratio of the scalar to vector transition polarizability, α/β. This measurement was actually started first. Due to two fiber amplifier failures and having to share the vacuum system and Raman lasers with the ground state measurement, this experiment took much longer than anticipated.

6.1 Two-pathway coherent control

To measure the ratio α/β, we chose a two-color coherent control technique to interfere the relatively small Stark amplitude with a larger two-photon transition. When driving atoms via two distinct coherent transitions, the total transition rate is proportional to

$$\mathcal{W} \propto \left| A_{2\mathrm{p}} + A_{\mathrm{St}} \right|^2,$$

where $A_{2\mathrm{p}}$ and A_{St} are the transition amplitudes for the two-photon and Stark transitions respectively. If coherence is maintained, the rate can be simplified to,

$$\mathcal{W} \propto |A_{2\mathrm{p}}|^2 + |A_{\mathrm{St}}|^2 + \left(A_{2\mathrm{p}} A_{\mathrm{St}}^* + A_{2\mathrm{p}}^* A_{\mathrm{St}} \right). \tag{6.1}$$

Here we have two dc terms for the direct two-photon and Stark transitions and we have an interference term that can be modulated by varying the phase of the two transitions. Next, we have the two-photon transition amplitude,

$$A_{2\mathrm{p}} = \tilde{\alpha} \boldsymbol{\varepsilon}^\omega \cdot \boldsymbol{\varepsilon}^\omega \delta_{F,F'} \delta_{m,m'} \mathrm{e}^{-2\mathrm{i}\phi^\omega}. \tag{6.2}$$

$\tilde{\alpha}$ is the scalar polarizability for the two-photon transition. It is quite similar to the Stark vector polarizability, but it should not be confused with α. $\boldsymbol{\varepsilon}^{\omega}$ is the electric field of the laser with frequency ω. δ is the Kronecker delta function forcing $\Delta F = 0$ and $\Delta m = 0$ transitions. Finally, we have a phase for the electric field of the laser, $\mathrm{e}^{-2\mathrm{i}\phi^{\omega}}$. The Stark amplitude is as follows,

$$\begin{aligned} A_{\mathrm{St}} &= \Big\{[\alpha \mathbf{E}\cdot\boldsymbol{\varepsilon}^{2\omega}\delta_{F,F'} + \mathrm{i}\beta\left(\mathbf{E}\times\boldsymbol{\varepsilon}^{2\omega}\right)_z C_{F,m}^{F',m'}]\delta_{m,m'} \\ &\quad +[\pm\mathrm{i}\beta\left(\mathbf{E}\times\boldsymbol{\varepsilon}^{2\omega}\right)_x - \beta\left(\mathbf{E}\times\boldsymbol{\varepsilon}^{2\omega}\right)_y]C_{F,m}^{F',m'}\delta_{m,m'\pm1}\Big\}\,\mathrm{e}^{-\mathrm{i}\phi^{2\omega}}. \end{aligned} \tag{6.3}$$

This amplitude contains the scalar and vector transition polarizabilities, α and β. Here we see the relationship between the scalar term and the applied electric field, $E\cdot\boldsymbol{\varepsilon}$, and the vector term and the applied electric field, $E\times\boldsymbol{\varepsilon}$. We also have terms that are proportional to Clebsch-Gordon coefficients, $C_{F,m}^{F',m'}$. These components are dependent on the magnetic Zeeman sublevel. To interfere the scalar and vector Stark terms, we must select a field geometry that allows only the scalar or vector Stark transition. Since we will interfere with the two-photon transition, the transition must not change the magnetic Zeeman sublevel, hence $\Delta m = 0$. With a magnetic field along the laser propagation axis, $\vec{B} \parallel \vec{k}$, this condition is satisfied. Then the interference could be switched from α to β by changing the angle between the laser polarization and the applied electric field. This simplifies the Stark interference term to,

$$A_{\mathrm{St}} = E\varepsilon^{2\omega}\left[\alpha\cos\theta + \mathrm{i}\beta C_{F,m}^{F',m'}\sin\theta\right]\mathrm{e}^{-\mathrm{i}\phi^{2\omega}}, \tag{6.4}$$

where θ is the angle between the laser polarization and the applied electric field. From here we can vary the optical phase of the 2ω field relative to the ω field while switching between α (parallel) and β (perpendicular) to get the following ratio,

$$\mathcal{R} = \frac{\alpha}{\beta C_{F,m}^{F',m'}}. \tag{6.5}$$

This ratio can be further simplified by calculating the C coefficient. This coefficient is proportional to the average m quantum number $\langle m\rangle$. Since m ranges from $-F$ to F, some

state preparation is required to observe the β interference. We must also determine the value of $\langle m \rangle$ if we wish to measure α/β. The following ratio is what we measure when extracting α/β.

$$\mathcal{R} = \frac{4}{\langle m \rangle} \frac{\alpha}{\beta}, \tag{6.6}$$

The above ratio assumes the polarization of the laser is perfectly aligned either perpendicular or parallel to the static applied electric field. In the presence of imperfect polarization, this ratio is modified. We write this imperfect polarization of the 540 nm (green) as $\boldsymbol{\varepsilon^{2\omega}} = \hat{\boldsymbol{y}}\varepsilon_y + \hat{\boldsymbol{x}}\left(\varepsilon_x' + \mathrm{i}\varepsilon_x''\right)$, where ε_y represents the "good" polarization, ε_x' is the slight rotation of the polarization from the intended direction, and ε_x'' represents a slight circular polarization. Even with a new α-BBO Glan-laser polarizer[1] carefully aligned to the electric field axis, the effect of these slight imperfections in the polarization purity can cause significant modifications to the measured ratio on the 0.1% level. The following equation quantifies the effect of the imperfect polarization of the 540 nm beam on the observed ratio.

$$\mathcal{R}_\pm = \frac{4}{|\langle m \rangle|} \frac{\alpha}{\beta} \left(1 \mp \frac{4}{|\langle m \rangle|} \frac{\alpha}{\beta} \frac{\varepsilon_x''}{\varepsilon_y} + \left(\frac{4}{|\langle m \rangle|} \frac{\alpha}{\beta} \right)^2 \left[\left(\frac{\varepsilon_x''}{\varepsilon_y} \right)^2 - \frac{1}{2} \left(\frac{\varepsilon_x'}{\varepsilon_y} \right)^2 \right] \right) \tag{6.7}$$

The first correction term is due to the circular component of the green beam polarization and the second term is due to both the circular polarization and the misalignment. Here we have added a $\pm$ symbol to indicate the magnetic Zeeman pumping direction. Under a Zeeman reversal, the second term changes sign and would average out. The third term does not average out and must be minimized. Since $4\alpha/(\langle m \rangle \beta) \approx 13$, the ratios $\varepsilon_x'/\varepsilon_y$ and $\varepsilon_x''/\varepsilon_y$ must be kept small. We ensure this by minimizing birefringence in the optical view ports and by carefully rotating the polarization of the green beam to align with the electric field. We adjust $\varepsilon_x'/\varepsilon_y$ and $\varepsilon_x''/\varepsilon_y$ to be less than 1×10^{-3} and 5×10^{-4} respectively, making these corrections negligibly small. To extract the value of $\mathcal{R}$ we average successive measurements of $\mathcal{R}_+$ and $\mathcal{R}_-$.

[1]↑If you order a Glan-laser polarizer from overseas, ask the manufacture to not place the word laser on the outside of the box. US customs will hold it, delay delivery by a week, and require documentation from Purdue to release it.

6.2 Experimental configuration

Here we will discuss the experimental configuration, which is illustrated in Figure 6.1. We drive the $6s \rightarrow 7s$ transition with a laser that is resonant with the two-photon wavelength at 1079 nm. A portion of the 1079 nm light is used to stabilize its frequency to a tunable Fabry-Perot cavity. The rest of the 1079 nm light is greatly amplified in a rare earth element fiber amplifier up to 10 W of optical power. This intense beam is then focused into a periodically poled lithium niobate crystal for frequency doubling, second harmonic generation (SHG). This SHG light is at double the frequency and is phase coherent with the 1079 nm light. The 540 nm and 1079 nm light is separated and the 540 nm beam is phase shifted in a Mach-Zehnder interferometer. The beams are recombined, well polarized using an α-BBO polarizer, and then weakly focused on the atomic beam. A portion, 4%, of the amplified 1079 nm doubled passed through a heated vapor cell to reduce Doppler broadening. Fluorescence through the side of the vapor cell passes through a band pass filter centered on 852 nm and is collected on a PMT, Hamamatsu type R928. A 600 Hz dither is added to the Fabry-Perot length to modulate the laser frequency. The PMT output is demodulated in a lock-in amplifier to generate an error signal to stabilize the Fabry-Perot to the $6s, F = 3 \rightarrow 7s, F = 3$ transition.

The atomic beam is generated using an effusive oven and the beam geometry is collimated by 1 cm long stainless steel capillary tubes packed in a 8 mm high 12 mm wide opening. After collimation, the atomic beam is then pumped into the most extreme magnetic Zeeman sublevel ($m = \pm 3$) of the $6s, F = 3$ hyperfine ground state.

Once pumped, the atomic beam intersects the laser beams in the interaction region. Here an electric field is applied by 8 copper electrodes that are evenly spaced in a ring concentric to the laser propagation axis. Each electrode is 4.8 mm in diameter and the radius of the ring is 18 mm. The electrodes are biased and switched with a homemade high voltage switching circuit composed of several high voltage solid state relays. This circuit varies the bias voltages on the rods to produce an electric field in any of the eight possible directions. These potentials have been modeled and plots are show in Figure 6.2. We find that the electric field (430 V/cm is uniform to 20 mV/cm in the small interaction region

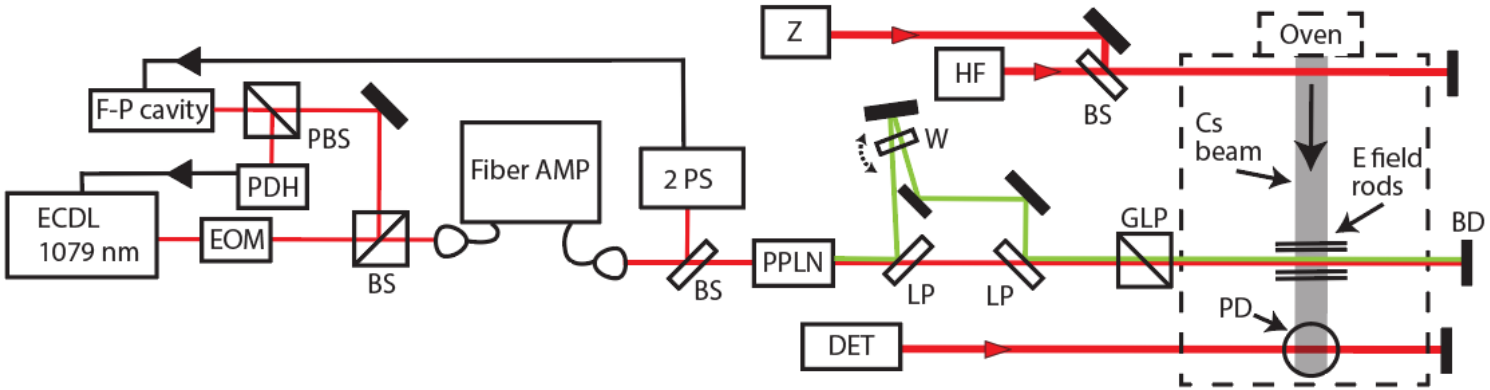

Figure 6.1. An experimental diagram of the α/β measurement. The 1079 nm ECDL is stabilized to a Fabry-Perot cavity (F-P cavity) and amplified in a fiber amplifier. This amplified 1079 nm beam is frequency doubled in a periodically-poled lithium niobate crystal (PPLN). The relative phase of the second harmonic at 540 nm and the fundamental at 1079 nm is varied in a Mach-Zehnder interferometer where one arm contains a galvanometer mounted window (W). The 540 nm and 1079 nm beams are recombined and polarized with a Glan-laser polarizer (GLP) before being focused and directed into the vacuum chamber. The following elements are labeled as; 2 PS - two-photon stabilization, ECDL - external cavity diode laser, PDH - Pound Drever Hall locking system, BD -beam dump, BS - beam splitter, PBS - polarizing beam splitter, DET - detection laser, Z - Zeeman laser, HF - hyperfine laser, LP - long pass filter, PD - photodetector, and EOM - Electro-optic modulator.

where the atomic beam and weakly focused laser beams overlap. To compare the scalar and vector Stark transition polarizability, we switch the applied electric field instead of relying on a rotation on the laser polarization. This reduces uncertainties in the polarization due to birefringence and in the 540 nm and 1079 nm beam overlap.

Atoms that undergo the $6s, F = 3 \rightarrow 7s, F = 3$ transition may decay down to the $6s, F = 4$ level. These atoms are then driven in a cycling transition 20 cm after the interaction region. This cycling transition scatters 100-200 photons for each $F = 4$ atom and around 10-20 are collected on a large area photodiode. This photocurrent is amplified in a transimpedance amplifier of gain 20 MΩ. This output voltage is then read by a lock-in amplifier. To vary the phase of the Stark transition relative to the two-photon transition, we linearly ramp (12 s) a window mounted galvanometer while slightly modulating (150 Hz) it. The 540 nm beam passes through the galvanometer mounted window twice when the beams are split inside of the Mach-Zehnder interferometer. This is to reduce the lateral shift of the green beam relative to the 1079 nm beam. As the window is ramped, the optical phase of the two laser beams scan at Ω =3.8 Hz. The fast 150 Hz modulation is then used as a reference to the lock-in amplifier to mix down this interference signal to Ω. The output of the lock-in is an ac modulation at the phase scanning frequency, Ω, that is proportional to the Stark$\rightarrow$two-photon interference. We record and digitally bandpass filter the lock-in output. The bandpass filter is centered on the phase modulation frequency, Ω, and reduces noise caused by phase fluctuations due to differing paths of the 1079 nm and 540 nm beams. For a single ramp cycle, we scan through >36 cycles. We show an example scan in Figure 6.3 where the blue trace is a scan of α interference and the orange trace is β interference. The inset to the right highlights the phase shift between the α transition and the β transition. The difference between these two scans is that the electric field was parallel to the green laser polarization for the α interference ane perpendicular for the β interference.

The lock-in amplifier output is internally low pass filtered to reduce noise at 150 Hz. This reduces the maximum rate at which we can scan the phase. We also must compensate for the switch between α and β scans by removing the first 2.6 s of the collected scan. We cut the resultant 36 cycle data set into 12 sections to avoid the effect of small phase fluctuations that are present during long scans. We fit each section with a sinusoid to determine the

amplitude. We record the average and standard error of the 12 fitted values in a single scan. The α and β interference amplitudes are combined to produce the ratio shown in Equation 6.6. After each scan of α and β, we change the pumping direction by reversing the handedness of the circularly polarized Zeeman beam that pumps the magnetic sublevels. This allows measurements of R_+ and R_-. We make 160 ratio measurements (80 of R_+ and 80 of R_-). We combine these measurements to attain a final ratio and uncertainty.

6.3 $\langle m \rangle$

As mentioned previously, we actually measure the quantity $(4/\langle m \rangle)(\alpha/\beta)$ since the α amplitude is independent of the magnetic Zeeman sublevel. This requires a precise determination of the average Zeeman sublevel, $\langle m \rangle$, when extracting the value α/β. For this measurement, we have greatly overhauled the optical pumping and state detection techniques. We have improved the pumping so that fewer than 1 atom in 2000 are in the wrong hyperfine level and around 99% of the pumped atoms are in the most extreme magnetic Zeeman sublevel. Although pretty good, the pumping is not perfect. Here we will discuss the technique for evaluating the pumping efficiency and how we determine $\langle m \rangle$.

The general technique for determining $\langle m \rangle$ is described in Section 3.6.2. Here we will discuss the specifics and what was done to reduce systematic errors. For state detection, we drive a $\Delta m = 0$ Raman transition from the $6s, F = 3$ to the $6s, F = 4$ ground state using Raman beams that are circularly polarized with the same handedness. We average 15 spectra and compare the observed peak areas to the calculated peak amplitudes. To avoid saturation effects, we operate at low laser powers where the peak amplitude grows linearly with the square of the Rabi frequency. We excite 1% to 1.5% of the atoms. The peak areas are determined by fitting the peak locations to determine the center frequencies. Once the peak centers are located, the data is spliced to extract single peaks. All peak splices have the same width, are centered on the peaks, and the width of the splice coincides with the peak to peak spacing to ensure the edges of the splice are far from the peak centers. The vertical offset is determined by averaging the first and last few data points in the peak splice. The offset is then subtracted from the peak amplitudes and the resultant data is integrated.

We compare these amplitudes without Zeeman pumping but with hyperfine pumping. The observed peak amplitudes agree with calculations to better than 7%. This is likely due to population redistribution during hyperfine pumping, but it is difficult to be certain and we must use this 7% when calculating the uncertainty in our technique. Although 7% sounds terrible for a precision measurement, not all hope is lost. If all of the atoms are in the $m = \pm 3$ states, then it doesn't really matter how well we know the peak amplitudes. All of the atoms are there and $\langle m \rangle = \pm 3$. This is almost true since our pumping is so good. If only a few atoms are in the $m = 2$ and $m = 1$ states, then only a small correction is needed. With this technique, we can determine $\langle m \rangle$ to better than 0.1%.

So, we are able to pump atoms into the most extreme Zeeman sublevel of the $F = 3$ hyperfine level. Don't we want to measure α/β on both the $6s, F = 3 \rightarrow 7s, F = 3$ and $6s, F = 4 \rightarrow 7s, F = 4$ transitions? Ideally, yes we would like to do that, but the Raman detection is more complicated on the $F = 4$ level for our field geometry. Since there are no $m = \pm 4$ magnetic sublevels in the $F = 3$ hyperfine level, we can't drive a $\Delta m = 0$ transition to observe the population in the $F = 4$ level. This detection scheme would then have to be modified to drive $\Delta m = \pm 2$ transitions for state detection. Unfortunately, $\Delta m = \pm 2$ transitions are 50-300 times weaker that $\Delta m = 0$ transitions. Driving $\Delta m = \pm 2$ transitions requires the two Raman beams to be circularly polarized with opposite handedness. In practice, it is not feasible to generate a high enough polarization extinction ratio between these two crossed circularly polarized beams to reduce the $\Delta m = 0$ transitions to smaller than 0.1% of the $\Delta m = \pm 2$. Our solution was to look to atomic theory.

Our theory friends [102] postulated a higher order Stark term, the tensor polarizability γ. This term would produce slight difference in the α/β ratio between measurements on the different hyperfine levels. The recent work of Xiao *et al.* [102], showed that this tensor term due to hyperfine coupling is around an order of magnitude smaller than the current measurement uncertainty. Since we can't measure the pumping efficiency to the 0.1% level and any differences between the ratio should be on the 0.01% level, we didn't measure α/β on the $6s, F = 4 \rightarrow 7s, F = 4$ transition. The only other measurement near this precision was by Weiman's group and they only measured on the $6s, F = 3 \rightarrow 7s, F = 3$ transition as well [45]. It would be interesting to search for a difference and observe this γ term,

but this would require over an order of magnitude improvement in signal-to-noise in this measurement geometry.

6.4 Systematic contributions to the α/β ratio

For a precision measurement examining weak transitions, careful consideration of other allowed transitions is critical. We select magnetic and electric field geometries as well as laser polarization to only drive the interactions under study. Other transitions can still cause systemic errors and we reduce their effects by careful alignment of magnetic and electric fields. For instance, we wish to drive the α and β Stark transitions. By aligning the magnetic field along the laser propagation direction, the M_1 interaction primarily drives $\Delta m = \pm 1$ magnetic dipole transitions that do not interfere with the 2-photon transition since we use two photons of equal frequency. Then the only systematic contribution due to the M_1 transition comes from stray magnetic fields that are not along $\hat{k}$. We null the stray magnetic field relative to the applied field in the interaction region to around a part in a thousand. Based on the strength of the magnetic dipole transition ($M_1/\beta \approx 29.5$ V/cm [4, 35]) and the strength of the applied electric field (430 V/cm), we reduce the systematic effects of the M_1 transition to 80 ppm.

To align the laser polarization to the static electric field, we apply an electric field rotated by $\pm 45°$ from the laser polarization. By comparing the ratio of the $\pm 45°$ interference amplitudes, we can align the laser polarization along the electric field to 1 mrad. This alignment error produces an uncertainty of 90 ppm in the measured ratio. We measure the polarization extinction ratio of two crossed polarizers before and after the chamber to be 2.5×10^{-7}. This indicates an uncertainty in ε_x'' to be less than $0.5 \times 10^{-3} \varepsilon_y$, where ε_x'' indicate the degree of circular polarization. The circular polarization introduces an uncertainty on the measured α/β ratio of 40 ppm. A summary of these main uncertainties and more is included in Table 6.1.

To search for systematic errors due to the applied electric field, we measure the α/β ratio with the laser polarization rotated from vertical to horizontal as well as with the electric field rotated by 180°. The ratio of α/β should be the same for 0°-90° ratio measurements as

Table 6.1. Sources and magnitudes of uncertainty for the determination of the ratio α/β. The primary sources of uncertainty originate from the fit and the determination of $\langle m \rangle$. We add the errors in quadrature to obtain the total uncertainty.

source of uncertainty	σ (ppm)
$\langle m \rangle$	670
fit	610
$\varepsilon'_x/\varepsilon_y$ (polarization alignment)	90
$\varepsilon''_x/\varepsilon_y$(circular polarization)	44
M_1	80
electric field	50
Total	920

it is for 180°-270° ratio measurements. This angle is the angle between the applied electric field and vertical. We also perform ratio measurement where the field is inverted back and forth, so 180°-0° ratio measurements. This ratio should be one since it compares α to α. Deviation here would indicate an asymmetric electric field. We see no significant deviation for these measurement except for when we rotated the laser polarization. The deviation due to rotation was 0.15% and could be caused by a slight ellipticity in the electrode apparatus, or by the measurement statistics. This will be discussed further in the next section.

6.5 Results

The relative uncertainty of 160 scans (80 $\mathcal{R}_+$ averaged with 80 $\mathcal{R}_-$) is typically around $0.15-0.2\%$. We believe deviations in this number are caused by building noises and vibrations that affect the phase coherence in the 540 nm and 1079 nm beams. The average reduced chi squared (χ^2_{red}) value among the data sets is 1.18. For any value of $\chi^2_{red} > 1$, we multiply the uncertainty by the square root of χ^2_{red}[107]. The primary uncertainty in the measurement

was due to shot noise in the 2-photon transition and relative phase fluctuations of the 540 nm and 1079 nm beams.

We searched for effects of ac Stark shifts on the α/β ratio by varying the intensity of the 540 nm and 1079 nm beams. No dependence was observed while varying the 540 nm beam power, but a slight dependence was noticed when varying the 1079 nm beam power. See Figure 6.5. We determine the α/β ratio by extrapolating the power dependent ratios back to zero intensity. We conduct experiments with the laser polarization vertically and horizontally aligned and see a slight deviation between the two results, $\alpha/\beta = -9.894\,(9)$ for vertical polarization and $\alpha/\beta = -9.909\,(7)$ for horizontal. This deviation could be caused by a slight ellipticity of the electrode apparatus and/or by measurement statistics. Since their uncertainties are similar and the unknown cause of the deviation, we report the unweighted average of the horizontal and vertical determinations as $\alpha/\beta = -9.902(6)_{stat}(7)_{sys}$ where stat and sys represent the statistical and systematics uncertainties. This value agrees very well with the value of Cho *et al.* [45], $\alpha/\beta = 9.905(11)$, but has slightly smaller uncertainty. The primary contribution to the systematic uncertainty is due to the $\langle m \rangle$ determination.

Previous experimental (green points) and theoretical (blues points) determinations of α/β are shown in Figure 6.6. The right most portion of the figure is an expanded scale plot of the two most precise measurements. We combine our result with that of Cho *et al.* [45] using a weighted average to produce our recommended value, $\alpha/\beta = -9.903(6)$. The pink line in the figure is our recommended value and the blue shaded region is its recommended uncertainty.

Figure 6.6 is unfair to the theoretical calculations since they must calculate α and β individually using a sum-over-states technique and then take the ratio. This is quite difficult since they depend on the same reduced matrix elements, but β has large amounts of cancellation. Atomic theorists are good at calculating α and when we combine that with a precision measurement of α/β, we have a much more precise value for β. When we combine our value for the scalar transition polarizability from section 5.5 with the new recommended value for α/β we get $\beta_\alpha = 27.048(26)\ a_0^3$. The most precise value for $\beta_{M1} = 26.957(51)\ a_0^3$ comes from a calculation of M_1^{hf}[72], and a laboratory determination of the ratio M_1^{hf}/β [35]. Figure 6.7 lists previous determinations of β using the sum-over-states approach (blue) and

the M_1^{hf} approach (green). The most precise value for β_α and β_{M1} differ from one another by $\beta_\alpha - \beta_{M1} = 0.091(57)$ or about 1.6σ.

6.6 Conclusion

This precision measurement of α/β was conducted using a coherent control technique to interfere a weak single photon transition with a much stronger two-photon transition. This technique facilitated a continuously phase shifted interference signal that minimizes uncertainties that would normally be present due to discrete phase shifts. We also further improve on the work of Antypas [21] and Wood [20] in improving the optical pumping efficiency and state read out precision. With this measurement, we confirm the results of Cho *et al.*[45] and do not further reduce the deviation between the two determinations of β. With the reduced uncertainty in our new value for β_α, the relative deviation between β_α and β_{M1} increased from 1.4σ to 1.6σ. This indicates a need for further study of this deviation. Our group is currently setting up a new measurement of the M_1^{hf}/β ratio with a three color coherent control technique that will allow interference measurements on all of the $6s \rightarrow 7s$ hyperfine transitions. This work was aided in part by Aidan Jacobsen who constructed the $\langle m \rangle$ reversal apparatus. This work has been published in Physical Review A [5].

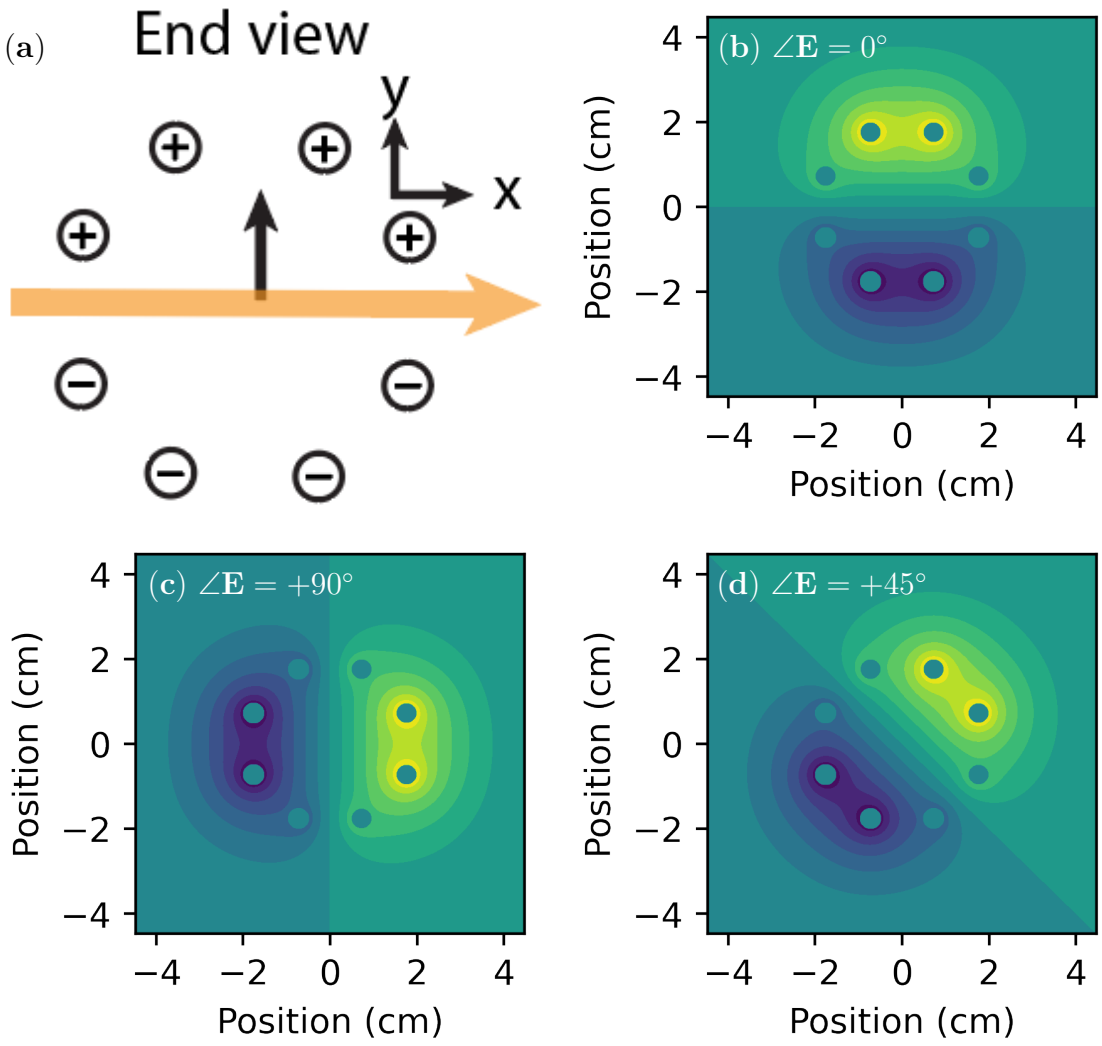

Figure 6.2. (a) Diagram illustrating the interaction region geometry and (b-d) modeled electric potentials generated by the circular arrangement of eight biased conducting rods. In (a) the large, orange arrow depicts the cesium beam and the small, black arrow depicts the laser polarization. The laser propagates into the page in each illustration (a-d). The rod assembly allows for rapid, reproducible rotation of the static electric field ($\mathbf{E}$) while the polarization ($\boldsymbol{\varepsilon}^{2\omega}$) remains fixed. The angle labeled in the figures ($\angle\mathbf{E}$) is specified relative to vertical.

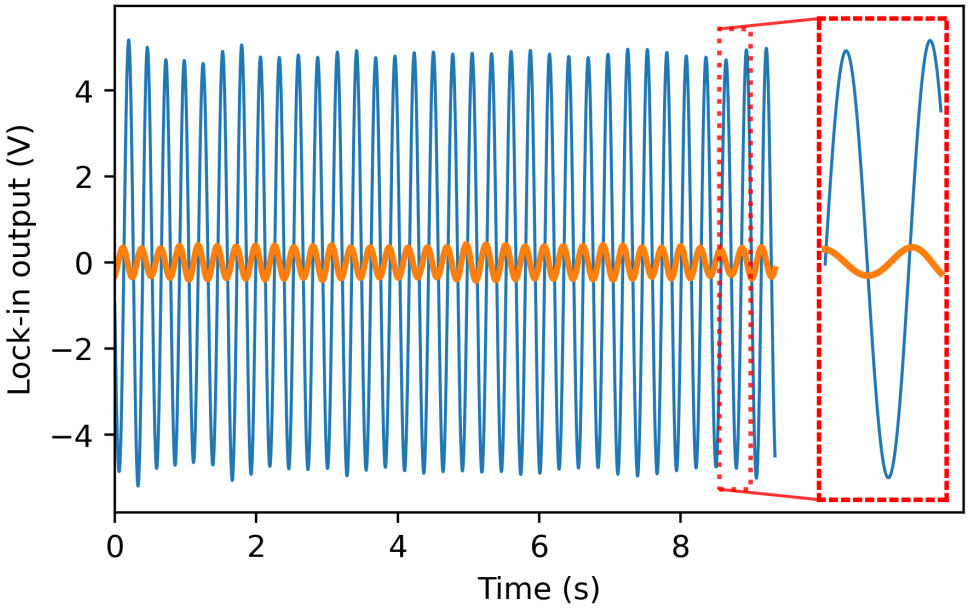

Figure 6.3. Representative examples of the bandpass-filtered output of the lock-in amplifier, showing the sinusoidal modulation vs. time, as the optical phase difference $\Delta\phi$ is scanned. Here atoms are prepared into the $m = +3$ Zeeman sublevel, so $C_{F,m}^{F'm'} = -3/4$. The larger (thin blue) trace demonstrates the α interference with an electric field parallel to the static polarization and smaller (thick orange trace) illustrates β interference. The inset plot (dotted red section) is horizontally stretched to highlight the phase difference between the α and β interference. This shift is consistent with a negative value for the ratio of α/β.

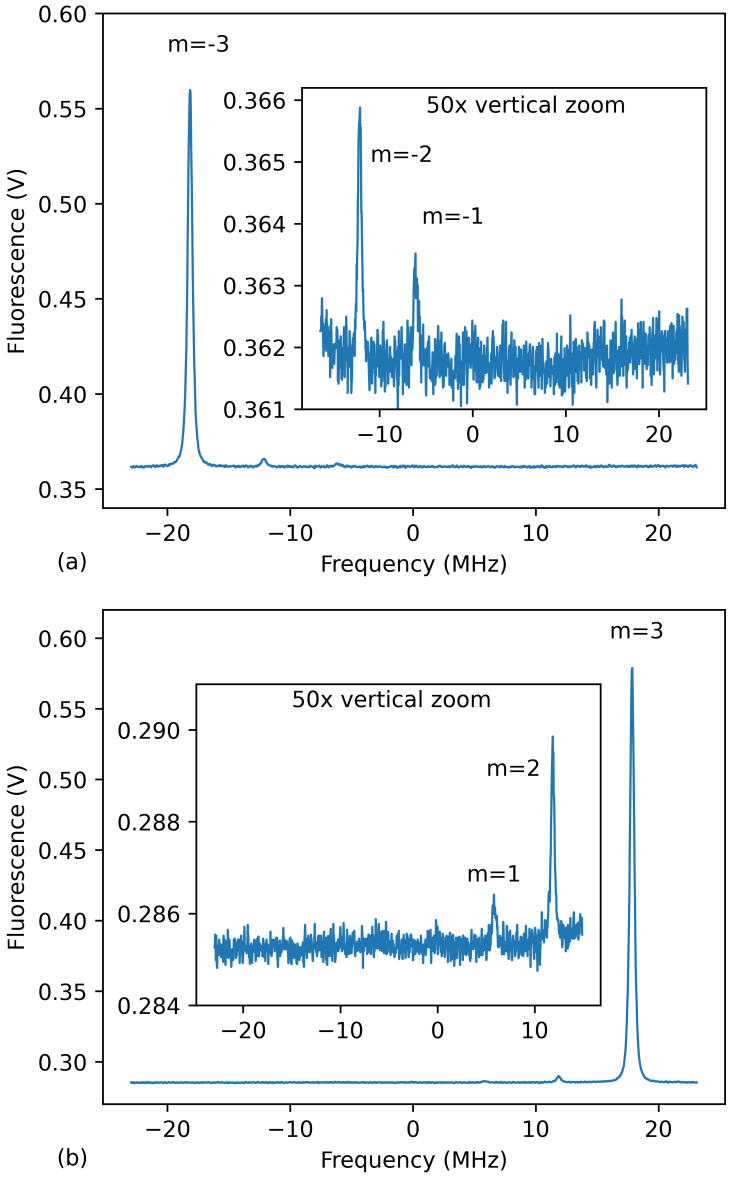

Figure 6.4. Raman spectra illustrating the effect of optical pumping of the cesium atoms to the most extreme magnetic Zeeman sublevel. Here we plot the detected population in the previously emptied hyperfine level versus the difference in frequency between the Raman lasers, centered on the 9.192 GHz ground state frequency. Atoms are pumped into the (a) $m = -3$ or (b) $m = +3$ Zeeman sublevel by driving a $\Delta m = -1$ transition using the Zeeman laser for (a) or a $\Delta m = +1$ transition for (b). This reversal is facilitated by inserting or removing a half-wave plate to change the handedness of the Zeeman beam from right to left circularly polarized. The inset plot has been vertically stretched to better illustrate the less extreme Zeeman sublevels.

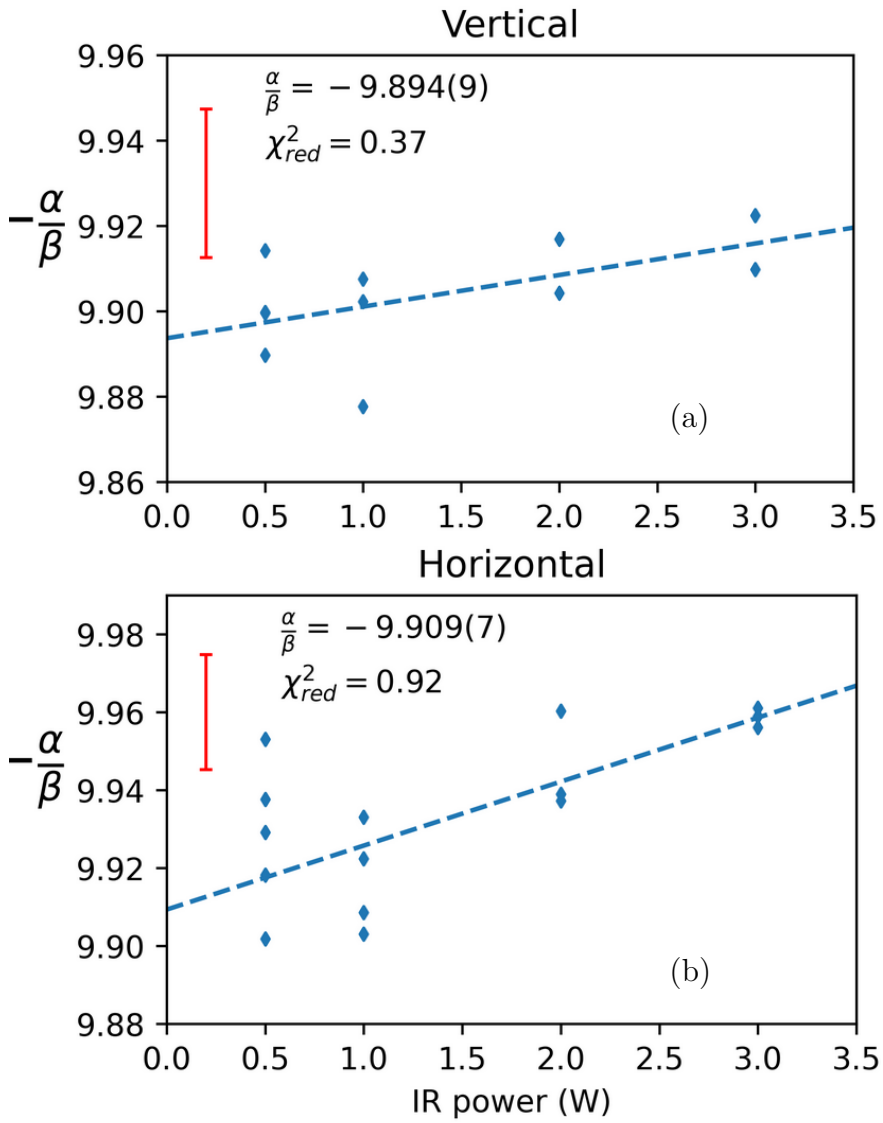

Figure 6.5. Ratio measurements plotted vs. the IR laser power exciting the two-photon transition. The ratios are fitted to a straight line to determine the zero intensity ratio. The red error bars in each plot show the average uncertainty of the measured ratios (blue diamonds). Plot (a) shows the fitted ratio when the polarization is vertical and (b) shows the fitted ratio when the polarization is horizontal.

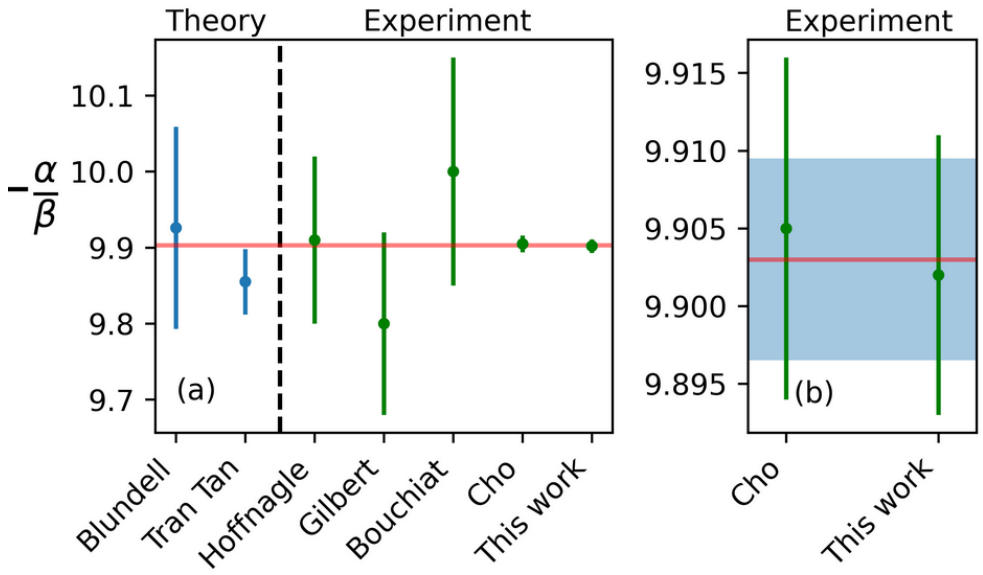

Figure 6.6. Previous theoretical (left, blue) [19, 31] and experimental (right, green) [45, 82, 83, 86] results of the ratio α/β. Theoretical results are a sum-over-states calculations of α and β. Plot (a) includes all previous results and plot (b) shows the two highest precision measurements on a finer scale. The pink horizontal line indicates the weighted average of the present result and that of Cho *et al.* [45], which we suggest as the recommended value, and the blue shaded region indicates the recommended uncertainty.

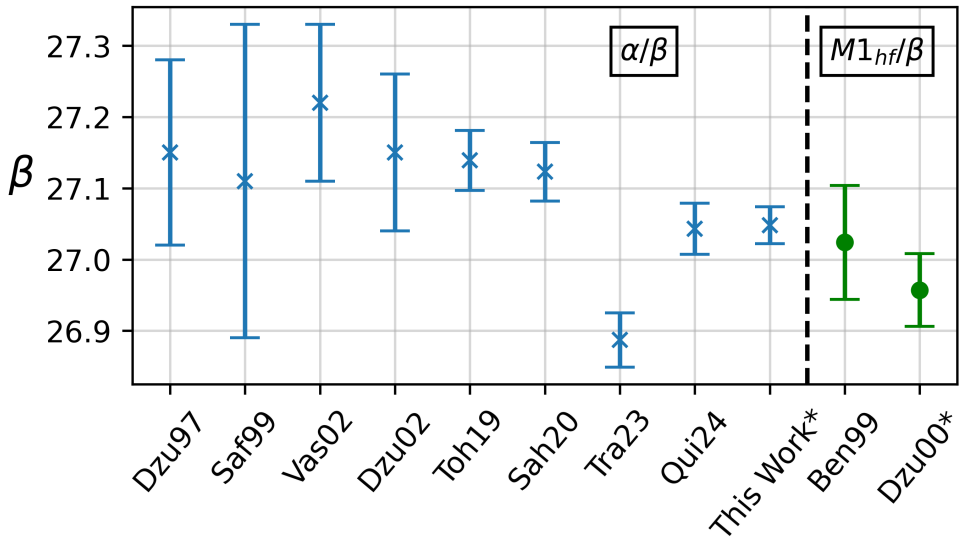

Figure 6.7. Illustrated here are previous determinations of β [19, 35, 54, 71, 72, 101, 103–105] using the sum-over-state calculation of α and a measured ratio of α/β (left, blue) and calculations of $M1_{hf}$ with a measured ratio of $M1_{hf}/\beta$ (right, green). These determinations are identified by the first three letters of the first author's name and the abbreviated publication year. The values to the left of 'This Work' use the Cho *et al.* [45] value for α/β. This result uses a weighted average of the Cho *et al.* value and the measured value in this work to determine β. The two values with an asterisk are the most precise determinations of β from each technique.

7. WORK TOWARDS A NEW PARITY VIOLATION MEASUREMENT

In this chapter we will give an overview of the expected PNC experimental technique and discuss the significant steps that have been taken towards a new measurement of E_{PNC}/β. Since 2018, we have constructed individual power build-up cavities for generating the necessary laser fields for M_1 reduction. We now have phase coherence between a two photon transition using unequal photons and a single photon transition. We have also constructed a field plate apparatus and a low noise switching circuit to bias these electrodes. We have also significantly reduced the building noise by fixing the optical table floating system and installing an additional vibration isolation damper on the turbo-molecular pump. There are a few steps still to complete. Some refinement of the electric field plates may be necessary after searching for systematic errors and we still need to construct the triple cavity system needed for the three coherent fields. Finally, some details of which laser, combination of lasers, or cavity will be locked to the 2-photon resonance. This last step will likely require some trial and error after the triple power build-up cavity apparatus is constructed.

7.1 Coherent light with three fields

This section will detail the technique that will be implemented to produce three coherent laser fields. Previously, the coherent control techniques utilized in the lab drove two-photon transitions where the photons were each half of the excited state energy and had the same polarization state [2–4]. This technique relied on an intense beam at the fundamental (two-photon) frequency to generate a second harmonic beam inside a nonlinear crystal and to drive the fairly weak two-photon transition. This technique is limited in that it can only drive $\Delta F = 0$ transitions. We propose an alternative technique to drive the two-photon transition with unequal photons, which would then permit $\Delta F = 0, \pm 1$ transitions. This technique is illustrated in Fig. 7.1.

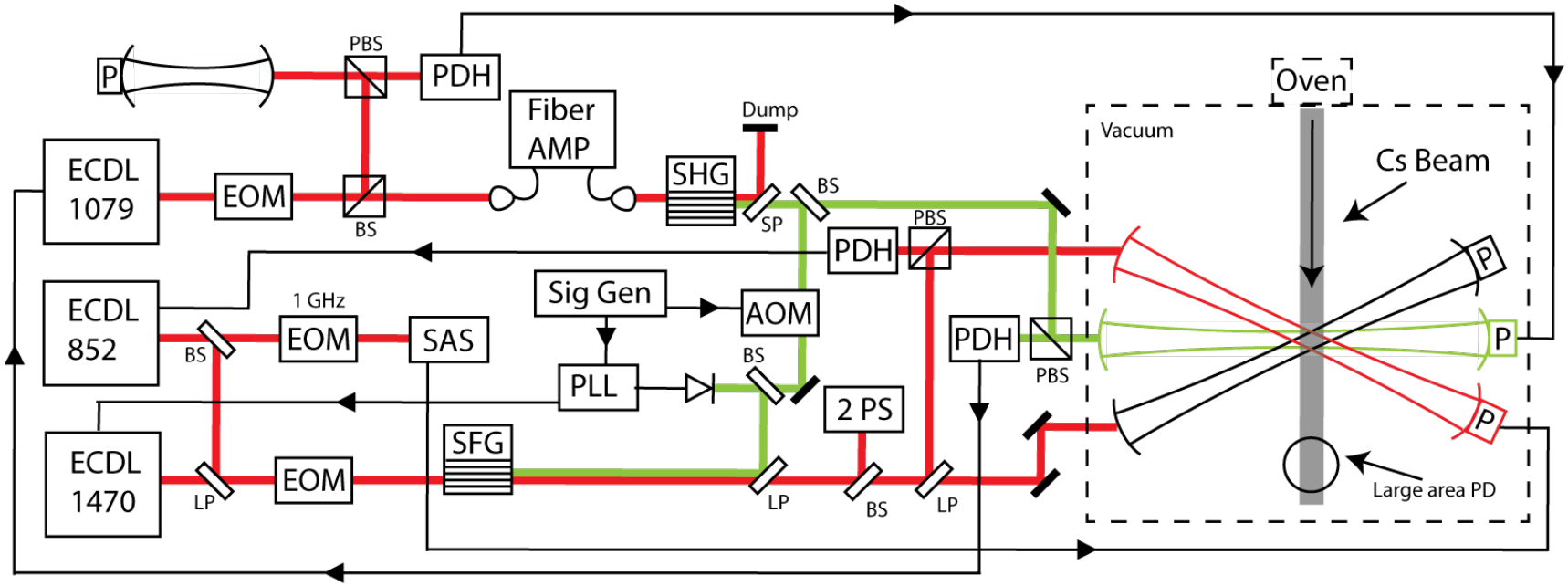

Figure 7.1. An illustration of the experimental configuration for the PNC experiment. Here we see an overview of the locking structure to stabilize the 540 nm, 852 nm, and 1470 nm beams to ensure overall stability and phase coherence. The following elements are labeled as; P - piezoelectric transducer, PD - photodetector, BS - beam splitter, SAS - saturated absorption spectroscopy cell, 2PS - two photon spectroscopy in a vapor cell, AOM acousto-optic modulator, PLL - phase-locked loop, PBS - polarizing beam splitter, LP - long pass filter, PDH - Pound-Drever-Hall, SFG - sum-frequency generation, SHG - second-harmonic generation, EOM - electro-optic modulator.

We present a method with which to stabilize three mutually coherent ECDLs to two Fabry-Perot cavities and an atomic transition. Our goals are coherence, absolute frequency stability, and high power.

We choose to drive the two-photon transition with 852 nm and 1470 nm beams. The 852 nm light will be red detuned from the D2 line in cesium by ∼1 GHz. We already have a resonant electro-optic phase modulator at 1 GHz, all of the necessary driving electronics, laser, and saturated absorption spectroscopy elements. The light at 1470 nm is currently being generated by a commercial ECDL which produces 50 mW of optical power. The 852 nm ECDL is a homemade Littrow type laser with ∼120 mW of optical power. Sum frequency generation is used to generate 200 μW of light at 540 nm with these two sources. This light is beat against a portion of the frequency doubled 540 nm light that has been frequency offset in an acousto-optic modulator (driving frequency 80 MHz). This AOM driving frequency is used as a reference in an OPLL to stabilize the beat note between the two 540 sources. The error signal from the OPLL is used to stabilize the 1470 nm light such that the sum frequency generated light and the frequency doubled light are phase coherent.

7.2 Power build-up cavity

The procedure we will implement to stabilize and amplify the light at 540 nm is as follows and is depicted in Fig. 7.1. We will amplify the light at 540 nm with a power build-up cavity (PBC) placed inside the vacuum chamber. The PBC will be atypical in that there will be no solid spacer between the mirrors to accommodate an atomic beam passing through the center. To amplify the interference signal, we aim for a large cavity finesse (50 to 70k) and a free spectral range of ∼500 MHz. This finesse will lead to an electric field build-up factor of 125 to 150, a critical amplification for observing the E_{PNC} interference. To stabilize light to such a narrow cavity resonance, a stable source at 1079 nm is necessary. We have purchased a commercial ECDL with a linewidth specification of 50 kHz and a fast commercial servo to stabilize the frequency. The frequency is stabilized and the linewidth is further narrowed using the Pound-Drever-Hall (PDH) technique. The 1079 nm source is stabilized such that the 540 nm light is resonant with the PBC. The PBC must be stabilized to the atomic

resonance. First, we stabilize this PBC to a second stable invar cavity by PDH. This second cavity is utilized due to the atypical nature of the high finesse cavity. Typically, high finesse cavities incorporate many techniques to increase stability that are not feasible with our geometric constraints. Without these features, our cavity transmission frequency will jump around due to tiny mirror vibrations. By stabilizing this high finesse cavity to a lower finesse cavity, these high frequency perturbations are dampened and produce a more stable lock to the atomic resonance. The lower finesse invar cavity is stabilized such that the 1079 nm light is resonant with the $6s \rightarrow 7s$ two-photon frequency. We currently detect this by double passing a portion of the amplified 1079 nm light through a heated vapor cell and collecting fluorescence with a photomultiplier tube. This configuration only allows $\Delta F = 0$ transitions and we must switch to an unequal two-photon transition for $\Delta F = \pm 1$ transitions. This is possible since the bandwidth of the phase lock is very high (1.2 MHz) and the bandwidth of the invar lock is quite low (<1 kHz).

Stray magnetic fields will allow M_1 transitions that interfere with the E_{PNC} and β transitions, with the same Δm. Since the M_1 transition is 20 000 times larger than E_{PNC}, we would need to cancel the stray fields in the interaction region to the 2×10^7 level to make a 0.1 % measurement. Luckily, M_1 transitions amplitudes are proportional to $(\vec{k} \times \epsilon)$ and a perfectly retroreflected beam would cancel this interaction. This perfect retroreflection is mostly realized by coupling the beams into a very high finesse optical cavity. Thus we choose to use intense standing waves for all three laser beams driving the $6s \rightarrow 7s$ transition to avoid excessively stringent stray magnetic field requirements. A simple cartoon of this geometry is illustrated in Fig. 7.2. We require that the 1470 nm and 852 nm beams be retroreflected as well since this is an interference measurement. Simply retroreflecting the 540 nm beams will not work since the phase matching condition, $\vec{k}_{852} + \vec{k}_{1470} - \vec{k}_{540} = 0$ is not met for the return beam. Here the double arrows in Fig. 7.2 indicate that the laser beams retroreflect back on themselves. The cesium beam would them traverse the three laser fields along the plane they generate. If the back reflector of each of these cavities has less than 100 ppm of loss, then the stray fields need to be canceled to better that one part in two-thousand. With a 10 G field, this equates to 5 mG. We are able to achieve such extinction ratios by observing the broadening of the Raman spectra in the absence of an applied magnetic field.

Mirrors with 100 ppm of loss are quite reasonable and even higher reflectivity mirrors would result in more relaxed magnetic field cancellation. Three cavities are a significant cost in terms of literal cost of mirror coatings, time spent stabilizing them, and physical size. Due to the slight wavefront mismatch of the three different cavities, the modulation signal will be reduced in size as the angle between the cavities is increased. See appendix B. This necessitates a tight geometry to minimize this effect.

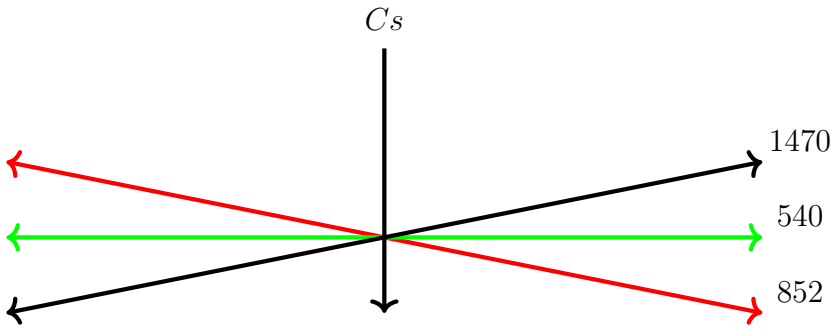

Figure 7.2. Simple geometry of the triple cavity

7.3 Procedure to measure E_{PNC}/β

To measure E_{PNC}/β, the PNC and vector Stark transition will be driven with a laser field resonant with the single photon $6s \rightarrow 7s$ transition at λ =540 nm. These transition amplitudes will be interfered with the two-photon transition amplitude that is driven by two other laser fields whose summed phase will be stabilized to the laser driving the single photon transitions, $\Phi(t) = \phi^{852} + \phi^{1470} - \phi^{540}$. We have shown that the three transitions amplitudes will beat against one another when this relative phase is varied and it is this technique with which we measure E_{PNC}/β.

There are multiple techniques to vary the optical phase. Previously, our lab has used a technique to interfere these weak transitions using a single intense beam and its second harmonic. This guarantees phase coherence. Then the beams were split in a Mach-Zehnder inferferometer where one of the beam paths was varied in length using a window mounted on a galvanometer. This limited the length and linearity of the scan. The limited scan requires the beat signal to be measured directly and fitted to a sine curve. The amplitudes of the sine

curve are then recorded. This procedure requires several fitting parameters and it is difficult to accurately determine the amplitude. A correction for the non-linearity of the scans is required as well. This procedure can be circumvented using better control of the driving field's phase. When phase locking three sources, we may drive the phase locking electronics with slightly varied frequencies. If we stabilize the 540 nm beam such that its frequency is 150 Hz away from the sum of 852 nm and 1470 nm frequencies, $\nu^{540} - \nu^{852} - \nu^{1470} \approx 150$ Hz, then the weak transitions will beat against the two-photon transition at 150 Hz and will not be limited in scan length or linearity. The primary benefit of this technique is that it allows direct measurement of the interference signal by using a lock-in amplifier. A lock-in amplifier can accurately mix down and filter the interference beat signal with the 150 Hz modulation from the phase locking electronics. This 150 Hz modulation is used as the lock-in reference and is easily derived by mixing a portion of each 80 MHz signal with a phase detector. These 80 MHz signals are used to offset a portion of the frequency doubled beam and to offset phase lock the sum-frequency and frequency doubled beams. Instead of fitting sine curves, the lock-in amplifier will measure and report the amplitude and phase of the interference signal relative to the 150 Hz phase modulation.

To form the measurement, we will prepare the atoms in the proper hyperfine and magnetic Zeeman sublevel as described in the optical pumping section. The atoms then interact with the three laser fields driving the $6s \rightarrow 7s$ transition. The Stark interaction requires a DC electric field to be applied. To drive the Stark transition, we will center a pair of electric field plates on the interaction region and vary the strength with an applied voltage. Atoms that interact with the three laser fields decay back down to either the $6s$ $F = 3$ or $6s$ $F = 4$ ground state. Atoms that decay into the opposite hypefine level than the one they were initially pumped are detected with a large area photo detector. This signal is amplified in a low-noise homemade transimpedance amplifier circuit. The output of this circuit is connected to a lock-in amplifier. As a reference to the lock-in amplifier, the two RF sources from the phase locking setup are mixed down in a phase detector. This allows demodulation at the beating frequency to determine the amplitude and phase relationship. The PNC interaction and the Stark vector polarizability are 90 degrees out of phase and the observed

combined interference varies in phase as the amplitude of the Stark transition is varied with the applied electric field.

Weak interaction measurements suffer from systematic errors due to stray fields. We reduce these by reversing electric and magnetic fields as well as initial m states to search for and reduce systematic errors. After minimizing systematic errors, the measurement proceeds by measuring the interference amplitude as a function of several different applied electric fields. Since the two weak amplitudes add out of phase, the applied electric field versus interference amplitude traces out a hyperbola whose vertex at zero electric field is only the E_{PNC} amplitude. Previously, our group has used this coherent control technique to measure the ratio of the magnetic dipole moment to the vector Stark polarizability, M_1/β [4]. Interference curves were measured by varying electric fields and a hyperbolic curve was traced out and fitted to determine the ratio M_1/β. This curve is plotted in Fig. 7.3. We will measure E_{PNC}/β using the same technique of varying the applied electric field to change the strength of the vector Stark polarizability and trace out a hyperbola to determine the ratio, E_{PNC}/β. To account for ac Stark effects, we will measure E_{PNC}/β at several different laser intensities to extrapolate back to zero laser intensity.

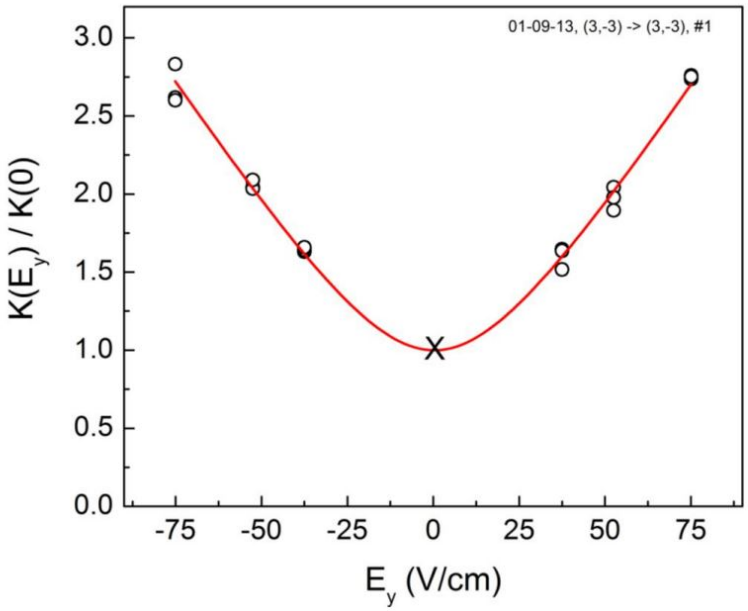

Figure 7.3. $M1/\beta$ interference fitting hyperbola. Image from [21]

7.4 Steps completed

7.4.1 Phase lock

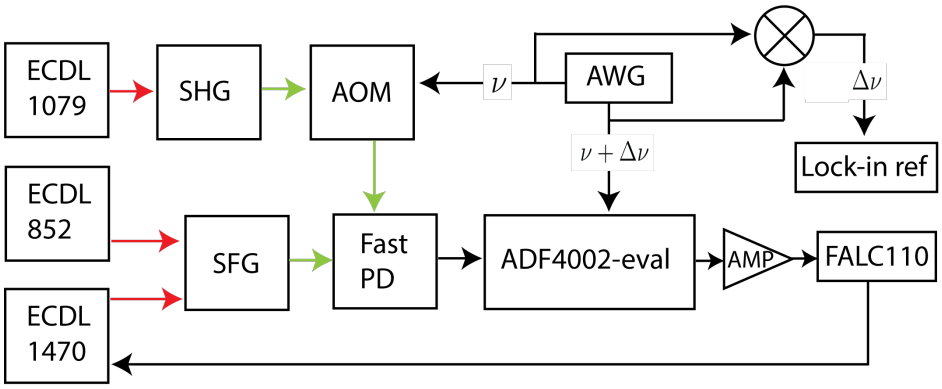

Figure 7.4. Technique for generating the beatnote between the two green beams (SFG and SHG). We use and ADF4002 evaluation board to compare phases and the feedback is sent to the 1470 nm laser.

The technique we use to phase lock the three lasers together is shown in Figure 7.4. Here we couple the SFG and SHG 540 nm beam into a polarization maintaining single mode optical fiber. This light is directed onto a 150 MHz Si photoreceiver (PDA10 - 10 kV/A). The beat signal output from the photoreceiver is directly fed into the ADF4002 evaluation board. We use a two channel arbitrary waveform generator with phase coherent output to generate a reference signal for the ADF4002. The other channel is used to offset the SHG 540 nm beam that is used for beating. This configuration allows an AOM to upshift the beam by 80 MHz and the optical phase lock loop to shift the beam back down 80 MHz. The output of the ADF4002 is a series of current pulses whose polarity indicates whether the reference or the signal is advanced in phase. These current pulses are integrated on a single pole loop filter that was simulated on ADIsimPLL software. The loop filter is unable to drive the low input impedance servo, so the output of this loop filter is the sent to a simple op-amp filter to buffer and slightly amplify the output to drive the FALC110 servo. The input impedance of the FACL110 is 50 Ω, so this op-amp buffer is critical. The FALC110 is used to servo the 1470 nm current to generate phase coherence between the SHG and SFG

beams. We have successfully stabilized these lasers using the analog (mixer) optical phase lock loop technique as well, but the preceding technique has been more robust.

Figure 7.5 shows the beat note between the SHG and SFG beams. A 20 db (1%) coupler is used to pick off a portion of the beat note to view with a spectrum analyzer. We see here an −80 dBc/Hz phase noise relative to the carrier near dc. We also see servo bumps at around 1.2 MHz, indicating the point at which the servo increases the noise of the laser system. Figure 7.6 shows a wide scan of the beat note between the SHG and SFG beams. This looks horrible and it is caused by the PDH modulation that is required for stabilizing the 852 nm (4 MHz) and 1079 nm (20 MHz) lasers to their optical cavities. We see all the intermodulation terms between the carriers and their sidebands. With the digital OPLL that we implement, the optical phase lock is insensitive to these extra peaks and does not add to the phase noise in the servo loop. Essentially, they look really bad but you wouldn't notice them without scanning wider to find them.

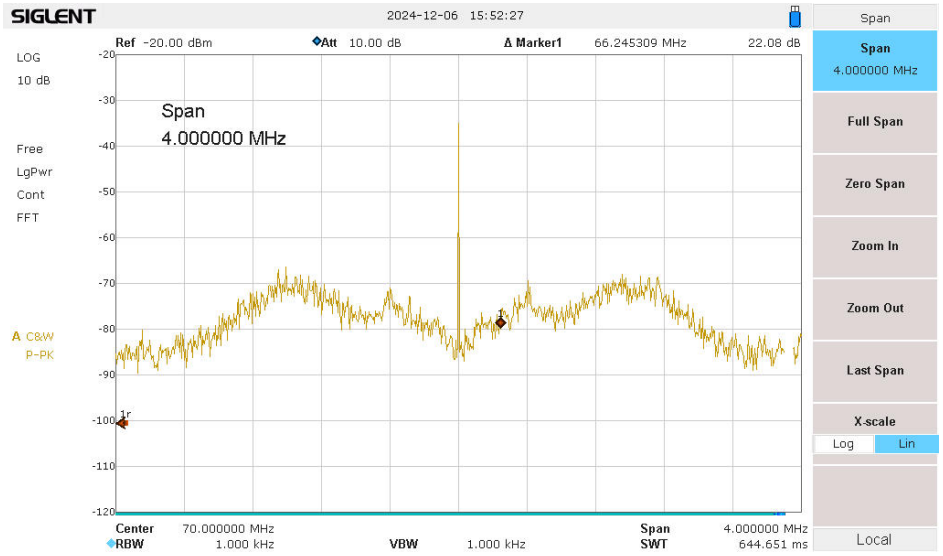

Figure 7.5. Beatnote between the SFG and SHG green beams. The trace shows the coherence between the two-photon transition (852 nm +1470 nm) and the single photon transition (540 nm). This coherence is critical for phase sensitive measurements.

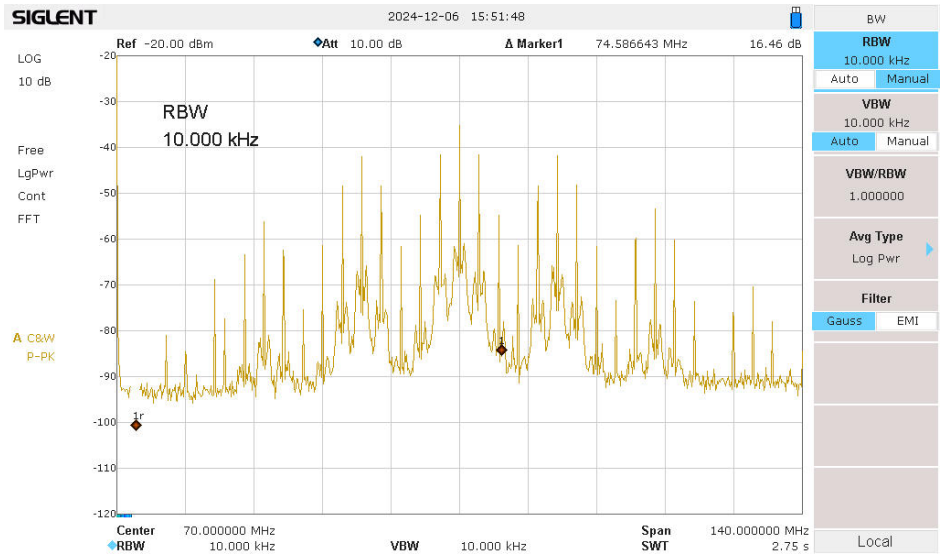

Figure 7.6. Beatnote between the SFG and SHG green beams. This spectra is a wide scan to show the

7.4.2 Cavity locks

We have gotten quite good at stabilizing lasers to high finesse cavities. We see linewidths well below 1 kHz after the power build-up cavity even with the cavity bouncing back and forth by several tens of MHz. We are able to lock the SHG beam to the power build-up cavity for the entire day without it coming unlocked. We use cavity ring-down spectroscopy to quantify the mirror reflectivity. If the input beam to a Fabry-Perot cavity with circulating power is suddenly switched off, the power in the cavity will exponentially decrease. This exponential decrease is dependent on the cavity finesse and mirror spacing. We use the formula

$$F = 2\pi \frac{c}{L} \tau_c, \tag{7.1}$$

from [108] to determine the finesse. Using an AOM to shutter the SHG beam, we record the power transmitting from the back side of the power build-up cavity. This exponential decay is fit and the decay constant and cavity length is then used to determine the finesse. An example ring-down measurement is shown in Figure 7.8. We measure finesse values in the range of 30k-50k. We believe the lower finesse values are due to contaminated mirror

surfaces such as mechanical pump oil. The mirror can be restored with a lot of cleaning wipes and patience.

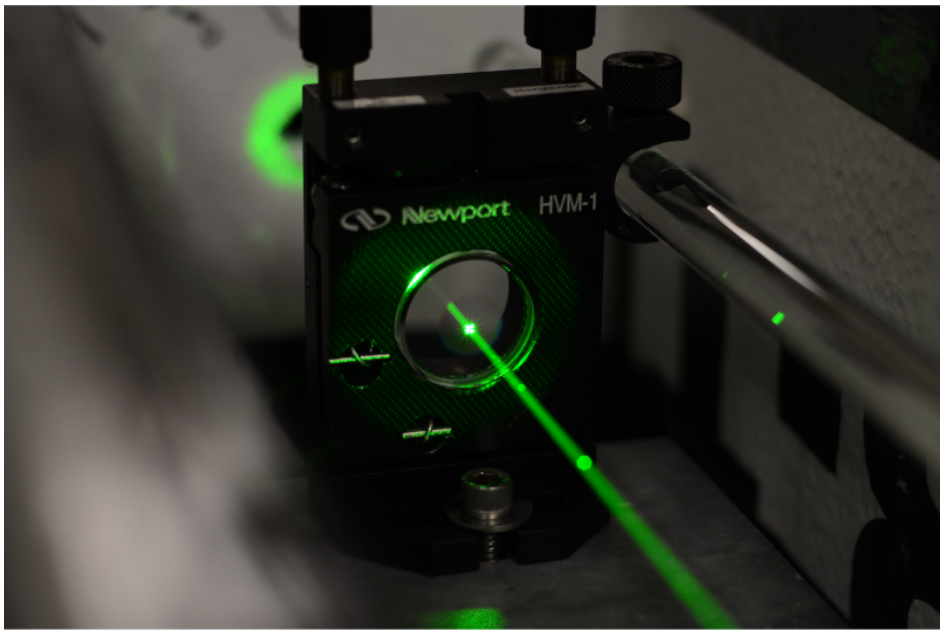

Figure 7.7. Here we see an image of the intense green beam stabilized to a high finesse Fabry-Perot cavity. A close look will reveal that the laser is stabilized to the (1,1) Hermite-Gaussian mode of the cavity. This is actually non-ideal since we want light in the (0,0) mode, but that makes a less interesting picture. Since the cavity is near flat-flat configuration, careful alignment is critical.

7.4.3 Two-photon locks

We plan to drive the $6s \rightarrow 7s$ transition and observe each hyperfine transition. This means that we cannot use the 1079 nm laser to stabilize the rest of the lasers via two-photon spectroscopy since it will not drive $\Delta F = \pm 1$ transitions. We must then use a portion of the 852 nm and 1470 nm beams for spectroscopy. Figure 7.9 shows an overview of this technique. We overlap the two IR beams and double pass them through a heated vapor cell and make sure to overlap the return beams well with the forward beams. When we observe fluorescence off to the side of the vapor cell while scanning one of the lasers, we see spectra like that of Figure 7.10. The blue trace is the fluorescence from the two-photon transition and the pink trace is the transmission of a 1 GHz free spectral range Fabry-Perot.

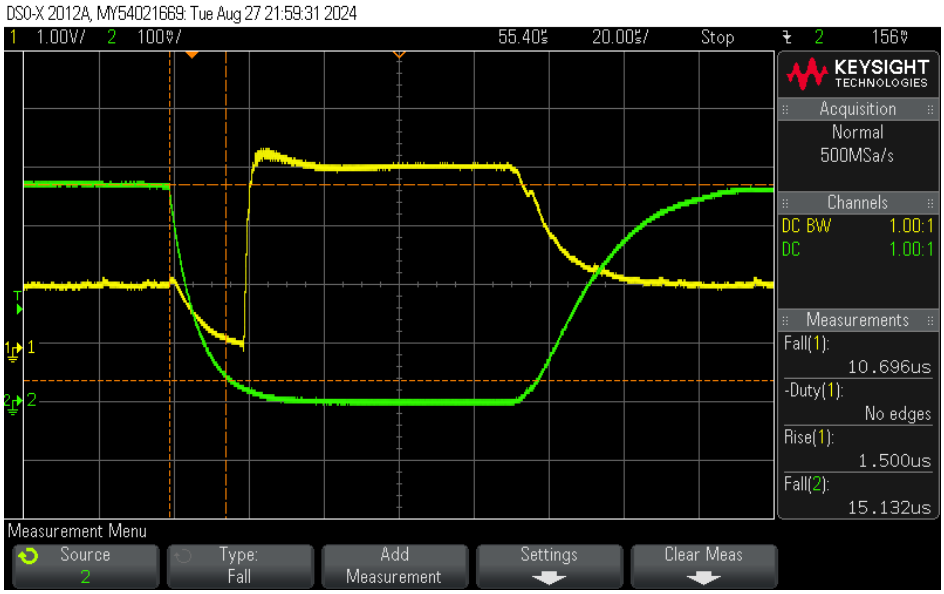

Figure 7.8. A measurement of the cavity ring down time for 540 nm power build-up cavity. The green trace shows the power transmitted through the power build-up cavity and the yellow trace shows the power reflected from the power build-up cavity. Here the frequency of the 1079 nm laser is stabilized to the cavity resonance and then is quickly turned off ($\approx$ 30 ns) using an acoustio-optic modulator. This light is turned back on after several μs to allow the servo to begin integrating the error signal to re-lock the laser. This process takes around 70 μs to start to re-lock. We fit the exponential decay of the yellow curve to extract the fall time of the circulating power in the cavity.

The slope in the baseline signal is due to scattered light from the intensity variation in the 852 nm beam. The slight peak asymmetry is due to having the retroreflected beam slightly tilted. We see large etalon effects from the cell otherwise. The dip in the center is caused by a similar process as saturated absorption spectroscopy. When on resonance, the forward and reverse beams interact with the same velocity group of atoms which reduces the overall fluorescence signal. Much like saturated absorption spectroscopy, we modulate one of the lasers (852 nm) at a low frequency and demodulate this signal to generate an error signal that we use to lock to this dip in the resonance.

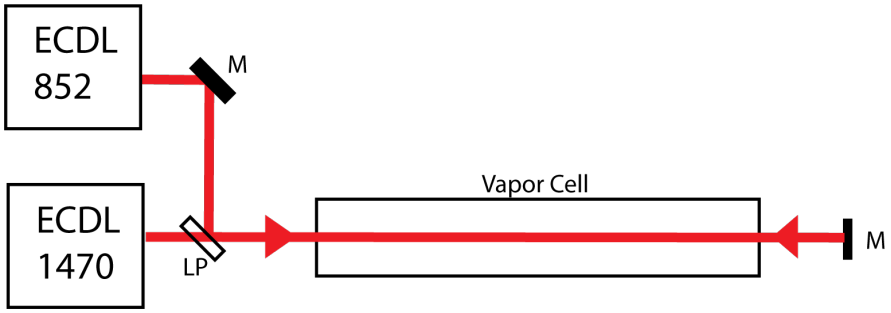

Figure 7.9. A simple image to illustrate the two-photon spectroscopy we will use to stabilize the three lasers to the $6s \rightarrow 7s$ transition.

7.4.4 Electric field generation

The electric field requirements for this measurement are quite stringent since we wish to apply fields on the order of 1.6 mV/cm. This requires precisely spaced plates and low noise voltage sources. The plates are constructed of 10 cm by 15 cm polished copper plates. Flatness of these plates is better than 12 µm over the plate surface. We space these plates by precision machined ceramic spacers whose length (4 cm) is known to ±12 µm. The spacers are tapped on the end for 8-32 thread. This allows the field plate to be assembled using nylon screws. An image of the field plates is shown in Figure 7.11 .

To generate the precision voltages, we designed the circuit shown in Figure 7.12. Here we generate three high precision voltages using extremely low noise (0.21 ppm_{RMS} from 10 Hz to 1 kHz) voltage references, LTC6655LN. These references come in two styles, a regular and a lower noise variant. The circuit is designed to accept both with a slight change in which components are populated. These voltages are then multiplexed to apply several different electric fields with both positive and negative polarity. The circuit takes either a signal from the computer or from physical switches on the front of the circuit case. A monitor pin has been included to measure the voltage across the plates using a floating digital multimeter such as a Keithley 2001. A voltage division circuit will be placed on the plates in the vacuum to lower the voltage down to the mV level required for the measurement. This will reduce noise injected onto the plates since the division will take place at the plates and not external

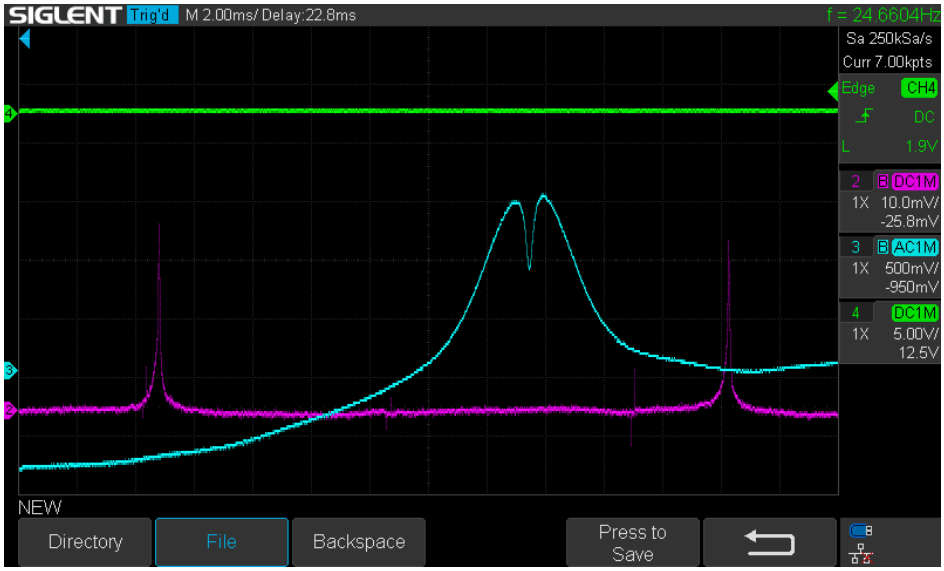

Figure 7.10. A measurement of the two-photon transition using two unequal photons in a vapor cell. The dip in the center is caused by a similar process as saturated absorption spectroscopy. When detuned from resonance, the forward and reverse pair of two-photon beams interact with different velocity groups in the vapor cell. When on resonance, the forward and reverse beams interact with the same velocity group which reduces the overall fluorescence signal.

to the vacuum chamber. The voltage division resistors are Caddock UFS-340 resistors with a $5ppm/°C$ temperature coefficient. Since the resistors will be coupled to the electric field plates, their ratio stability will be even better than $5ppm/°C$. This is already well below the measurement uncertainty. All we must do is measure the division ratio using two well calibrated digital multimeters. Then we can just monitor the applied field across the plates before the divider for the measurement.

7.4.5 Noise reduction

We have taken several steps to reduce the noise in the detection system. When stabilizing the 1079 nm lase to the power build-up cavity, the laser has a very large bandwidth and is easily able to keep up with the cavity. When trying to stabilize this cavity to the invar cavity or the atomic resonance, the power build-up cavity struggles to keep up due to the finite bandwidth of the cavity piezo. Mechanical vibration from the turbomolecular pump (800 Hz)

and from the ground causes noise on the power build of cavity to resonance lock. We have been working to minimize this mechanical noise coupling into the cavity by changing the cavity mount (now a Newport VIB100 isolator). We have also purchased and installed a new table leg. Due to the vacuum system weight, the table would not float on one corner. This new fifth leg passively damps vibration from the room and allows the entire table to float. We have also purchased a second vibration damper to place between the turbomolecular pump and the vacuum chamber. One manufacturer suggested that adding a second damper would increase damping by a 2.5 times.

7.5 Next steps

There are a few steps left for the E_{PNC}/β measurement. The three cavity configuration must be constructed and the entire laser system has to be stabilized to the atomic transition. The first step is hard and the second is not so difficult but must happen after the first. The triple cavity configuration is difficult due to size limitations and we will need some creative thinking in order to surpass this hurdle. Figure 7.13 shows the current state of locking and highlights what else is necessary to complete before the PNC measurement.

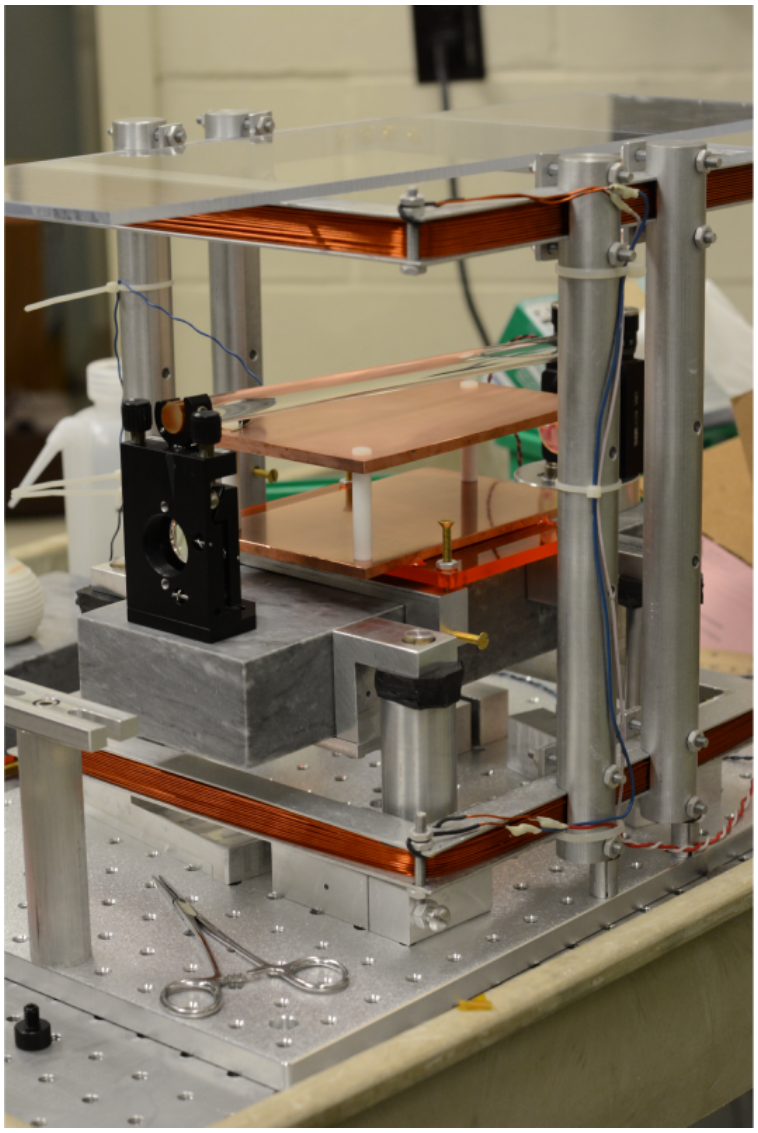

Figure 7.11. An image of the test power build-up cavity and electric field plates. The triple cavity apparatus for the PNC experiment will require three cavities that are overlapped on the atomic beam.

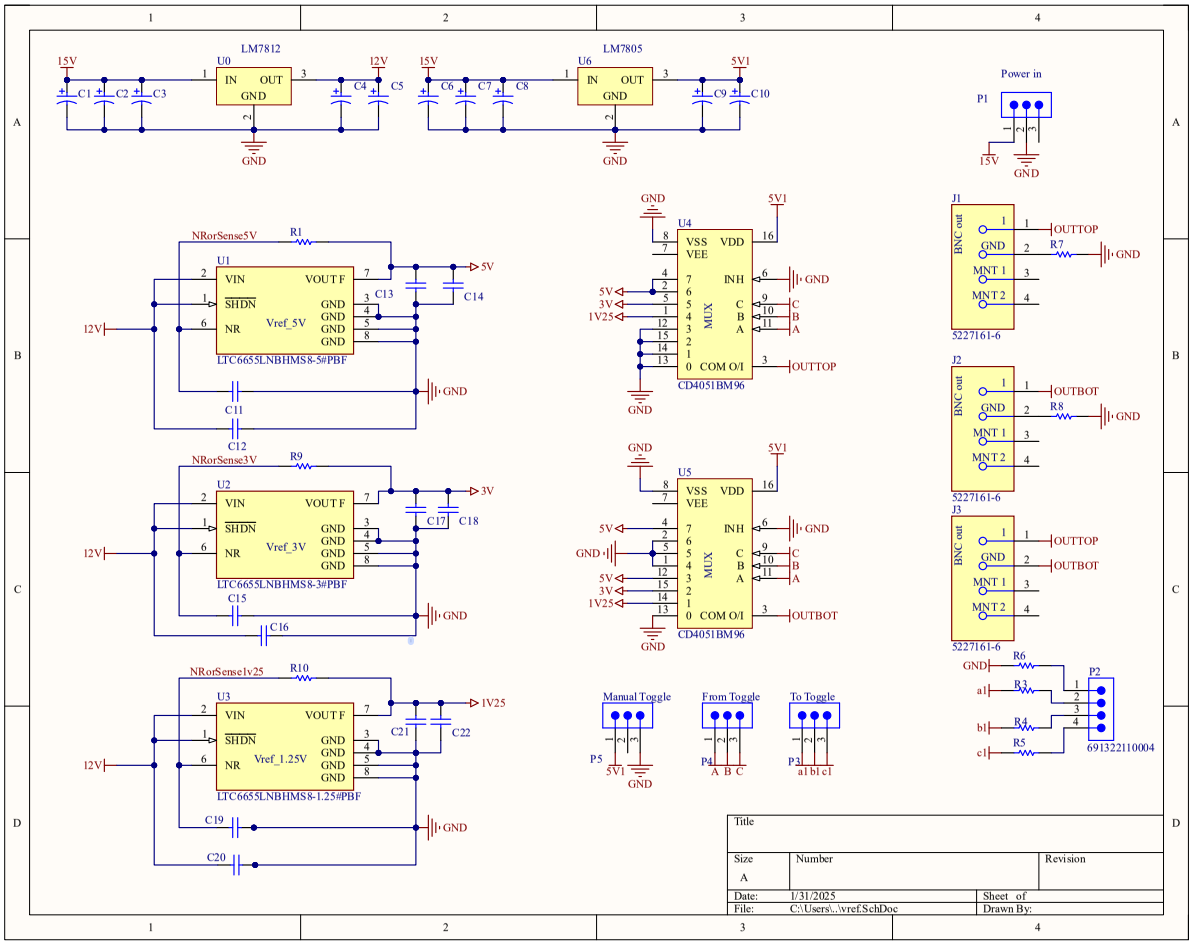

Figure 7.12. The PNC measurement requires a small low-noise electric field for interfering with the Stark vector polarizability, on the order of a few mV/cm. To apply these small fields, we have constructed a low voltage switching circuit to generate a stable low noise voltage (LTC6655LN voltage ref.) and to switch the electric field plate bias (CD4051BE multiplexer). This circuit allows fast and accurate switching of the electric field via a front panel or computer.

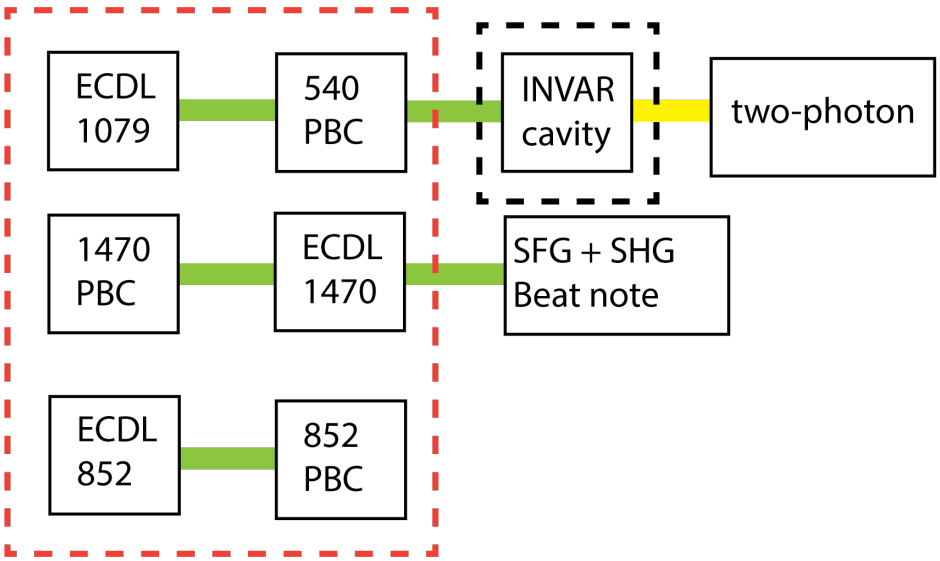

Figure 7.13. A high level diagram depicting the current state of locking. Items to the left are being locked to the right and the green color indicates a successful stable lock. The yellow lock is works for the two-photon transition for two equal photons, but must still be completed for unequal photons. The red box indicates that these three green locks have been completed for the triple cavity configuration. The black box is a lock that may be unnecessary if the PBC can be locked directly to the two-photon resonance.

8. SUMMARY

8.1 Contribution to atomic parity violation

In this thesis we have shown an improved measurement of the ratio α/β as well as an improved measurement of α_{7s}. This second measurement, along with improved atomic theory [19, 75], allowed us to calculate an improved value for α. We combine this new value of α with our new ratio of α/β to attain a more precise value for $\beta = 27.048\ (26)\ a_0^3$. This value has a 40% smaller uncertainty than the previous best determination [22]. This is due to reducing the uncertainty of α/β by about half and the uncertainty of α by 30%. This new value for β is a critical component in the determination of the weak charge of the cesium nucleus, see equation 8.1.

$$Q_w = k_{PV}\ \frac{\mathrm{Im}(E_{PNC})}{\beta}\ \frac{\beta}{\alpha}\ \alpha \tag{8.1}$$

With this updated value for β, we can recalculate Q_w. Using our new suggested value for $\beta = 27.048\ (26)\ a_0^3$ and the Wood measurement of $\mathrm{Im}(E_{PNC})/\beta = -1.5935\ (56)\ mV/cm$ [1], we get $\mathrm{Im}(E_{PNC}) = 0.8382\ (31) \times 10^{-11}\ |\mathrm{e}|a_0$. This value must be combined with an atomic theory value for k_{pv}. There are two high precision determinations that disagree with one another. Porsev *et al.* [109, 110] determined

$$\mathrm{Im}(E_{PNC}) = 0.8906\ (24) \times 10^{-11}\ |\mathrm{e}|a_0\,(-Q_w/N)\,. \tag{8.2}$$

Here N is the number of neutrons in the nucleus and a_0 is the Bohr radius. With this value for k_{pv} we get $Q_w = -73.41(27)_{expt}(20)_{theo}$. Dzuba *et al.* [111, 112] determined

$$\mathrm{Im}(E_{PNC}) = 0.8977\ (40) \times 10^{-11}\ |\mathrm{e}|a_0\,(-Q_w/N)\,. \tag{8.3}$$

When we combine this value with our new determination of $\mathrm{Im}(E_{PNC})$, we get $Q_w = -72.83(27)_{expt}(32)_{theo}$. A summary of these results and past results are illustrated in Figure 8.1. There have been enough determinations of Q_w using the results of Wood *et al.* [1] to give researchers whiplash and it is for this reason we have not published a new value for Q_w in

our article on α/β or in our Stark shift letter. Really what is needed is a new determination of E_{PNC}/β and a more precise value for k_{pv}. We are working quickly towards the former and Andrei Derevianko at University of Nevada, Reno is working towards the latter. We hope to attain 0.1% uncertainty in E_{PNC}/β and Derevianko believes 0.2% is attainable for k_{pv}. These two contributions would be a huge step forwards for atomic parity violation and could elucidate new physics.

In addition to the work that directly affects the value of Q_w, we have also produced high precision measurements of hyperfine spacings on the $8p_{1/2}$, $8p_{3/2}$, $12s_{1/2}$, $13s_{1/2}$, $11d_{3/2}$, and $11d_{5/2}$ levels. The $ns_{1/2}$ and $np_{1/2}$ levels are of particular interest to atomic theorist who aim to calculate k_{pv}.

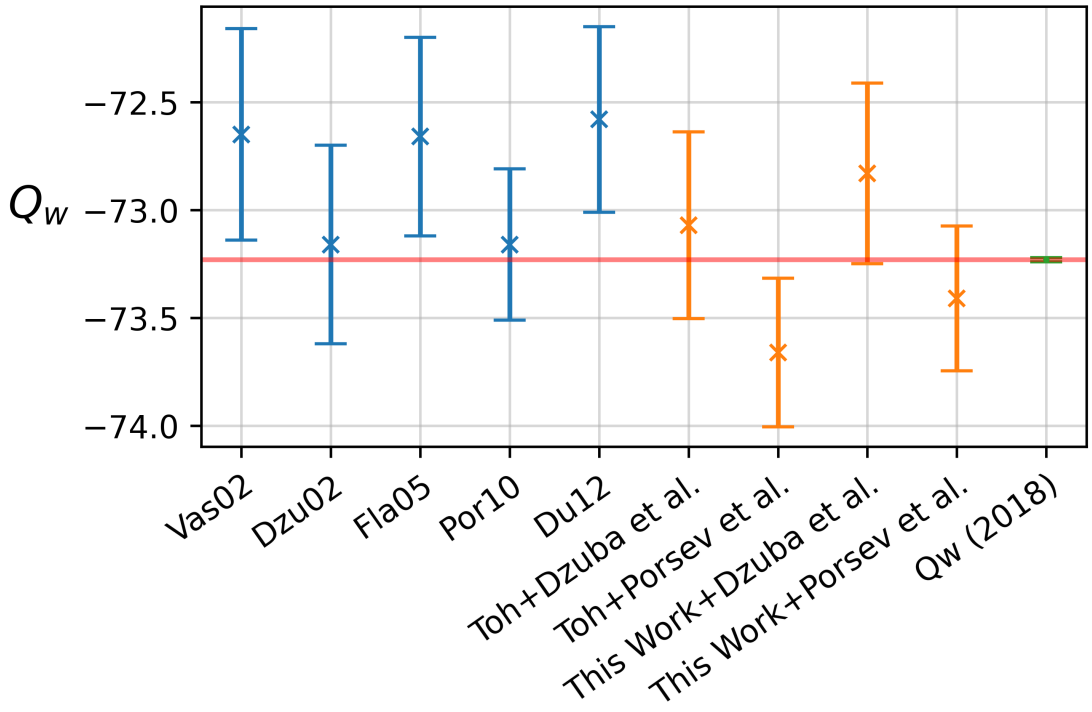

Figure 8.1. A summary of past results for Q_w of the cesium nucleus. Each determination uses a calculated value for k_{pv} and the measurement of E_{PNC}/β [103, 104, 109–113]. The first three letters and the publication year indication the work cited. The orange results use the sum-over-states calculation of α to determine β and the two most precise values for k_{pv}. The last value (green) is the standard model prediction [25].

REFERENCES

[1] C. S. Wood *et al.*, "Measurement of parity nonconservation and an anapole moment in cesium," *Science*, vol. 275, no. 5307, pp. 1759–1763, 1997, ISSN: 0036-8075. DOI: 10.1126/science.275.5307.1759. [Online]. Available: http://science.sciencemag.org/content/275/5307/1759.

[2] M. Gunawardena and D. S. Elliott, "Atomic homodyne detection of weak atomic transitions," *Phys. Rev. Lett.*, vol. 98, p. 043 001, 4 Jan. 2007. DOI: 10.1103/PhysRevLett.98.043001. [Online]. Available: https://link.aps.org/doi/10.1103/PhysRevLett.98.043001.

[3] M. Gunawardena and D. S. Elliott, "Weak signal detection using coherent control," *Phys. Rev. A*, vol. 76, p. 033 412, 3 Sep. 2007. DOI: 10.1103/PhysRevA.76.033412. [Online]. Available: https://link.aps.org/doi/10.1103/PhysRevA.76.033412.

[4] D. Antypas and D. S. Elliott, "Measurement of a weak transition moment using two-pathway coherent control," *Phys. Rev. A*, vol. 87, p. 042 505, 4 Apr. 2013. DOI: 10.1103/PhysRevA.87.042505. [Online]. Available: https://link.aps.org/doi/10.1103/PhysRevA.87.042505.

[5] J. A. Quirk, C. E. Tanner, and D. S. Elliott, "Measurement of the ratio of the scalar polarizability to the vector polarizability for the $6s\,^2S_{1/2} \rightarrow 7s\,^2S_{1/2}$ transition in cesium," *Phys. Rev. A*, vol. 109, p. 062 809, 6 Jun. 2024. DOI: 10.1103/PhysRevA.109.062809. [Online]. Available: https://link.aps.org/doi/10.1103/PhysRevA.109.062809.

[6] T. D. Lee and C. N. Yang, "Question of parity conservation in weak interactions," *Phys. Rev.*, vol. 104, pp. 254–258, 1 Oct. 1956. DOI: 10.1103/PhysRev.104.254. [Online]. Available: https://link.aps.org/doi/10.1103/PhysRev.104.254.

[7] C. S. Wu, E. Ambler, R. W. Hayward, D. D. Hoppes, and R. P. Hudson, "Experimental test of parity conservation in beta decay," *Phys. Rev.*, vol. 105, pp. 1413–1415, 4 Feb. 1957. DOI: 10.1103/PhysRev.105.1413. [Online]. Available: https://link.aps.org/doi/10.1103/PhysRev.105.1413.

[8] M. J. D. Macpherson, K. P. Zetie, R. B. Warrington, D. N. Stacey, and J. P. Hoare, "Precise measurement of parity nonconserving optical rotation at 876 nm in atomic bismuth," *Phys. Rev. Lett.*, vol. 67, pp. 2784–2787, 20 Nov. 1991. DOI: 10.1103/PhysRevLett.67.2784. [Online]. Available: https://link.aps.org/doi/10.1103/PhysRevLett.67.2784.

[9] D. M. Meekhof, P. A. Vetter, P. K. Majumder, S. K. Lamoreaux, and E. N. Fortson, "Optical-rotation technique used for a high-precision measurement of parity nonconservation in atomic lead," *Phys. Rev. A*, vol. 52, pp. 1895–1908, 3 Sep. 1995. DOI: 10.1103/PhysRevA.52.1895. [Online]. Available: https://link.aps.org/doi/10.1103/PhysRevA.52.1895.

[10] N. H. Edwards, S. J. Phipp, P. E. G. Baird, and S. Nakayama, "Precise measurement of parity nonconserving optical rotation in atomic thallium," *Phys. Rev. Lett.*, vol. 74, pp. 2654–2657, 14 Apr. 1995. DOI: 10.1103/PhysRevLett.74.2654. [Online]. Available: https://link.aps.org/doi/10.1103/PhysRevLett.74.2654.

[11] D. Antypas, A. Fabricant, J. E. Stalnaker, K. Tsigutkin, V. V. Flambaum, and D. Budker, "Isotopic variation of parity violation in atomic ytterbium," *Nature Physics*, vol. 15, no. 2, pp. 120–123, 2018. DOI: 10.1038/s41567-018-0312-8.

[12] M. S. Safronova, D. Budker, D. DeMille, D. F. J. Kimball, A. Derevianko, and C. W. Clark, "Search for new physics with atoms and molecules," *Rev. Mod. Phys.*, vol. 90, p. 025 008, 2 Jun. 2018. DOI: 10.1103/RevModPhys.90.025008. [Online]. Available: https://link.aps.org/doi/10.1103/RevModPhys.90.025008.

[13] M. A. Bouchiat and C. Bouchiat, "I. parity violation induced by weak neutral currents in atomic physics," *Journal de Physique*, vol. 35, no. 12, pp. 899–927, 1974. DOI: 10.1051/jphys:019740035012089900.

[14] M. A. Bouchiat and C. Bouchiat, "Parity violation induced by weak neutral currents in atomic physics. part ii," *Journal de Physique*, vol. 36, no. 6, pp. 493–509, 1975. DOI: 10.1051/jphys:01975003606049300.

[15] S. Nanos, I. Papigkiotis, and D. Antypas, "Studies of parity violation in atoms," *Annalen der Physik*, Nov. 2024, ISSN: 1521-3889. DOI: 10.1002/andp.202400261. [Online]. Available: http://dx.doi.org/10.1002/andp.202400261.

[16] M. R. Kalita *et al.*, "Isotope shifts in the $7s \rightarrow 8s$ transition of francium: Measurements and comparison to ab initio theory," *Phys. Rev. A*, vol. 97, p. 042 507, 4 Apr. 2018. DOI: 10.1103/PhysRevA.97.042507. [Online]. Available: https://link.aps.org/doi/10.1103/PhysRevA.97.042507.

[17] H. B. Tran Tan, D. Xiao, and A. Derevianko, "Parity-mixed coupled-cluster formalism for computing parity-violating amplitudes," *Phys. Rev. A*, vol. 105, p. 022 803, 2 Feb. 2022. DOI: 10.1103/PhysRevA.105.022803. [Online]. Available: https://link.aps.org/doi/10.1103/PhysRevA.105.022803.

[18] H. B. Tran Tan and A. Derevianko, "Precision theoretical determination of electric-dipole matrix elements in atomic cesium," *Phys. Rev. A*, vol. 107, p. 042 809, 4 Apr. 2023. DOI: 10.1103/PhysRevA.107.042809. [Online]. Available: https://link.aps.org/doi/10.1103/PhysRevA.107.042809.

[19] H. B. T. Tan, D. Xiao, and A. Derevianko, *Reevaluation of Stark-induced transition polarizabilities in cesium*, 2023. arXiv: 2306.09573 [physics.atom-ph].

[20] C. Wood, "High precision atomic parity non-conservation measurement using a spin polarized cesium beam and the nuclear anapole moment of ^{133}Cs," Ph.D. dissertation, 1996.

[21] D. Antypas, "Measurement of a weak transition moment using coherent control," Ph.D. dissertation, 2013.

[22] T. Yao De George, "Progress towards a new parity non-conservation measurement in cesium-133," Ph.D. dissertation, 2019.

[23] G. Yang, J. Wang, B. Yang, and J. Wang, "Determination of the hyperfine coupling constant of the cesium $7S_{1/2}$ state," *Laser Physics Letters*, vol. 13, no. 8, p. 085 702, 2016. [Online]. Available: http://stacks.iop.org/1612-202X/13/i=8/a=085702.

[24] K.-H. Weber and C. J. Sansonetti, "Accurate energies of ns, np, nd, nf, and ng levels of neutral cesium," *Phys. Rev. A*, vol. 35, pp. 4650–4660, 11 Jun. 1987. DOI: 10.1103/PhysRevA.35.4650. [Online]. Available: https://link.aps.org/doi/10.1103/PhysRevA.35.4650.

[25] M. Tanabashi *et al.*, "Review of particle physics," *Phys. Rev. D*, vol. 98, p. 030 001, 3 Aug. 2018. DOI: 10.1103/PhysRevD.98.030001. [Online]. Available: https://link.aps.org/doi/10.1103/PhysRevD.98.030001.

[26] M. S. Safronova, D. Budker, D. DeMille, D. F. J. Kimball, A. Derevianko, and C. W. Clark, "Search for New Physics with Atoms and Molecules," *Rev. Mod. Phys*, vol. 90, p. 025 008, 2018.

[27] W. R. Johnson, M. S. Safronova, and U. I. Safronova, "Combined effect of coherent z exchange and the hyperfine interaction in the atomic parity-nonconserving interaction," *Phys. Rev. A*, vol. 67, p. 062 106, 6 Jun. 2003. DOI: 10.1103/PhysRevA.67.062106. [Online]. Available: https://link.aps.org/doi/10.1103/PhysRevA.67.062106.

[28] W. C. Haxton and C. E. Wieman, "Atomic Parity Nonconservation and Nuclear Anapole Moments," *Annual Review of Nuclear and Particle Science*, vol. 51, pp. 261–293, 2001. DOI: 10.1146/annurev.nucl.51.101701.132458. eprint: nucl-th/0104026.

[29] B. Desplanques, J. F. Donoghue, and B. R. Holstein, "Unified treatment of the parity violating nuclear force," *Annals of Physics*, vol. 124, no. 2, pp. 449–495, 1980, ISSN: 0003-4916. DOI: https://doi.org/10.1016/0003-4916(80)90217-1. [Online]. Available: https://www.sciencedirect.com/science/article/pii/0003491680902171.

[30] S. L. Gilbert and C. E. Wieman, "Atomic-beam measurement of parity nonconservation in cesium," *Phys. Rev. A*, vol. 34, pp. 792–803, 2 Aug. 1986. DOI: 10.1103/PhysRevA.34.792. [Online]. Available: https://link.aps.org/doi/10.1103/PhysRevA.34.792.

[31] S. A. Blundell, J. Sapirstein, and W. R. Johnson, "High-accuracy calculation of parity nonconservation in cesium and implications for particle physics," *Phys. Rev. D*, vol. 45, pp. 1602–1623, 5 Mar. 1992. DOI: 10.1103/PhysRevD.45.1602. [Online]. Available: https://link.aps.org/doi/10.1103/PhysRevD.45.1602.

[32] C. Bouchiat and C. Piketty, "Magnetic dipole and electric quadrupole amplitudes induced by the hyperfine interaction in the cesium 6*s*-7*s* transition and the parity violation calibration," *Journal de Physique*, vol. 49, pp. 1851–1856, 1988. DOI: https://doi.org/10.1051/jphys:0198800490110185100. [Online]. Available: https://jphys.journaldephysique.org/en/articles/jphys/abs/1988/11/jphys_1988___49_11_1851_0/jphys_1988___49_11_1851_0.html.

[33] B. Stephen, Ph.D. dissertation, University of Colorado, 1998.

[34] M.-A. Bouchiat and J. Guéna, "The E2 6S-7S amplitude in Cesium and its importance in a precise calibration of Epv," *Journal de Physique*, vol. 49, no. 12, pp. 2037–2044, 1988. DOI: 10.1051/jphys:0198800490120203700. [Online]. Available: https://hal.science/jpa-00210884.

[35] S. C. Bennett and C. E. Wieman, "Measurement of the 6s 7s Transition Polarizability in Atomic Cesium and an Improved Test of the Standard Model," *Physical Review Letters*, vol. 82, no. 12, pp. 2484–2487, Mar. 1999. DOI: 10.1103/PhysRevLett.82.2484. [Online]. Available: http://link.aps.org/doi/10.1103/PhysRevLett.82.2484.

[36] S. L. Gilbert, B. P. Masterson, M. C. Noecker, and C. E. Wieman, "Precision measurement of the off-diagonal hyperfine interaction," *Phys. Rev. A*, vol. 34, pp. 3509–3512, 4 Oct. 1986. DOI: 10.1103/PhysRevA.34.3509. [Online]. Available: https://link.aps.org/doi/10.1103/PhysRevA.34.3509.

[37] R. Pires, M. Ascoli, E. E. Eyler, P. L. Gould, and A. Derevianko, "Upper limit on the magnetic dipole contribution to the $5p-8p$ transition in Rb by use of ultracold atom spectroscopy," *Phys. Rev. A*, vol. 80, p. 062 502, 6 Dec. 2009. DOI: 10.1103/PhysRevA.80.062502. [Online]. Available: https://link.aps.org/doi/10.1103/PhysRevA.80.062502.

[38] C. E. Wieman and L. Hollberg, "Using diode lasers for atomic physics," *Review of Scientific Instruments*, vol. 62, no. 1, pp. 1–20, 1991. DOI: 10.1063/1.1142305. eprint: https://doi.org/10.1063/1.1142305. [Online]. Available: https://doi.org/10.1063/1.1142305.

[39] K. G. Libbrecht and J. L. Hall, "A low-noise high-speed diode laser current controller," *Review of Scientific Instruments*, vol. 64, no. 8, pp. 2133–2135, 1993. DOI: 10.1063/1.1143949.

[40] C. M. Seck, P. J. Martin, E. C. Cook, B. C. Odom, and D. A. Steck, "Noise reduction of a Libbrecht–Hall style current driver," *Review of Scientific Instruments*, vol. 87, no. 6, p. 064 703, 2016. DOI: 10.1063/1.4953330.

[41] D. L. Troxel, C. J. Erickson, and D. S. Durfee, "Note: Updates to an ultra-low noise laser current driver," *Review of Scientific Instruments*, vol. 82, no. 9, p. 096 101, 2011. DOI: 10.1063/1.3630950.

[42] C. Erickson, M. Van Zijll, G. Doermann, and D. Durfee, *An ultrahigh stability, low-noise laser current driver with digital control*, Jul. 2008. [Online]. Available: https://pubmed.ncbi.nlm.nih.gov/18681691/.

[43] D. Wolfgang, *Laser Spectroscopy: BASIC concepts and instrumentation: 2nd corrected printing*. Springer-Verlag, 1996.

[44] E. D. Black, "An introduction to Pound–Drever–Hall laser frequency stabilization," *American Journal of Physics*, vol. 69, no. 1, pp. 79–87, 2001. DOI: 10.1119/1.1286663.

[45] D. Cho, C. S. Wood, S. C. Bennett, J. L. Roberts, and C. E. Wieman, "Precision measurement of the ratio of scalar to tensor transition polarizabilities for the cesium 6s-7s transition," *Phys. Rev. A*, vol. 55, pp. 1007–1011, 2 Feb. 1997. DOI: 10.1103/PhysRevA.55.1007. [Online]. Available: https://link.aps.org/doi/10.1103/PhysRevA.55.1007.

[46] J. S. M. Ginges and A. V. Volotka, "Testing atomic wave functions in the nuclear vicinity: The hyperfine structure with empirically deduced nuclear and quantum electrodynamic effects," *Phys. Rev. A*, vol. 98, p. 032 504, 3 Sep. 2018. DOI: 10.1103/PhysRevA.98.032504. [Online]. Available: https://link.aps.org/doi/10.1103/PhysRevA.98.032504.

[47] V. Gerginov, A. Derevianko, and C. E. Tanner, "Observation of the nuclear magnetic octupole moment of ^{133}Cs," *Physical Review Letters*, vol. 91, no. 7, p. 072 501, 2003.

[48] A. Corney, *Atomic and Laser Spectroscopy*. Clarendon Press Oxford, 1978.

[49] M. Safronova. "Portal for high precision atomic data and computation." (2021), [Online]. Available: https://www1.udel.edu/atom/index.html.

[50] S. J. Grunefeld, B. M. Roberts, and J. S. M. Ginges, "Correlation trends in the hyperfine structure for Rb, Cs, and Fr, and high-accuracy predictions for hyperfine constants," *Phys. Rev. A*, vol. 100, no. 4, p. 042 506, 2019. DOI: 10.1103/PhysRevA.100.042506. [Online]. Available: https://link.aps.org/doi/10.1103/PhysRevA.100.042506.

[51] C. Tai, R. Gupta, and W. Happer, "Hyperfine structure of the $8^2P_{1/2}$ state of Cs^{133}," *Physical Review A*, vol. 8, no. 4, p. 1661, 1973.

[52] F. Cataliotti, C. Fort, F. Pavone, and M. Inguscio, "Doppler-free excitation of the weak $6S_{1/2} \rightarrow 8P_{1/2}$ cesium transition at 389 nm," *Zeitschrift für Physik D Atoms, Molecules and Clusters*, vol. 38, no. 1, pp. 31–33, 1996.

[53] Y.-W. Liu and P. Baird, "Measurement of the caesium $6S_{1/2} \rightarrow 8P_{1/2}$ transition frequency," *Applied Physics B*, vol. 71, no. 1, pp. 567–572, 2000.

[54] M. S. Safronova, W. R. Johnson, and A. Derevianko, "Relativistic many-body calculations of energy levels, hyperfine constants, electric-dipole matrix elements, and static polarizabilities for alkali-metal atoms," *Phys. Rev. A*, vol. 60, pp. 4476–4487, 6 Dec. 1999. DOI: 10.1103/PhysRevA.60.4476. [Online]. Available: https://link.aps.org/doi/10.1103/PhysRevA.60.4476.

[55] Y.-B. Tang, B.-Q. Lou, and T.-Y. Shi, "Ab initio studies of electron correlation effects in magnetic dipolar hyperfine interaction of Cs," *Journal of Physics B: Atomic, Molecular and Optical Physics*, vol. 52, no. 5, p. 055 002, 2019. [Online]. Available: https://doi.org/10.1088/1361-6455/ab013c.

[56] B. K. Sahoo, B. P. Das, and H. Spiesberger, "New physics constraints from atomic parity violation in Cs 133," *Physical Review D*, vol. 103, no. 11, p. L111303, 2021.

[57] V. Gerginov, C. E. Tanner, S. A. Diddams, A. Bartels, and L. Hollberg, "High-resolution spectroscopy with a femtosecond laser frequency comb," *Opt. Lett.*, vol. 30, no. 13, pp. 1734–1736, Jul. 2005. DOI: 10.1364/OL.30.001734. [Online]. Available: http://opg.optica.org/ol/abstract.cfm?URI=ol-30-13-1734.

[58] V. Gerginov and C. E. Tanner, "Fluorescence of a highly collimated atomic cesium beam: Theory and experiment," *Optics Communications*, vol. 222, no. 1, pp. 17–28, 2003, ISSN: 0030-4018. DOI: https://doi.org/10.1016/S0030-4018(03)01505-0. [Online]. Available: https://www.sciencedirect.com/science/article/pii/S0030401803015050.

[59] J. A. Quirk, L. Sherman, A. Damitz, C. E. Tanner, and D. S. Elliott, "Measurement of the hyperfine coupling constants and absolute energies of the $8p\ ^2P_{1/2}$ and $8p\ ^2P_{3/2}$ levels in atomic cesium," *Phys. Rev. A*, vol. 107, p. 012 807, 1 Jan. 2023. DOI: 10.1103/PhysRevA.107.012807. [Online]. Available: https://link.aps.org/doi/10.1103/PhysRevA.107.012807.

[60] H. Bucka and G. von Oppen, "Hyperfeinstruktur und lebensdauer des $8P_{3/2}$-terms im CsI-spektrum," *Annalen der Physik*, vol. 465, no. 1, pp. 119–120, 1962.

[61] A. Faist, E. Geneux, and S. Koide, "Frequency shift in magnetic transitions between hyperfine levels of $^2P_{3/2}$ states of Cs 133," *Journal of the Physical Society of Japan*, vol. 19, no. 12, pp. 2299–2305, 1964. DOI: 10.1143/JPSJ.19.2299. eprint: https://doi.org/10.1143/JPSJ.19.2299. [Online]. Available: https://doi.org/10.1143/JPSJ.19.2299.

[62] S. Rydberg and S. Svanberg, "Investigation of the $np\ ^2P_{3/2}$ level sequence in the Cs I spectrum by level crossing spectroscopy," *Physica Scripta*, vol. 5, no. 45, p. 209, 1972.

[63] J. Abele, M. Baumann, and W. Hartmann, "Gj-factors and magnetic hfs interaction constants in the 6 $^2P_{3/2}$-and 8 $^2P_{3/2}$-states of ^{133}Cs," *Physics Letters A*, vol. 51, no. 3, pp. 169–170, 1975.

[64] S. B. Bayram *et al.*, "Quantum beat spectroscopy: Stimulated emission probe of hyperfine quantum beats in the atomic Cs $8p\,^2P_{3/2}$ level," *Phys. Rev. A*, vol. 90, p. 062 510, 6 Dec. 2014. DOI: 10.1103/PhysRevA.90.062510. [Online]. Available: https://link.aps.org/doi/10.1103/PhysRevA.90.062510.

[65] P. Barbey and E. Geneux, "Hyperfine structure of the 8 $^2P_{3/2}$ state of cesium-133," *Helvetica Physica Acta (Switzerland)*, vol. 35, Jan. 1962. [Online]. Available: https://www.osti.gov/biblio/4737265.

[66] P. Tsekeris and R. Gupta, "Measurement of hyperfine structure of the $8^2S_{\frac{1}{2}}$ and $9^2S_{\frac{1}{2}}$ states of rubidium, and $12^2S_{\frac{1}{2}}$ state of cesium by stepwise dye-laser spectroscopy," *Phys. Rev. A*, vol. 11, pp. 455–459, 2 Feb. 1975. DOI: 10.1103/PhysRevA.11.455. [Online]. Available: https://link.aps.org/doi/10.1103/PhysRevA.11.455.

[67] P. Tsekeris, "Hyperfine-structure measurements in excited states of alkali atoms by cw laser spectroscopy," Ph.D. dissertation, Columbia University, 1976.

[68] S. Svanberg and G. Belin, "Determination of hyperfine structure and g_j factors in the sequences of 2d states in alkali atoms using a tunable dye laser," *Journal of Physics B: Atomic and Molecular Physics*, vol. 7, no. 3, p. L82, 1974. DOI: 10.1088/0022-3700/7/3/024. [Online]. Available: https://doi.org/10.1088/0022-3700/7/3/024.

[69] J. Deech, R. Luypaert, L. Pendrill, and G. Series, "Lifetimes, depopulation cross sections and hyperfine structures of some rydberg s and d states of ^{133}Cs," *Journal of Physics B: Atomic and Molecular Physics*, vol. 10, no. 5, p. L137, 1977. DOI: 10.1088/0022-3700/10/5/004. [Online]. Available: https://doi.org/10.1088/0022-3700/10/5/004.

[70] J. A. Quirk, A. Damitz, C. E. Tanner, and D. Elliott, "Measurement of the hyperfine coupling constants and absolute energies of the $12s^2S_{1/2}$, $13s^2S_{1/2}$, and $11d^2D_J$ levels in atomic cesium," *Physical Review A*, vol. 105, no. 2, p. 022 819, 2022.

[71] G. Toh, A. Damitz, C. E. Tanner, W. Johnson, and D. Elliott, "Determination of the scalar and vector polarizabilities of the cesium $6s\,^2S_{1/2} \rightarrow 7s\,^2S_{1/2}$ transition and implications for atomic parity nonconservation," *Physical Review Letters*, vol. 123, no. 7, p. 073 002, 2019.

[72] V. A. Dzuba and V. V. Flambaum, "Off-diagonal hyperfine interaction and parity nonconservation in cesium," *Phys. Rev. A*, vol. 62, p. 052 101, 5 Oct. 2000. DOI: 10.1103/PhysRevA.62.052101. [Online]. Available: https://link.aps.org/doi/10.1103/PhysRevA.62.052101.

[73] B. M. Roberts, C. J. Fairhall, and J. S. M. Ginges, "Electric-dipole transition amplitudes for atoms and ions with one valence electron," *Phys. Rev. A*, vol. 107, p. 052 812, 5 May 2023. DOI: 10.1103/PhysRevA.107.052812. [Online]. Available: https://link.aps.org/doi/10.1103/PhysRevA.107.052812.

[74] C. J. Fairhall, B. M. Roberts, and J. S. M. Ginges, "QED radiative corrections to electric dipole amplitudes in heavy atoms," *Phys. Rev. A*, vol. 107, p. 022 813, 2 Feb. 2023. DOI: 10.1103/PhysRevA.107.022813. [Online]. Available: https://link.aps.org/doi/10.1103/PhysRevA.107.022813.

[75] H. B. Tran Tan and A. Derevianko, "Precision theoretical determination of electric-dipole matrix elements in atomic cesium," *Phys. Rev. A*, vol. 107, p. 042 809, 4 Apr. 2023. DOI: 10.1103/PhysRevA.107.042809. [Online]. Available: https://link.aps.org/doi/10.1103/PhysRevA.107.042809.

[76] S. C. Bennett, J. L. Roberts, and C. E. Wieman, "Measurement of the dc Stark shift of the $6s \rightarrow 7s$ transition in atomic cesium," *Phys. Rev. A*, vol. 59, R16–R18, 1 Jan. 1999. DOI: 10.1103/PhysRevA.59.R16. [Online]. Available: %5C%5C%20https://link.aps.org/doi/10.1103/PhysRevA.59.R16.

[77] J. M. Amini and H. Gould, "High precision measurement of the static dipole polarizability of cesium," *Phys. Rev. Lett.*, vol. 91, p. 153 001, 15 Oct. 2003. DOI: 10.1103/PhysRevLett.91.153001. [Online]. Available: %5C%5C%20https://link.aps.org/doi/10.1103/PhysRevLett.91.153001.

[78] M. D. Gregoire, I. Hromada, W. F. Holmgren, R. Trubko, and A. D. Cronin, "Measurements of the ground-state polarizabilities of Cs, Rb, and K using atom interferometry," *Phys. Rev. A*, vol. 92, p. 052 513, 5 Nov. 2015. DOI: 10.1103/PhysRevA.92.052513. [Online]. Available: https://link.aps.org/doi/10.1103/PhysRevA.92.052513.

[79] J. R. P. Angel and P. Sandars, "The hyperfine structure Stark effect i. theory," *Proceedings of the Royal Society of London. Series A. Mathematical and Physical Sciences*, vol. 305, no. 1480, pp. 125–138, 1968.

[80] M. S. Safronova, U. I. Safronova, and C. W. Clark, "Magic wavelengths, matrix elements, polarizabilities, and lifetimes of cs," *Phys. Rev. A*, vol. 94, p. 012 505, 1 Jul. 2016. DOI: 10.1103/PhysRevA.94.012505. [Online]. Available: %5C%5C%20https://link.aps.org/doi/10.1103/PhysRevA.94.012505.

[81] J. Mitroy, M. S. Safronova, and C. W. Clark, "Theory and applications of atomic and ionic polarizabilities," *Journal of Physics B: Atomic, Molecular and Optical Physics*, vol. 43, no. 20, p. 202 001, Oct. 2010. DOI: 10.1088/0953-4075/43/20/202001. [Online]. Available: https://dx.doi.org/10.1088/0953-4075/43/20/202001.

[82] R. N. Watts, S. L. Gilbert, and C. E. Wieman, "Precision measurement of the Stark shift of the $6S-7S$ transition in atomic cesium," *Phys. Rev. A*, vol. 27, pp. 2769–2772, 5 May 1983. DOI: 10.1103/PhysRevA.27.2769. [Online]. Available: https://link.aps.org/doi/10.1103/PhysRevA.27.2769.

[83] J. Hoffnagle, V. Telegdi, and A. Weis, "Empirical determination of the scalar polarizability α in the $6S \rightarrow 7S$ transition in cesium," *Physics Letters A*, vol. 86, no. 9, pp. 457–460, 1981, ISSN: 0375-9601. DOI: https://doi.org/10.1016/0375-9601(81)90656-3. [Online]. Available: http://www.sciencedirect.com/science/article/pii/0375960181906563.

[84] W. van Wijngaarden and J. Li, "Polarizabilities of cesium s, p, d, and f states," *Journal of Quantitative Spectroscopy and Radiative Transfer*, vol. 52, no. 5, pp. 555–562, 1994, ISSN: 0022-4073. DOI: https://doi.org/10.1016/0022-4073(94)90024-8. [Online]. Available: https://www.sciencedirect.com/science/article/pii/0022407394900248.

[85] H. L. Zhou and D. W. Norcross, "Improved calculation of the quadratic Stark effect in the $6P_{3/2}$ state of Cs," *Phys. Rev. A*, vol. 40, pp. 5048–5051, 9 Nov. 1989. DOI: 10.1103/PhysRevA.40.5048. [Online]. Available: https://link.aps.org/doi/10.1103/PhysRevA.40.5048.

[86] C. Bouchiat, C. Piketty, and D. Pignon, "A theoretical analysis of parity violation induced by neutral currents in atomic cesium," *Nuclear Physics B*, vol. 221, no. 1, pp. 68–108, 1983, ISSN: 0550-3213. DOI: https://doi.org/10.1016/0550-3213(83)90619-3. [Online]. Available: http://www.sciencedirect.com/science/article/pii/0550321383906193.

[87] G. Toh *et al.*, "Measurement of the lifetime of the $7s^2S_{1/2}$ state in atomic cesium using asynchronous gated detection," *Phys. Rev. A*, vol. 97, p. 052 507, 5 May 2018. DOI: 10.1103/PhysRevA.97.052507. [Online]. Available: %5C%5C%20https://link.aps.org/doi/10.1103/PhysRevA.97.052507.

[88] G. Toh *et al.*, "Electric dipole matrix elements for the $6p\,^2P_J \rightarrow 7s\,^2S_{1/2}$ transition in atomic cesium," *Phys. Rev. A*, vol. 99, p. 032 504, 3 Mar. 2019. DOI: 10.1103/PhysRevA.99.032504. [Online]. Available: https://link.aps.org/doi/10.1103/PhysRevA.99.032504.

[89] L. Young *et al.*, "Precision lifetime measurements of cs 6p $^2P_{1/2}$ and 6p $^2P_{3/2}$ levels by single-photon counting," *Phys. Rev. A*, vol. 50, pp. 2174–2181, 3 Sep. 1994. DOI: 10.1103/PhysRevA.50.2174. [Online]. Available: https://link.aps.org/doi/10.1103/PhysRevA.50.2174.

[90] R. J. Rafac and C. E. Tanner, "Measurement of the ratio of the cesium D-line transition strengths," *Phys. Rev. A*, vol. 58, pp. 1087–1097, 2 Aug. 1998. DOI: 10.1103/PhysRevA.58.1087. [Online]. Available: https://link.aps.org/doi/10.1103/PhysRevA.58.1087.

[91] R. J. Rafac, C. E. Tanner, A. E. Livingston, and H. G. Berry, "Fast-beam laser lifetime measurements of the cesium $6p^2P_{1/2,3/2}$ states," *Phys. Rev. A*, vol. 60, pp. 3648–3662, 5 Nov. 1999. DOI: 10.1103/PhysRevA.60.3648. [Online]. Available: https://link.aps.org/doi/10.1103/PhysRevA.60.3648.

[92] A. Derevianko and S. G. Porsev, "Determination of lifetimes of $6P_J$ levels and ground-state polarizability of cs from the van der waals coefficient C_6," *Phys. Rev. A*, vol. 65, p. 053 403, 5 Apr. 2002. DOI: 10.1103/PhysRevA.65.053403. [Online]. Available: https://link.aps.org/doi/10.1103/PhysRevA.65.053403.

[93] N. Bouloufa, A. Crubellier, and O. Dulieu, "Reexamination of the 0_g^- pure long-range state of Cs_2: Prediction of missing levels in the photoassociation spectrum," *Phys. Rev. A*, vol. 75, p. 052 501, 5 May 2007. DOI: 10.1103/PhysRevA.75.052501. [Online]. Available: %5C%5C%20https://link.aps.org/doi/10.1103/PhysRevA.75.052501.

[94] Y. Zhang, J. Ma, J. Wu, L. Wang, L. Xiao, and S. Jia, "Experimental observation of the lowest levels in the photoassociation spectroscopy of the 0_g^- purely-long-range state of cs_2," *Phys. Rev. A*, vol. 87, p. 030 503, 3 Mar. 2013. DOI: 10.1103/PhysRevA.87.030503. [Online]. Available: https://link.aps.org/doi/10.1103/PhysRevA.87.030503.

[95] B. M. Patterson *et al.*, "Lifetime measurement of the cesium $6P_{3/2}$ level using ultrafast pump-probe laser pulses," *Phys. Rev. A*, vol. 91, p. 012 506, 1 Jan. 2015. DOI: 10.1103/PhysRevA.91.012506. [Online]. Available: https://link.aps.org/doi/10.1103/PhysRevA.91.012506.

[96] C. E. Tanner *et al.*, "Measurement of the $6p^2P_{3/2}$ state lifetime in atomic cesium," *Phys. Rev. Lett.*, vol. 69, pp. 2765–2767, 19 Nov. 1992. DOI: 10.1103/PhysRevLett.69.2765. [Online]. Available: https://link.aps.org/doi/10.1103/PhysRevLett.69.2765.

[97] J. F. Sell, B. M. Patterson, T. Ehrenreich, G. Brooke, J. Scoville, and R. J. Knize, "Lifetime measurement of the cesium $6P_{3/2}$ state using ultrafast laser-pulse excitation and ionization," *Phys. Rev. A*, vol. 84, 010501(R), 1 Jul. 2011. DOI: 10.1103/PhysRevA.84.010501. [Online]. Available: https://link.aps.org/doi/10.1103/PhysRevA.84.010501.

[98] A. Damitz, G. Toh, E. Putney, C. E. Tanner, and D. S. Elliott, "Measurement of the radial matrix elements for the $6s\,^2S_{1/2} \rightarrow 7p\,^2P_J$ transitions in cesium," *Phys. Rev. A*, vol. 99, p. 062 510, 6 Jun. 2019. DOI: 10.1103/PhysRevA.99.062510. [Online]. Available: https://link.aps.org/doi/10.1103/PhysRevA.99.062510.

[99] A. Kramida, Y. Ralchenko, J. Reader, and NIST ASD team, "NIST atomic spectra database (version 5.10); National Institute of Standards and Technology, Gaithersburg, MD, 2012," *web*, p. 2, 2022, https://physics.nist.gov/asd.

[100] G. Toh, A. Damitz, C. E. Tanner, W. R. Johnson, and D. S. Elliott, "Determination of the scalar and vector polarizabilities of the cesium $6s\ ^2S_{1/2} \rightarrow 7s\ ^2S_{1/2}$ transition and implications for atomic parity nonconservation," *Phys. Rev. Lett.*, vol. 123, no. 7, p. 073 002, 2019. DOI: 10.1103/PhysRevLett.123.073002. [Online]. Available: https://link.aps.org/doi/10.1103/PhysRevLett.123.073002.

[101] V. A. Dzuba, V. V. Flambaum, and O. P. Sushkov, "Polarizabilities and parity nonconservation in the Cs atom and limits on the deviation from the standard electroweak model," *Phys. Rev. A*, vol. 56, R4357–R4360, 6 Dec. 1997. DOI: 10.1103/PhysRevA.56.R4357. [Online]. Available: https://link.aps.org/doi/10.1103/PhysRevA.56.R4357.

[102] D. Xiao, H. B. Tran Tan, and A. Derevianko, "Nuclear-spin-dependent corrections to the transition polarizability in cesium," *Phys. Rev. A*, vol. 108, p. 032 805, 3 Sep. 2023. DOI: 10.1103/PhysRevA.108.032805. [Online]. Available: https://link.aps.org/doi/10.1103/PhysRevA.108.032805.

[103] A. A. Vasilyev, I. M. Savukov, M. S. Safronova, and H. G. Berry, "Measurement of the $6s - 7p$ transition probabilities in atomic cesium and a revised value for the weak charge Q_W," *Phys. Rev. A*, vol. 66, p. 020 101, 2 Aug. 2002. DOI: 10.1103/PhysRevA.66.020101. [Online]. Available: https://link.aps.org/doi/10.1103/PhysRevA.66.020101.

[104] V. A. Dzuba, V. V. Flambaum, and J. S. M. Ginges, "High-precision calculation of parity nonconservation in cesium and test of the standard model," *Phys. Rev. D*, vol. 66, p. 076 013, 7 Oct. 2002. DOI: 10.1103/PhysRevD.66.076013. [Online]. Available: https://link.aps.org/doi/10.1103/PhysRevD.66.076013.

[105] B. K. Sahoo and B. P. Das, "Constraints on new physics from an improved calculation of parity violation in ^{133}Cs," *arXiv 2008.08941*, 2020. [Online]. Available: https://arxiv.org/abs/2008.08941.

[106] J. A. Quirk, A. Jacobsen, A. Damitz, C. E. Tanner, and D. S. Elliott, "Measurement of the static Stark shift of the $7s\ ^2S_{1/2}$ level in atomic cesium," *Phys. Rev. Lett.*, vol. 132, p. 233 201, 23 Jun. 2024. DOI: 10.1103/PhysRevLett.132.233201. [Online]. Available: https://link.aps.org/doi/10.1103/PhysRevLett.132.233201.

[107] P. R. Bevington and D. K. Robinson, *Data Reduction and Error Analysis for the Physical Sciences*, 3rd. McGraw Hill, 2003, ISBN: 0-07-247227-8.

[108] D. Z. Anderson, J. C. Frisch, and C. S. Masser, "Mirror reflectometer based on optical cavity decay time," *Appl. Opt.*, vol. 23, no. 8, pp. 1238–1245, Apr. 1984. DOI: 10.1364/AO.23.001238. [Online]. Available: https://opg.optica.org/ao/abstract.cfm?URI=ao-23-8-1238.

[109] S. G. Porsev, K. Beloy, and A. Derevianko, "Precision determination of electroweak coupling from atomic parity violation and implications for particle physics," *Phys. Rev. Lett.*, vol. 102, p. 181 601, 18 May 2009. DOI: 10.1103/PhysRevLett.102.181601. [Online]. Available: https://link.aps.org/doi/10.1103/PhysRevLett.102.181601.

[110] S. G. Porsev, K. Beloy, and A. Derevianko, "Precision determination of weak charge of ^{133}Cs from atomic parity violation," *Phys. Rev. D*, vol. 82, p. 036 008, 3 Aug. 2010. DOI: 10.1103/PhysRevD.82.036008. [Online]. Available: https://link.aps.org/doi/10.1103/PhysRevD.82.036008.

[111] V. A. Dzuba, J. C. Berengut, V. V. Flambaum, and B. Roberts, "Revisiting parity nonconservation in cesium," *Phys. Rev. Lett.*, vol. 109, p. 203 003, 20 Nov. 2012. DOI: 10.1103/PhysRevLett.109.203003. [Online]. Available: https://link.aps.org/doi/10.1103/PhysRevLett.109.203003.

[112] B. M. Roberts, V. A. Dzuba, and V. V. Flambaum, "Quantum electrodynamics corrections to energies, transition amplitudes, and parity nonconservation in Rb, Cs, Ba^+, Tl, Fr, and Ra^+," *Phys. Rev. A*, vol. 87, p. 054 502, 5 May 2013. DOI: 10.1103/PhysRevA.87.054502. [Online]. Available: https://link.aps.org/doi/10.1103/PhysRevA.87.054502.

[113] V. V. Flambaum and J. S. M. Ginges, "Radiative potential and calculations of QED radiative corrections to energy levels and electromagnetic amplitudes in many-electron atoms," *Phys. Rev. A*, vol. 72, p. 052 115, 5 Nov. 2005. DOI: 10.1103/PhysRevA.72.052115. [Online]. Available: https://link.aps.org/doi/10.1103/PhysRevA.72.052115.

[114] R. N. Zare, *Angular momentum: Understanding spatial aspects in chemistry and physics*. New York, 1988.

A. ELECTRIC QUADRUPOLE

We mentioned previously that the electric quadrupole transition will not affect the PNC measurement. Here we will discuss this in further detail. We will start with the general phenomenological transition operator that Bouchiat and Piketty introduced [32]. This operator is as follows,

$$\begin{aligned} T(n,n') = -2M_1 \boldsymbol{S}\cdot(\boldsymbol{\mathcal{E}}\times k) - \mathrm{i}(M_1^{hf}/2)\,(\boldsymbol{S}\times\boldsymbol{I})\cdot(\boldsymbol{\mathcal{E}}\times\boldsymbol{k}) \\ -\mathrm{i}(E_2/2)\left[(\boldsymbol{S}\cdot\boldsymbol{\mathcal{E}})\,(\boldsymbol{I}\cdot\boldsymbol{k}) + (\boldsymbol{S}\cdot\boldsymbol{k})\,(\boldsymbol{I}\cdot\boldsymbol{\mathcal{E}})\right]. \end{aligned} \tag{A.1}$$

The first and second terms represent the hyperfine invariant magnetic dipole moment and the hyperfine changing component of the magnetic dipole moment. The last term is the electric quadrupole moment caused by off-diagonal hyperfine mixing of $|nD\rangle$ and $|nP\rangle$ states [32]. Figure A.1 shows the field geometry for the PNC measurement. When only considering the E_2 amplitude with the PNC applied field geometry, equation A.1 simplifies to

$$T(n,n') = -\mathrm{i}(E_2/2)\left[S_x I_y + S_y I_x\right]\mathcal{E}_x k_y. \tag{A.2}$$

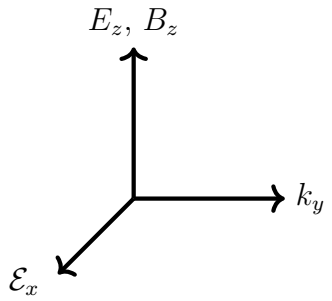

Figure A.1. Geometry for analyzing the electric quadrupole transition.

We can rewrite these products of spherical tensor operators as another tensor operator using the technique described in Zare (5.44)[114],

$$X(2,\pm 2) = \left[A^{(1)} \otimes B^{(1)}\right]^{(2)}_{\pm 2} = \frac{1}{2}\left[(A_x B_x - A_y B_y) \pm \mathrm{i}\,(A_x B_y + A_y B_x)\right]. \tag{A.3}$$

Then the difference of $X(2,2) - X(2,-2)$ is,

$$X(2,2) - X(2,-2) = 2\mathrm{i}(S_x I_y + S_y I_x). \tag{A.4}$$

We can substitute this into equation A.2 to find,

$$T = \frac{-E_2}{4}\left[X(2,2) - X(2,-2)\right]\mathcal{E}_x k_y. \tag{A.5}$$

We can use Zare (5.64) to evaluate the reduced matrix element,

$$\begin{aligned}\langle 7sS'I'F'm'||T||6sSIFm\rangle = -\frac{E_2}{4}(-1)^{F-m}&\left[\begin{pmatrix} F & 2 & F' \\ -m & 2 & m' \end{pmatrix} - \begin{pmatrix} F & 2 & F' \\ -m & -2 & m' \end{pmatrix}\right] \\ &\times\langle 7sS'I'F'||X^{(2)}||6sSIF\rangle\mathcal{E}_x \boldsymbol{k}_y\end{aligned} \tag{A.6}$$

For the Wigner- 3-j symbol to be nonzero, the bottom row must sum to zero. This implies that we will only see a contribution from $\Delta m = \pm 2$ transitions. Since we will be interfering a $\Delta m = \pm 1$ transition when measuring E_{PNC}/β, the E_2 moment will not affect this measurement.

B. PHASE MATCHING CONDITION FOR CROSSED BEAMS

Careful alignment of the three Fabry-Perot cavities driving the PNC interaction is critical for preserving phase matching. If the crossing angle is too sharp or if there is no overlap, the interference signal will be reduced. Here we will discuss the angular alignment necessary for the PNC experiment. We must ensure that the wave vectors of each beam do not "slip" a cycle over the interaction region. If they do, a portion will be in phase and another out of phase. This reduces or can even fully average away the interference amplitude. The requirement is then,

$$\Delta\vec{k} \cdot \vec{r} < \pi \tag{B.1}$$

where $\Delta\vec{k}$ is the wave vector mismatch and $\vec{r}$ is any vector within the interaction region.

B.1 Experiment geometry

Figure B.1 shows the alignment of the triple cavity setup. With the angles labeled here, we will evaluate equation B.1. Here we have,

$$\left|\left[\vec{k}_{1470} + \vec{k}_{852} - \vec{k}_{540}\right] \cdot \vec{r}\right| < \pi, \tag{B.2}$$

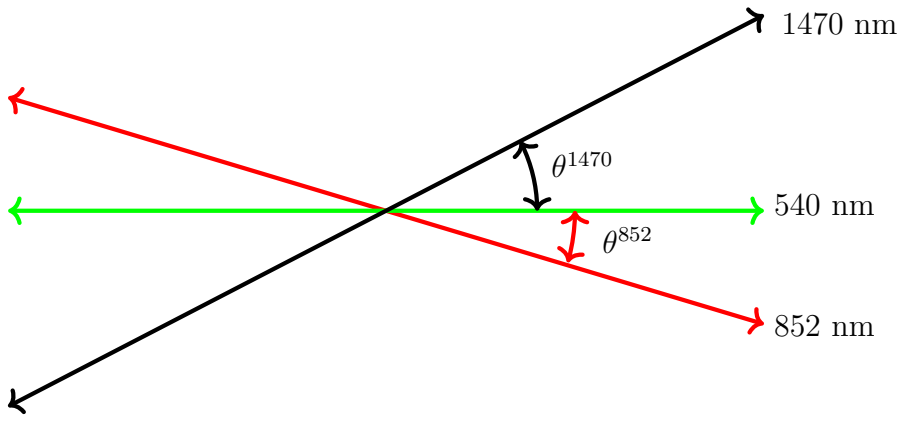

Figure B.1. Geometry for analyzing the crossing angle of the three Fabry-Perot cavities.

where $\vec{k}_n$ is the nth laser's wave vector. We can now split this equation into an x and y component. The x component is along the laser beam, so its interaction length is around 1 mm. The y component is along the atomic beam and is characterized by the diameter of the laser beams, 2ω =1 mm. Here ω is the waist radius. The x and y components are as follows,

$$\left|\left[k_{1470}\cos(\theta^{1470}) + k_{852}\cos(\theta^{852}) - k_{540}\right]\cdot\vec{r}\right| < \pi, \tag{B.3}$$

$$\left|\left[k_{1470}\sin(\theta^{1470}) - k_{852}\sin(\theta^{852})\right]\cdot\vec{r}\right| < \pi. \tag{B.4}$$

This second equation is linear in angle for small angles, so we would like to suppress this term by appropriately choosing θ^{1470} and θ^{852}. This is accomplished by setting the angles to,

$$\frac{\theta^{1470}}{\theta^{852}} = \frac{\lambda_{1470}}{\lambda_{852}}. \tag{B.5}$$

We ensure $k_{1470} + k_{852} - k_{540} = 0$ with our locking scheme. Then the upper equation simplifies to,

$$\left[\frac{(\theta^{1470})^2}{\lambda_{1470}} + \frac{(\theta^{852})^2}{\lambda_{852}}\right] d_x < \frac{1}{2}, \tag{B.6}$$

where d_x is the length of the interaction region along the laser beam, 1 mm. When we use the angle ratio from equation B.5, we can further simplify and solve for one of the angles. We solve for the angle between the 852 nm beam and the 540 nm beam and get,

$$(\theta^{852})^2 < \frac{\lambda_{852}}{2d_x\,(1+\lambda_{1470}/\lambda_{852})}. \tag{B.7}$$

With d_x =1 mm, we get θ^{852}<12.5 mrad. If we suppose that there is an error in set angle such that equation B.4 does not perfectly cancel, then we can manually add in an error (δ) to θ^{852}.

This modifies equation B.4 to,

$$\left|\left[\frac{2\pi}{\lambda_{1470}}\theta^{1470} - \frac{2\pi}{\lambda_{852}}\left(\theta^{852}+\delta\right)\right] d_y\right| < \pi. \tag{B.8}$$

Here, d_y spans the interaction region along the cesium beam (laser beam diameter). This length is 1 mm. Equation B.4 then places the constraint in the precision we must set for the angle.

$$\delta < \frac{\pi\lambda_{852}}{2d_y} \tag{B.9}$$

With d_y =1 mm, the error in the angle must be less than 1.3 mrad. This should not be so critical since a pair of machined pin holes could be used to fixed this distance, 0.2 mm for a 35 cm cavity.

B.2 Conclusion

Proper phase matching in the interaction region will not be easily attained and will require careful design and planning. The crossing angle becomes less restrictive as the atomic beam is apertured down, but this method reduces the overall signal strength. Unfortunately, the maximum angle increases as $1/\sqrt{d_x}$, so halving the interaction size only increases the tolerable angle by 41%. A 12.5 mrad crossing angle between the 540 nm and 852 nm beams for a 35 cm length cavity only gives a beam distance of 2.2 mm. Some creative construction inside the vacuum chamber may allow longer beam paths.

PUBLICATIONS

Jonah Quirk, Aidan Jacobsen, Amy Damitz, C. E. Tanner, and D. S. Elliott, Measurement of the static Stark shift of the $7s\ ^2S_{1/2}$ level in atomic cesium, Phys. Rev. Lett., vol. 132, p. 233 201, 23 Jun. 2024.

Jonah Quirk, Amy Damitz, C. E. Tanner, and D. Elliott, Measurement of the hyperfine coupling constants and absolute energies of the $12s\ ^2S_{1/2}$, $13s\ ^2S_{1/2}$, and $11d\ ^2D_J$ levels in atomic cesium, Physical Review A, vol. 105, no. 2, p. 022 819, 2022.

Jonah Quirk, Liam Sherman, Amy Damitz, C. E. Tanner, and D. S. Elliott, Measurement of the hyperfine coupling constants and absolute energies of the $8p\ ^2P_{1/2}$ and $8p\ ^2P_{3/2}$ levels in atomic cesium, Phys. Rev. A, vol. 107, p. 012 807, 1 Jan. 2023.

Jonah Quirk, C. E. Tanner, and D. S. Elliott, Measurement of the ratio of the scalar polarizability to the vector polarizability for the $6s\ ^2S_{1/2} \rightarrow 7s\ ^2S_{1/2}$ transition in cesium, Phys. Rev. A, vol. 109, p. 062 809, 6 Jun. 2024.

George Toh, Jose A. Jaramillo-Villegas, Nathan Glotzbach, Jonah Quirk, Ian C. Stevenson, J. Choi, Andrew M. Weiner, and D. S. Elliott, Measurement of the lifetime of the $7s\ ^2S_{1/2}$ state in atomic cesium using asynchronous gated detection, Phys. Rev. A, vol. 97, p. 052 507, 5 May 2018.

George Toh, Amy Damitz, Nathan Glotzbach, Jonah Quirk, I. C. Stevenson, J. Choi, M.S. Safronova, and D.S. Elliott, "Electric dipole matrix elements for the $6p\ ^2P_J \rightarrow 7s\ ^2S_{1/2}$ transition in atomic cesium," Phys. Rev. A 99, 032904 (2019).

Amy Damitz, Jonah Quirk, Carol Tanner, and D.S. Elliott, "Technique for a direct measurement of the cesium anapole moment using coherent rf and Raman interactions," Phys. Rev. A 109 (3), 032810 (2024).